A Thesis submitted for the degree of

PHILOSOPHIAE DOCTOR

Innovative perspectives for seismic isolation of gravitational-wave detectors

Chiara Di Fronzo

Institute of Gravitational Wave Astronomy

School of Physics and Astronomy

University of Birmingham

December 2021

UNIVERSITY^{OF}BIRMINGHAM

University of Birmingham Research Archive

e-theses repository

Statement of originality

I confirm that the work presented in this thesis is original and has been entirely carried out by the author, started and completed at the University of Birmingham. The work done in collaboration with other scientific groups and/or abroad has been suitably highlighted throughout the thesis.

During my second year I collaborated with the Albert Einstein Institute (Hannover) to test a device I designed and built in Birmingham. In the same year, I spent 5 months, between June and November 2019, at LIGO Harford site, working on ideas for improving the stability of the interferometer. This work has been carried on in collaboration with the SEI (SEIsmic) group of Stanford, MIT, Caltech, UoB and LIGO Livingston.

Chiara Di Fronzo

Abstract

The discovery of gravitational waves opened a new way to look at the Universe and offered new opportunities to shed light on the still unknown aspects of physical sciences. The work presented in this thesis wants to give a contribution to the development of this new type of research: the author chose to focus on the improvement of the instruments able to detect the gravitational waves. This field is important to make the detectors more sensitive, in order to see more gravitational-wave sources and help to complete the mosaic of the astrophysical science. In particular, the detectors currently in use are interferometers, which are especially blind in a range of frequency below 30 Hz: this affects the chance to detect sources emitting in this frequency band.

This lack of sensitivity is mainly due to seismic motion, and the work presented in this thesis focussed on new techniques to lower the noise sources and allow the instruments to be sensitive below 30 Hz.

During the studies, the development and test of devices capable of potentially reducing the seismic motion have been performed, such as optical levers for tilt motion reduction and laser stabilization for low frequency readout; a new concept of the seismic system on one of the interferometers (LIGO) has also been proposed.

The optical levers can in principle reduce tilt motion below 1 Hz; the use of capacitive position sensors in a new software configuration for LIGO can help to suppress ground motion by a factor of 3 in order of magnitude below 0.1 Hz. A competitive frequency stabilization to 3.6 $\times$ 10^3 Hz/$\sqrt{Hz}$ at 1 Hz for readout at low frequency is possible with a

Abstract

compact and easy to handle setup. These results are promising to provide suppression of the seismic motion in the bandwidth of interest and show that it is possible for a ground-based instrument to be seismically more stable and capable of detecting gravitational waves where it is now forbidden.

Ai miei genitori e a mia sorella.

Acknowledgements

Contents

Contents

List of Figures

List of Tables

Notations

Speed of light:

$c = 3 \times 10^8$ **m/s**

Gravitational constant:

$G = 6,67^{-11}$ **Nm^2/Kg^2**

Gravitational wave amplitude:

$h \sim 10^{-21}$ $1/\sqrt{Hz}$

Solar mass:

$M_\odot = 10^{33}$ **g**

Chirp Mass

$M_c = \dfrac{(m_1 \cdot m_2)^{3/5}}{(m_1 + m_2)^{1/5}}$

Wave number

$k = 2\pi/\lambda$

Gravitational acceleration

$g = 9.8 m/s^2$

Boltzmann constant

$k_B = 1.38 \times 10^{-23}$ **J/K**

Acronyms

AA = Anti-Aliasing

ADC = Analogue-to-Digital Converter

AEI = Albert Einstein Institute

aLIGO = Advanced Laser Interferometric Gravitational-wave Observatory

AI = Anti-Imaging

ASD = Amplitude Spectral Density

BRS = Beam Rotation Sensors

BS = Beam Splitter

BSC = Basic Symmetric Chamber

BH = Black Hole

CARM = Common Arm length

CDS = Control and Data System

CP = Compensation Plate

CPS = Capacitive Position Sensors

CS = Corner Station

DAC = Digital-to-Analogue Converter

DARM = Differential Arm Length

DCC = Document Control Center

DIFF2SE = Differential to Single-Ended

ETM = End Test Mass

ET = Einstein Telescope

FC = Filter Cavity

FI = Faraday Isolator

List of Tables

FIR = Finite Impulse Response

HAM = Horizontal Access Module

HEPI = Hydraulic External Pre-Isolator

HoQI = Homodyne Quadrature Interferometer

HP = High Pass filter

HSTS = HAM Small Triple Suspension

IMBH = Intermediate Mass Black Hole

IMC = Input Mode Cleaner

IMCL = Input Mode Cleaner Length

ISI = Internal Seismic Isolation

ITM = Input Test Mass

LHO = LIGO Hanford Observaotry

LLO = LIGO Livingston Observatory

LP = Low Pass filter

LSC = Length Sensing and Control

LVDT = Linear Variable Displacement Transformer

LVK = Ligo-Virgo-Kagra meeting

MCA = Mid-Course Assessment

MICH = Michelson length

MIT = Massachusetts Institute of Technology

ND = Neutral-Density (filter)

NPBS = Non-Polarizing Beam Splitter

NS = Neutron Star

OPL = Opltical Path Length

PBS = Polarizing Beam Splitter

PD = PhotoDiode

PR = Power Recycling

PRCL = Power Recycling Cavity Length

PSD = Power Spectral Density

QPD = Quadrant Position Device

RIN = Relative Intensity Noise

SC = Sensor Correction

SR = Signal Recycling

SRCL = Signal Recycling Cavity Length

STS = Streckheisen Tri-axial Seismometer

TEC = Thermo-Electric Controller

UoB = University of Birmingham

Part I.

Gravitational-wave frontiers

1. Introduction

In this chapter I will briefly introduce the key concepts that establish the goals of the work presented in this thesis and moved all its steps. My research has been devoted to the enhancement of the instruments currently used to detect gravitational waves, which is one of the most advanced fields of astrophysics research of our time.

A detailed structure of the thesis then follows.

1.1. Gravitational waves and their detection

Gravitational waves are an astrophysical event that takes place when massive objects move with a quadrupolar momentum and deform the fabric of spacetime [1]. They have been theorized by Albert Einstein in 1915 and discovered a hundred years later by a joint collaboration of two detectors [3] [4], which was worthy of the Nobel Prize for Physics in 2017 [2].

The effect of the gravitational-wave radiation is to produce a strain h that induces a deformation of the physical lengths. This strain is typically very small ($h \sim 10^{-21}$), because the strain amplidute scales as $\sim GQ/c^4$, where $G = 6,67^{-11}$ Nm^2/Kg^2, Q is the quadrupole mass moment of the wave and c is the speed of light [2]. The quadrupole mass moment

---

[1]An in-depth source about how gravitational waves have been computed and their features is [2].

[2]See Appendix C for some information about the first detection of gravitational waves.

is directly proportional to the mass of the object involved: masses able to deform the fabric of spacetime and generate gravitational-wave amplitudes detectable on the Earth are of the order of more than the solar mass $M_\odot$, so such massive objects need to be looked for in the Universe.

1.1.1. A challenging detection

Detecting gravitational waves is particularly challenging, because the effect is very small, and the sensitivity required for an instrument to see it must be suitably high.

The challenging goal of detecting gravitational waves opened a research field dedicated to the development of new technologies, that could help to obtain the sensitivity necessary for the detection to happen.

This research is important, because detecting gravitational waves provides information on the sources which produced them. There is still a gap in the knowledge of many astrophysical objects, such as Black Holes (BH), Neutron Stars (NS) and Supernova events: this new-born branch of astrophysics will help to fill the gap and increase our knowledge of the Universe.

The detectors currently in use are sensitive to events from sources emitting at frequencies above ~ 30 Hz, but there is still a broad range of frequencies to which the detectors are blind. Looking at different frequencies of emission means looking at different objects emitting gravitational waves. This would broaden the catalogue of observed objects and the chances to better understand their nature.

The work carried on during my PhD studies and presented in this thesis has been dedicated to the improvement of the sensitivity of the detectors at frequencies below 10 Hz, by the development of new ideas and tech-

nologies to reduce noise sources affecting the low-frequency bandwidth, in particular the seismic motion.

1.2. Structure of this thesis

This thesis presents a study for the enhancement of the detectors for gravitational waves. It is divided into two parts: Part 1 introduces the context of the work done and frames the study into the specific field of the low frequency window and illustrates some features of the detectors useful to fully understand the work done in the laboratories. Part 2 is entirely focussed on the work done during the years between 2017 and 2021, covering the experience at LIGO Hanford and at the Albert Einstein Institute. This part includes the details of the experiments performed and their results.

Chapter 2. In this chapter we will see that there are some gravitational-wave sources emitting at lower frequency to which the current detectors are blind: it is in this frame that the experiments proposed in this thesis have been done. The final and ambitious goal is to improve the sensitivity of the detectors at lower frequencies.

Chapter 3. This chapter describes briefly how an interferometric detector for gravitational waves works. In particular, the detector LIGO, with which I collaborated, is illustrated. Specific details of the instruments to which I contributed are explained and referred to throughout the experimental work in the following chapters.

Chapter 4. This chapter contains the first experimental work performed in the first year of my PhD study: an optical lever for the reduction of tilt motion has been designed and built at UoB, and then tested at the AEI. The details of the experiment and the results are explained in detail.

Chapter 5. This chapter is focused entirely on the work done during my collaboration at LIGO Hanford in 2019. During the O3a and O3b runs I had the chance to contribute to the improvement of the detectors by studying a new configuration of the seismic system in order to make the instrument more stable and allow a longer observing time. The details of this study include original computations and tests at the LIGO sites.

Chapter 6. During the last year of my PhD studies, I contributed to the development of a new device for seismic control; in particular, I focused on the stabilization in frequency of the laser source of the device, making use of new technology and advanced techniques. The experiment has been fully carried out at UoB between September 2020 and September 2021 and it is described in detail.

2. The low frequency window

The scientific research presented in this thesis focuses on the improvement of ground-based gravitational-wave detectors at low frequency. This chapter intends to frame the work done in this context and highlight why the lower frequency window is so important. The discussion around this topic is relatively recent and it has been widely debated during dedicated workshops which the author of this thesis attended since 2018.

2.1. Sources of gravitational waves

Fig. 2.1 summarizes the possible objects that can be gravitational-waves sources, their frequency of emission and what kind of instrument can detect them. The terrestrial interferometric detectors are the most involved at present, but the efforts of the scientific community are directed towards the development of new detectors, both ground- and space-based, in order to widen the frequency window of observation.

The best modelled sources are binary systems, orbiting around a common central point. The Fig. 2.2 shows the main phases of the evolution of these kind of systems and the emission of gravitational waves at different frequencies, depending on the phase.

Gravitational waves from binary systems can provide information about the equation of state of Neutron stars, masses and spin of Black Holes and allow for test of General Relativity [1] [2]. The interest of the scientific community for these events and their detectors is therefore linked

2. The low frequency window
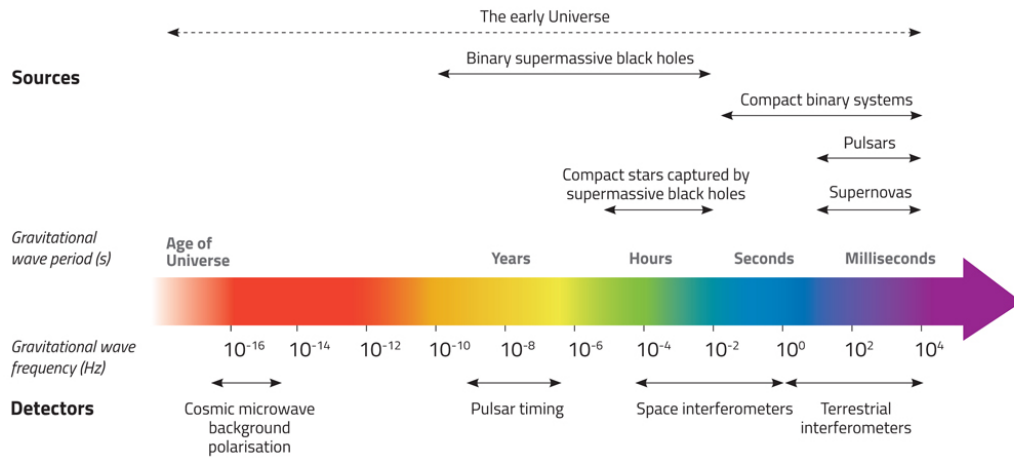
Figure 2.1.: Spectrum of emission of sources of gravitational waves (adapted from https://lisa.nasa.gov).

to the possibility of new astrophysical discoveries.

Currently, the ground-based observatories are tuned to detect emission mostly from binary systems: the interferometers are the only instruments that have been able to detect gravitational waves from these kind of sources.

The first detection of gravitational waves happened on the 14th September 2015 and confirmed the Theory of General Relativity, opening a new window on the Universe: the signal from a merger of two black holes have been observed thanks to the emission of gravitational waves, confirming the existence of these objects, still mostly unknown [4].

The detector responsible of the new discovery is based in the USA and it is one of the terrestrial interferometers currently in use for gravitational-wave detection [1].

---

[1]The working principles of the interferometers and details about the US instrument are explained in Chapter 3

Figure 2.2.: The three phases of a Black Hole (BH-BH) binary system emitting gravitational waves (amplitude vs time) [4]. **Inspiral phase**: the orbits shrink, velocity increases and frequency of the waves emitted increases as $f_{gw} = 2f_{orbital}$. **Merging phase**: the objects merge and the signal is at maximum. **Ring-down phase**: a new BH is formed and the signal emitted decreases in frequency as a damped sinusoid.

2.2. Opening the low frequency window

As we will see in the next chapter, the ground-based detectors involved in the search of gravitational waves cover a wide range of frequencies, but they are affected by some noises which make them unable to detect waves from sources emitting below 30 Hz. We will later see the nature of these noises. The reason why it is important to open the lower frequency window is that it can give access to the detection of gravitational waves emitted by sources whose physical structure and astrophysical features are still unknown and also to explore the features of a wave in the earlier phases of the inspiral.

This is the end towards which a significant part of the scientific collaboration is directed.

2.2.1. Frequencies of emission

The emitted frequency from a source of gravitational waves depends on the masses and the orbital frequency involved[2] and for mergers of binary systems, the frequency of a gravitational wave is twice the orbital frequency of its source [2]. Therefore, it can be used to determine the relation between the masses and the time to coalescence, i.e. the time when the two objects merge [3]. For masses in circular orbits, this is given by:

$$\tau \simeq 2.18s \left(\frac{1.21 M_\odot}{M_c}\right)^{5/3} \left(\frac{100 Hz}{f_{gw}}\right)^{8/3}, \qquad (2.1)$$

where M_c is the combination of the two involved masses m_1 and m_2, defined as *chirp mass* $M_c = (m_1 \cdot m_2)^{3/5}/(m_1 + m_2)^{1/5}$.

This equation is particularly useful if we want to know information about the radiation emitted by a certain mass, at a certain frequency, at a certain time before the merger. Predictions about this time and the frequency where it is possible to detect the radiation are essential for several reasons, going from efficiency of the detector in detecting different sources to Multimessenger astronomy, in which timing is important to assure a correct localization of the source [7].

In our case of interest, if we apply the lowest range of frequency available by ground-based detectors ($\sim$ 10 Hz in order of magnitude) and consider M_c = 1.21 $M_\odot$, it is possible to observe the radiation emitted at τ = 17 minutes to coalescence. Hence the equation says that the larger the time to coalescence is, the smaller the masses involved are [4].

Recalling Fig. 2.1, the range of the frequencies of emission below 10 Hz

---

[2]A detailed derivation of the gravitational-wave equation and how the frequencies of emission depend on the features of the sources can be found in [2].

[3]A simple example based on point-like masses in circular orbits is explained in details in [2].

[4]A useful exercise to prove this is by applying the Kepler's law for different emitting frequencies and masses. Some interesting examples are given in [2].

lies almost entirely in the domain of the space-based detectors. Opening this frequency window would allow the ground-based detectors to access to a frequency bandwidth which has still not been investigated and would allow the detection from sources whose physics is still unknown.

2.2.2. Redshifted frequencies

When dealing with cosmological objects, we need to take into account the contribution of the redshift z: in the case of gravitational waves, the redshift acts on the observed frequency. In a cosmological context, the time-scale is redshifted, and so is the frequency observed f_{obs} with respect to the emitted one f_{gw} by [2] [3]:

$$f_{obs} = f_{gw}/(1 + z).$$

(2.2)

The implication of this effect lies in a factor (1+z) multiplied to the masses involved [2].

An important consequence is that if the instrument could detect in a broader range of lower frequencies, it is possible to identify objects located at higher redshifts, i.e. more ancient, or apparent high masses increased by the cosmological distance [5]. Examples of these objects are Intermediate Mass Black Holes (IMBH) or stellar-mass BHs, whose nature and physics are still unknown.

2.2.3. Multi-messenger astronomy and low frequencies

Multi-messenger astronomy is a branch of astronomy born with the first gravitational wave detections. It has been seen that the signal of a gravitational wave can be followed up by observatories operating in other frequency bands (say, the electromagnetic bandwidth), to localize and

study the source under several other points of view [5].

It is then important that the communication between these observatories is the best of the efficiency: the joint-collaboration is determinant to provide a precise localization of the source in the sky and a complete set of data to study the object in all its details [6].

The main challenge when an electromagnetic observatory tries to follow up a signal from a gravitational-wave detector is the time spent in the communication of the signal, and in the adjustments of the instrument towards the right position in the sky. This can be achieved faster and precisely if the gravitational-wave detector is able to provide coordinates quickly and accurately.

A significant contribution to this goal could be added by the opening of the lower frequency window of ground-based gravitational-wave detectors. As seen in the previous section, the time to coalescence scales with frequency as $f^{-8/3}$. Lowering the frequency of observation would increase the time of observation before the coalescence. This would give more time for the electromagnetic detectors to adjust the position once they have received the coordinates. Moreover, the further the two inspiraling objects are from coalescence, the further they are from each other, thus increasing the volume of observation in the sky.

2.2.4. Duty cycle of the detector

The ground-based instruments are currently tuned to detect inspiraling binaries: the duty cycle of the detector is then very important for assessing its sensitivity. This quantity represents the time spent by the instrument in observing mode. As we will see in Chapter 5, this depends on how much time the detector can maintain resonance, i.e. on its stability.

---

[5]A general overview about multi-messenger astronomy can be found in [7]. An interesting paper about a multi-messenger GW-source detection and its implications is [8].

Duty cycle tells us for how much time the detector can follow the evolution of a signal in a given frequency band. Lowering the frequency band and increasing the sensitivity would improve the duty cycle, allowing the following of a signal for longer time, as we will see in Chapter 5. The consequent advantage is more precise waveform predictions based on these observations, in addition to the detection of a higher number of objects.

2.3. The goals of the gravitational-wave collaboration

The efforts of the scientific collaboration, towards the opening of the low frequency window, are devoted to the development of new technologies for active control of the noise sources, responsible for the lack of sensitivity below 30 Hz [9] [10] [11]. This has been the target of focus during the workshops dedicated to the low frequency band, which I attended between 2018 and 2021.

The goal of these meetings is to update the state-of-the-art of the topic and work together on new ideas and possible new solutions.

We will see in the next chapters that one of the most important noise sources, affecting the detectors in the low frequency range, is the seismic noise. The strategy investigated is based on the subtraction of this noise source: in particular, modelling, controls and reduction of the noise of seismic platforms are currently under examination for increasing the sensitivity below 30 Hz. Besides this, the study for the development of lower-noise sensors is also an up-to-date topic of discussion.

The importance of the opening of the lower frequency window has been widely outlined and highlighted [12]: the final goal is to reduce the noise coupling into the gravitational-wave signal, and an important contribu-

tion could be provided by the efforts of the people working on the seismic noise suppression.

It is in this frame that the work presented in this thesis takes place. The experiments carried out cover both the studies for noise suppression of seismic platforms on gravitational-wave detectors, and the development of new devices for sensing and reducing seismic motion.

3. Interferometry and Advanced LIGO

Most of the work reported in this thesis has been carried out in laboratories and on LIGO sites. In this chapter, I will briefly introduce interferometers and LIGO, and I will explain in detail only the structures at LIGO that have been the subject of study in this thesis work: this is essential to fully embrace the work reported in Chapter 5 in particular, and in general for the devices described in the whole thesis. The information contained in this chapter will often be referred throughout this thesis.

3.1. Interferometric detectors

The interaction of gravitation waves with two objects placed along the x axis produces effects on their distance $d = x_2 - x_1$ and hence the effect of the gravitational waves can be measured by looking at the variation of the distance of the masses involved.

A method to do it is to measure the time light takes to travel from one mass to the other: this is the basic principle of the *interferometer*.

As shown in Fig. 3.1, a laser interferometer is an instrument where a laser beam of wavelength λ is split into two beams which propagate in two perpendicular arms of the same length. At the end of each arm, a mirror reflects the beam back to be recombined with the other one. The recombined beam is then diverted to a photodiode.

3. Interferometry and Advanced LIGO
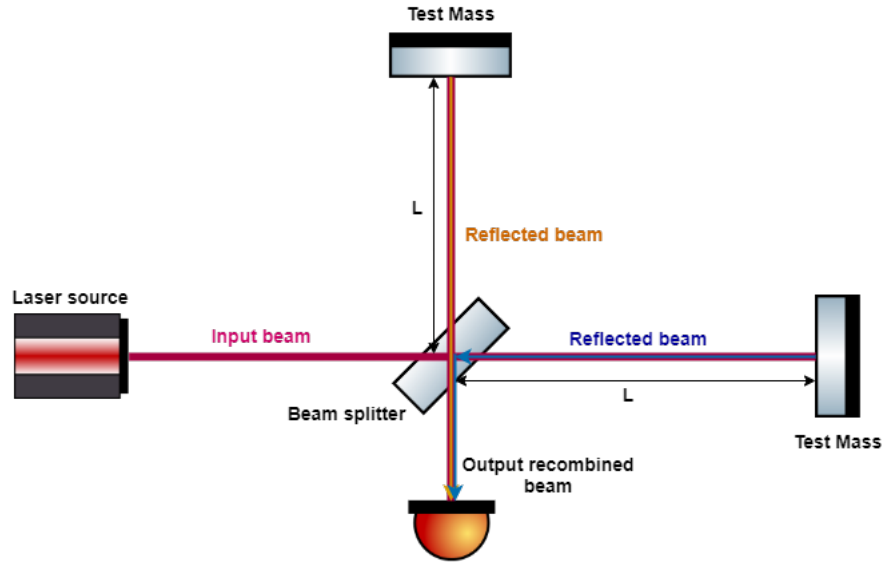
Figure 3.1.: Basic features of a Michelson interferometer.

If we consider the length of arms oriented to the x and y directions to be $L_x = L_y = L$, the power measured by the photodiode depends on the difference of path length between the two beams [2]:

$$P_{out} = E_0^2 \sin^2[k(L_x - L_y)] \tag{3.1}$$

where E_0 is the amplitude of the electric field generated by the laser source and k = $2\pi/\lambda$.

We know that the effect of a gravitational wave is to modify the distance between two masses: in the case of the interferometer the path length difference in the arms is proportional to the gravitational wave amplitude h [2]:

$$\Delta L = \frac{1}{2}hL \tag{3.2}$$

and hence the key feature of this detector is that the recombined beam brings a phase difference [1]:

$$\Delta\phi = \frac{4\pi hL}{\lambda} \tag{3.3}$$

---

[1]For details about interferometry refer to [2].

32

which results in a variation of the power measured:

$$P_{out} = E_0^2 \sin^2[k(L_x - L_y) + \Delta\phi]. \tag{3.4}$$

The amplitude of a gravitational wave is typically very small and corresponds to a variation of the arm length of the order of $\Delta L \sim 10^{-18}$ m. This means that, if we want to measure a considerable phase shift, the sensitivity of the instrument depends on the length of the arms.

Fabry-Perot cavities A useful way to increase the length of the arms is to make the laser beam travel back and forth inside an optical cavity delimited by two mirrors, called a *Fabry-Perot cavity*: here, thanks to the multiple reflections, the optical path length will be longer. This process returns a longer optical arm length, proportional to the quality factor of the cavity, which depends on the reflection coefficients of the two mirrors, named *Finesse* (F):

$$L_F \propto L\frac{2F}{\pi} \tag{3.5}$$

which gives a phase shift:

$$\Delta\phi_F = \frac{8hFL}{\lambda}. \tag{3.6}$$

A larger F results in an increased effective cavity length, hence a larger measurable phase shift.

3.2. Advanced LIGO

The goal of this work is to provide a contribution to the improvement of one of the interferometric detectors in use at present time, based in the USA: the Advanced Laser Interferometric Gravitational-wave Observatory (aLIGO).

The configuration of aLIGO is shown in Fig. 3.2: it is a Michelson interferometer adapted to include power recycling, signal recycling and 4km long Fabry-Perot arm cavities. The light source is a solid-state Nd:YAG laser of wavelength λ= 1064 nm, injected at a power between 5 - 125 W. The mirrors at the end of each arm, called End Test Masses (ETM), are made of fused silica and they are 34 cm $\times$ 20 cm in size and 40 kg in weight. A photodiode (PD) detects the power at the output. The optic able to split the injected beam into two parts along the arms is called a Beam Splitter (BS) and it is placed at 45° between the arms.

The instrument design is extremely intricate in all its details: this thesis will provide technical information useful for the understanding of the work made on specific sections of aLIGO.

There are two LIGOs in the USA, one in Hanford (WA) and one in Livingston (LA): some of the work that will be presented in the next chapters has been physically done in Hanford, in remote collaboration with Livingston team.

3.2.1. LIGO sensitivity and noise sources

The performance of LIGO, in terms of how far in the Universe it can detect gravitational waves and from which sources, depends on the sensitivity: this in turn depends on the quality of the technologies involved and on the natural limitations. Fig. 3.3 shows the sensitivity of LIGO during the first observation run and the main noise sources.

Advanced LIGO can be tuned to adjust the frequency band of detection: for each operational mode and detection bandwidth there is a gravitational wave source candidate, typically mergers of neutron stars (NS-NS) and black holes (BH-BH).

Noise sources make LIGO blind in some frequency windows: current technological limitations could be in principle overcome thanks to tech-
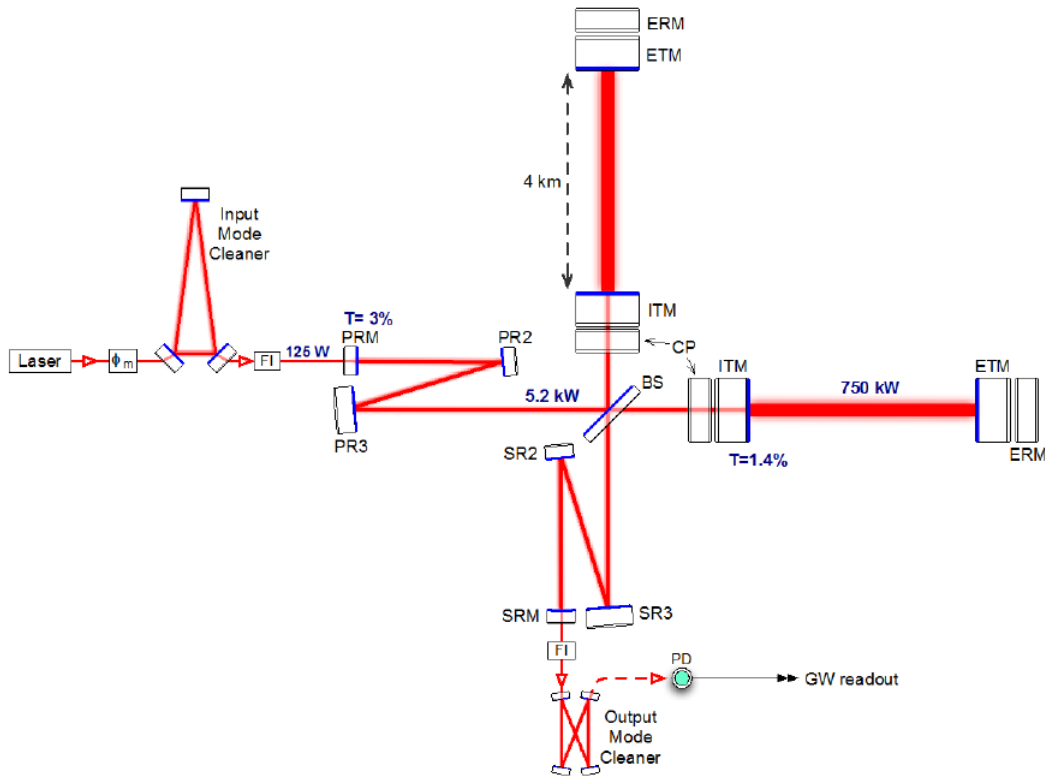
Figure 3.2.: Advanced LIGO configuration as proposed in [15]. As a second generation detector, it contains two Fabry-Perot resonant cavities in the arms, delimited by the Input Test Masses (ITM) and the End Test Masses (ETM), and two additional dual recycling cavities: the power recycling (PR) and the signal recycling (SR) cavities, whose core optics are all suspended to provide isolation from the environment. Compensation Plates (CP) take care of thermal effects occurring when high powers pass through the ITMs; mode cleaners in inputs and outputs keep the selected mode in resonance.

nological improvements, and this is what this present work is aiming to offer. The most important noise sources for LIGO are shown in the noise budget for LIGO Hanford (LHO) in Fig. 3.4.

Noises can be of fundamental, technical and environmental origin. Fundamental noises come from first principles, and they determine the ultimate design sensitivity of the instrument. They include thermal and
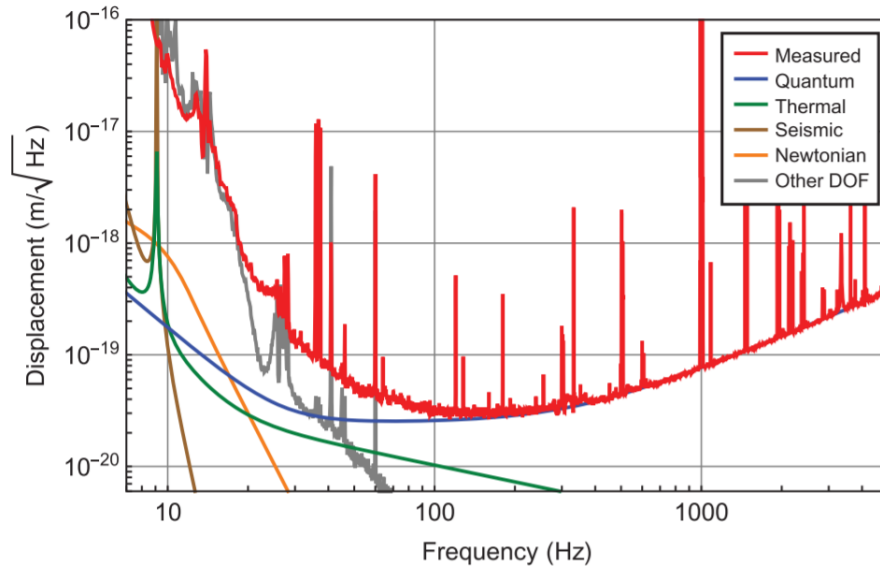
Figure 3.3.: Advanced LIGO sensitivity during the first observation run (O1) [16]. The sensitivity curve tells us that we can observe an event emitting gravitational waves of a given amplitude at a given frequency in an average observation time of 1 s. Since every source emits waves at a certain frequency and amplitude, lowering the curve means opening the viewing on currently hidden sources.
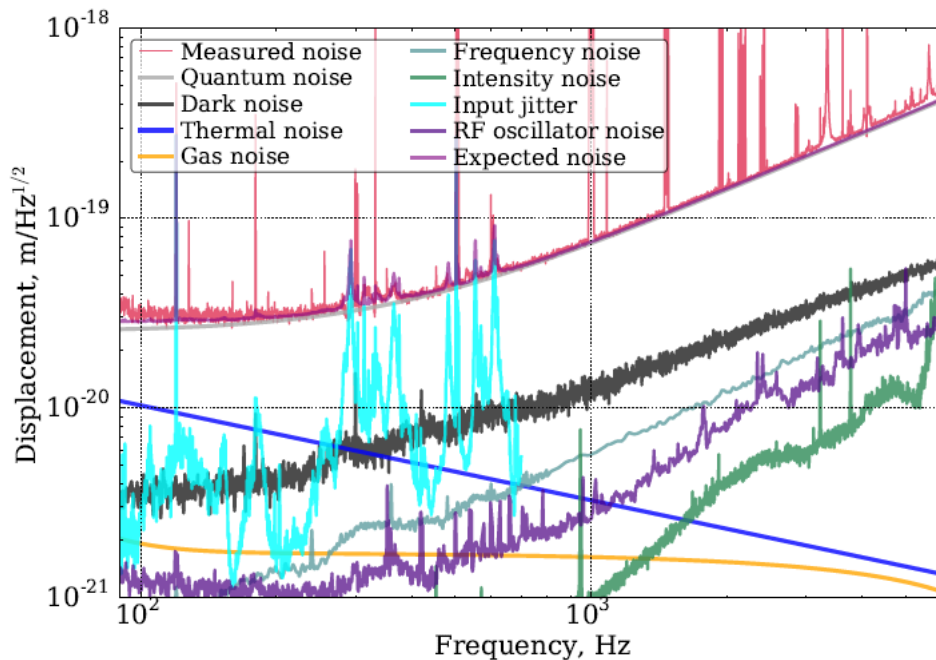
Figure 3.4.: Noise budget of LIGO Hanford Obsevatory [17].

quantum noises, and they cannot be reduced without a major instrument upgrade which involves structural changes. Quantum noise includes shot noise of the sensors, causing power fluctuations, and radiation pressure, resulting in a physical displacement of the test masses. Thermal noise arises from the suspensions and the optical coatings and dominates in the 5-100 Hz frequency range.

Technical noises arise from electronics, control loops, charging noise and other effects; environmental noises include seismic motion, acoustic and magnetic noises: these noises can be reduced once identified and carefully studied.

This thesis focuses on the improvement of the seismic isolation system. Seismic motion is measured using inertial sensors which are placed on the suspension benches. The residual motion affects the stability of the resonant cavities and limits the sensitivity of the detector in the low frequency band. The goal is to provide solutions to reduce the coupling of seismic motion to the interferometer and improve the detector sensitivity.

3.3. LIGO seismic isolation system

Every optic needs to be stable with respect to seismic motion, because movements in the mirrors will cause unwanted displacement of the laser beam on the optical surface, resulting in noise during the laser travel into the cavities and then at the output. The main mirrors (test masses and beam splitter) are suspended from a stabilized bench and every suspension chain is placed in vacuum chambers called *Basic Symmetric Chambers* (BSC). The auxiliary optics are placed on optical benches enclosed in the *Horizontal Access Module* (HAM) chambers.

The HAMs provide five levels of isolation, among which there is the Internal Seismic Isolation platform (HAM-ISI), where the auxiliary optics

3. Interferometry and Advanced LIGO
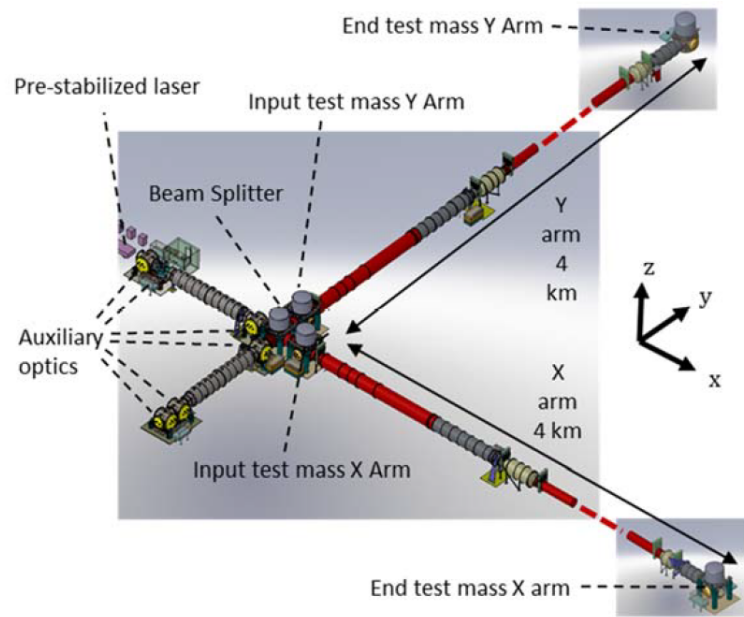
Figure 3.5.: Schematic view of the vacuum chambers enclosing the optics [18]. There are 5 BSCs and 6 HAMs, for a total of 11 vacuum chambers for each LIGO. Each chamber provides a mixture of passive-active isolation from seismic motion, using pendulums, inertial sensors and hydraulic systems.

are placed, giving both passive and active isolation. A detailed drawing in Fig. 3.6 shows the design of a HAM chamber.

The BSCs have a similar design as the HAMs, but they have two stages of ISI to support the suspensions isolating the test masses (Fig. 3.7).

The sensors on the chambers The devices dedicated to monitoring and providing feedback the seismic motion are inertial and displacement sensors, which are horizontal and vertical, according to the different motion they need to sense. Currently, no sensors for tilt motion are installed on the platforms. Actuators are paired to each sensor, for active isolation of the sensed noise. The vertical displacement sensors are called Capacitive Position Sensors and are placed between every stage of every chamber: they measure the relative motion between the plat-
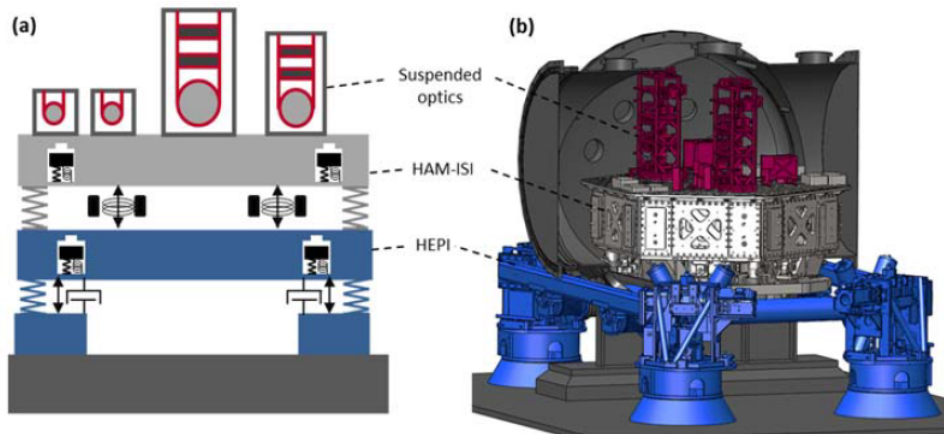
Figure 3.6.: Schematic (a) and CAD model (b) of a HAM chamber [18]. Suspensions of auxiliary optics provide levels of passive isolation above 10 Hz. The ISI platforms where the suspensions live are optical tables actively isolated via low noise inertial sensors at low frequency (~ 0.1 Hz). The hydraulic attenuators of the *Hydraulic External Pre-Isolator* (HEPI) and the geophones provide isolation from ground motion.

forms. These are the sensors we will use in Chapter 5. The vertical and horizontal inertial sensors with the dedicated actuators are placed on the platforms, underneath the optical tables, measuring the seismic motion in the horizontal and vertical directions. The position and the use of these sensors are different for HAM and BSC chambers, depending on the number of stages and the presence of the suspensions. The calibration and the specific role of each sensor into the seismic isolation system can be found in [44], with references to the covered range of frequencies in [19].

Stabilizing the ISI Part of the work presented in this thesis focussed on the enhancement of the performance of the active isolation system of the ISIs for both BSC and HAM chambers.

Active isolation implies a sensing system of the noise to reduce and a control system to compensate the disturbance. Each platform includes
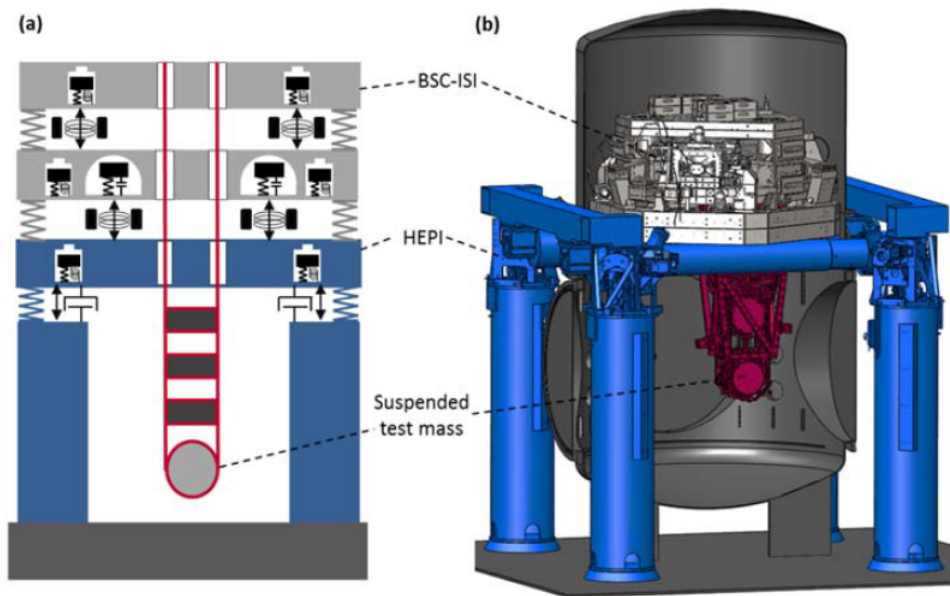
Figure 3.7.: Schematic (a) and CAD model (b) of a BSC chamber [18]. The active isolation is similar to the one exposed for HAM chambers. The two ISIs provide two stages of isolation while the suspensions are designed to be quadruple pendulums, for a total of seven levels of isolation.
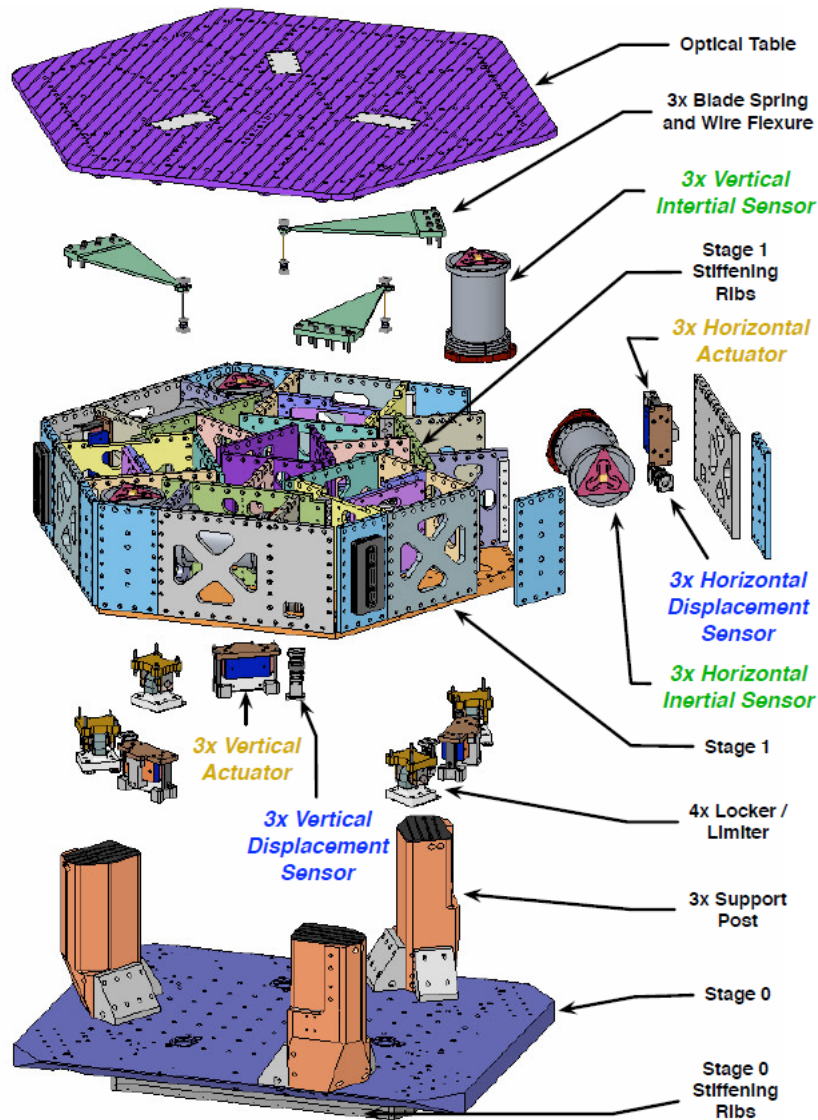
Figure 3.8.: Example of ISI inertial sensor scheme for a HAM chamber (figure taken from [44]). All the main inertial and displacement sensors involved in the seismic isolation are shown in their locations. The CPSs are the displacement sensors located between stages to measure the relative position. For the BSC chambers, the setup is similar.

relative position sensors, inertial sensors and actuators, working in all degrees of freedom.

The control loop of a generic ISI stage on the X degree of freedom is

simplified in the block diagram in Fig. 3.9. The platform motion is the sum of the input disturbance and the contribution from the control signal and it is measured by relative position and inertial sensors. This motion is then low- and high-passed via filters suitably built to fit the requirements and tuned to obtain the best performance combining the best results of both filters. This technique is called *blending*, and the frequency where the relative and the inertial sensors contribute at their best is called the *blend frequency*. The result of this blend is called the *super sensor*. The output of the super sensor feeds the feedback loop, where the actuators close the loop [2].

The *sensor correction loop* takes the ground motion signal from an inertial instrument, filtering it before adding it to the relative sensor signal. This filter is needed because the sum of the motions from the ground inertial and the relative sensors can in principle provide a measurement of the absolute motion of the platform. However, the ground sensors are affected by low frequency noise and need to be suitably filtered.

---

[2]A general overview of control loops theory is given in Appendix B
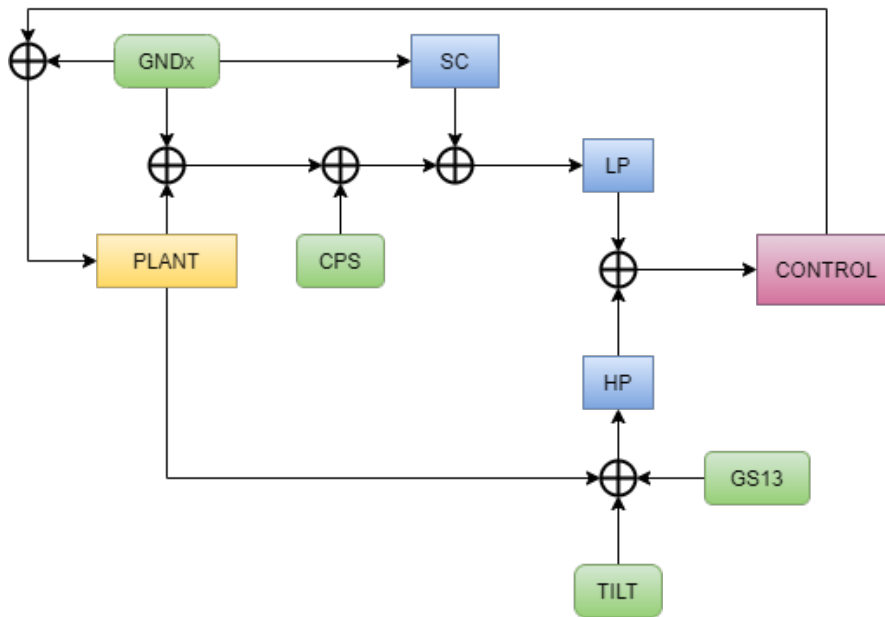
Figure 3.9.: Control loop of a generic HAM-ISI platform. Similar block diagrams can be applied for BSC-ISI platforms, including relative position sensors between the two stages of ISIs. **Green:** there is an inertial sensor measuring the ground motion along the x axis (GNDx), a Capacitive Position Sensor (CPS) measuring relative motions between the platform and the ground. Rotational sensors take care of tilt motion and GS13s are seismometers measuring seismic motion. Tilt and GS13 sensors are both placed on the platform. **Blue:** the Sensor Correction (SC) filter is typically a Finite Impulse Response (FIR) designed to provide required magnitude and phase match at 100 mHz (where isolation is needed). High- and low-pass filters (LP and HP) manipulate the signals from the low and high frequency sensors and are blended to form the super sensor, whose output is sent to the control loop in **pink**. The overall corrected signal is then sent to the plant (**yellow**), which represents the processing phase for platform motion actuation.

3.4. LIGO Length Sensing and Control

Length sensing and control (LSC) is a crucial feature of LIGO because the cavities need to be stable and resonant for as long as possible. This requires feedback controls between optical resonators and low-noise sensing systems to avoid noise coupling into the gravitational-wave readout.

There are several resonant cavities involved in this scheme, all important to guarantee the best performance on the sensitivity of the instrument. As we saw in Fig. 3.2, the resonators are the two Fabry-Perot cavities in the arms, the power recycling and the signal recycling cavities. The Fabry-Perot ones assure a higher sensitivity thanks to the beam bouncing inside the cavity multiple times, increasing the time spent by the light inside the arms and hence, the interaction time with a gravitational wave. The power recycling cavity is used to recover losses from power in the injection bench due to light reflected back to the laser source: this helps to increase the power travelling in each arm. The signal recycling cavity is placed at the output of the detector and is used to tune the detector to a specific observing bandwidth.

The main disturbance affecting the stabilization of the resonators is the ground motion, acting on the position of the optics and that can not be reduced by the passive isolation systems below 1 Hz. This means that an active isolation and a feedback control are required.

The most important cavity lengths to keep stable are highlighted in Fig. 3.10; each length path between optics contributes to a specific signal monitored to maintain the cavities in resonance. The signals are the Signal Recycling Cavity Length (SRCL), the Power Recycling Cavity Length (PRCL), the MICHelson (MICH), the Common Arm length (CARM) and the Differential Arm Length (DARM) and they are described by the fol-

44

lowing relations between lengths:

$$DARM = L_x - L_y$$

$$CARM = \frac{L_x + L_y}{2}$$

$$MICH = \frac{(l_x - l_y)}{2}$$

$$PRCL = l_p + \frac{l_x + l_y}{2}$$

$$SRCL = l_s + \frac{(l_x - l_y)}{2} = l_s + MICH$$

In particular, DARM is exactly the gravitational wave signal and thus the most important one to monitor and to keep stable.

During the time at LIGO Hanford, some of the work has been devoted to the optimization of the time spent by cavities in resonance (i.e. the duty cycle), using a new concept based on the communication between the optics and the platforms where they are placed.

As we will see, time in stable mode is crucial to assure higher chances of detection of gravitational-wave candidates. Small disturbances during the operational mode can compromise the detector while observing, losing stabilization (lock). This means that operators need to spend time to lock the instrument again and reset it in observing mode, time that is precious and that could instead be spent detecting events.
This work in particular intends to give a contribution to the improvement of the sensitivity and stabilization of LIGO at low frequencies.
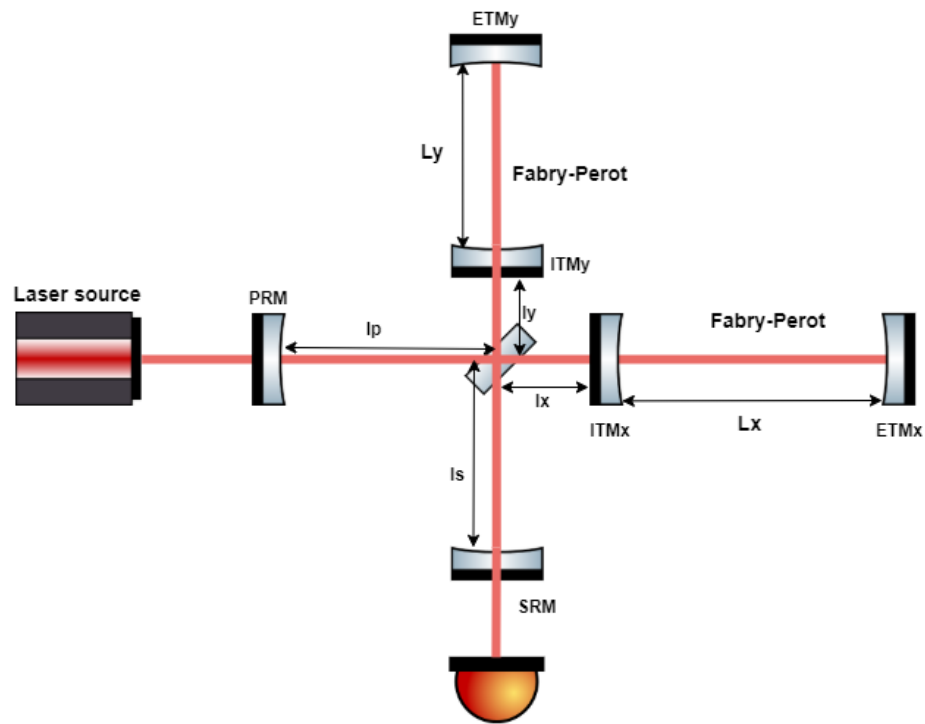
Figure 3.10.: Cavity lengths involved in the sensing and feedback control for stabilization of resonators. The PRM is the Power Recycling Mirror, which includes the power recycling setup with three mirrors inside two chambers. The SRM is the same concept for the Signal Recycling cavity.

Part II.

Lowering seismic motion

4. Optical levers for tilt motion reduction

The sensors dedicated to measure the seismic motion need to account for horizontal, vertical and tilt displacements in all degrees of freedom in order to be efficient: the technology for their improvement is currently pushing and competing on sensing as low seismic motion as possible. On an interferometric detector, seismic motion affects the stabilization of the supports where the optics lie. This produces unwanted noise at low frequencies (< 30 Hz), which reduces the sensitivity of the detector. During the first year of my PhD studies, I investigated the use of optical levers to reduce tilt motion: a device has been built at UoB, and tested at the Albert Einstein Institute (AEI) in Hannover in June 2019.

The content of this chapter has been re-adapted from my Mid-term report [21]. A poster about this project has been presented at the LVK meeting in Maastricht (September 2018) [22].

4.1. Inertial sensors affected by tilt-coupling

There are many contributions affecting aLIGO sensitivity at low frequency. One of the most investigated is the tilt of HAM vacuum chamber of ISI platforms, which dominates above 1 Hz [23].

For the rotational degrees of freedom, getting a good estimate of ground motion is not trivial because no rotational sensors capable of measuring the ground motion in rotation at low frequencies have been installed yet

4. Optical levers for tilt motion reduction

on aLIGO ISI platforms [24].

However, there is a possible way to measure angular displacements of the benches very precisely (10^{-12} rad/$\sqrt{Hz}$) and to actively control them: this could be done by optical levers. In the following, we will analyse the main contributions to tilt motion and we will see how optical levers could be useful to suppress this motion.
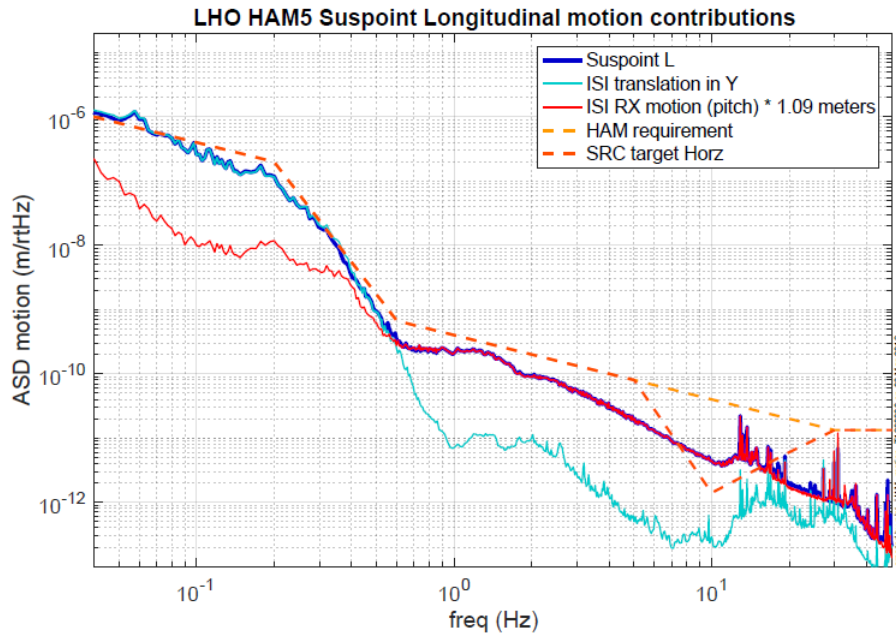
Figure 4.1.: Plot of the contributions to the Suspension point L motion at LHO HAM5. The pitch (RX) contribution dominates above 1 Hz (Figure taken from [23]).

Horizontal sensors One of the most important problems, in order to achieve good isolation, is the sensitivity of the horizontal sensors to rotation. If we could independently measure the rotation, we could calculate the true translational motion.

Referring to Fig. 4.2, when a rotation around the center of mass of the sensor occurs, an additional term to the equation of motion (F_{tilt}) appears:

Figure 4.2.: Basic sketch of horizontal sensor tilting.

$$F_{tilt} = mg\sin\theta \qquad (4.1)$$

where m is the mass and g = 9.8 m/s^2 is the gravitational acceleration. So we have the following situation:

$$m\ddot{x} = -kw - b\dot{w} + F_{tilt}, \qquad (4.2)$$

where x is the direction of motion, k is stiffness and b is damping of the spring.

We assume that the angle is very small, in such a way $\sin\theta \simeq \theta$. So the equations of motion are:

$$m\ddot{x} = -b(\dot{x} - \dot{y}) - k(x - y) + mg\theta, \qquad (4.3)$$

where x is the displacement of the mass and y is the displacement of the support of the sensor.

Since we want to study the system in the frequency domain, we substitute $w = x - y$ and apply the Laplace transform:

$$m(W + Y)s^2 = -bWs - kW + mg\Theta. \qquad (4.4)$$

After some manipulations, we obtain:

$$W = \frac{ms^2}{ms^2 + bs + k}\left(-Y + \frac{g}{s^2}\Theta\right). \qquad (4.5)$$

51

4. Optical levers for tilt motion reduction

where W is the measured quantity, Y and Θ are the quantities we are interested in. Remembering that s = $i\omega$ in a steady-state situation, we have:

$$W(\omega) = \frac{-m\omega^2}{-m\omega^2 + ib\omega + k} \left(-Y - \frac{g}{\omega^2}\Theta\right).$$ (4.6)

The relative sensitivity to translation and tilt are included in the second term in brackets. We expected this result, as the general one is that, for a horizontal seismometer, the ratio of the sensitivity to rotation (seismometer signal per radian of angle) to the sensitivity to horizontal motion (seismometer signal per meter of translation) at a particular frequency ω is:

$$\frac{rotation\ response}{translation\ response} = \frac{g}{\omega^2}.$$ (4.7)

If we know the size of our system, it is possible to calculate the angle θ. Since we have a factor ω^2 at the denominator, it has more contributions at low frequencies: the contribution given by the tilt is decoupled and summed to the transfer function.

When the seismometer is tilted, its sensitivity to angles increases as g/ω^2. So, if we have some sort of seismic system measuring ground motion with horizontal seismometers, we could in principle measure this contribution and remove it by subtracting from the transfer function.

Vertical sensors If we are dealing with vertical sensors, referring to Fig. 4.3, in presence of tilt we have:

$$m\ddot{x} = -b(\dot{x} - \dot{y}) - k(x - y) + mg\cos\theta.$$ (4.8)

Since $cos\theta \sim 1 - \theta^2/2$, the θ^2 is second order and negligible for changes of angles.

52
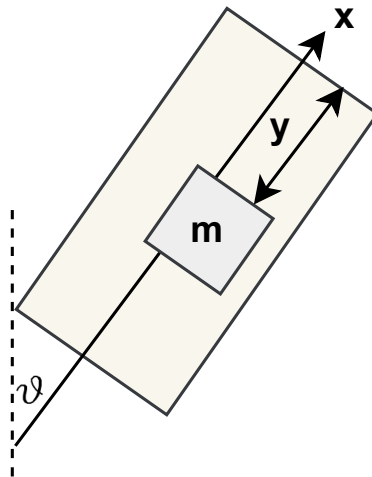
Figure 4.3.: Tilting of vertical sensor.

4.2. Optical levers

In general, an optical lever is a convenient device that makes use of a beam light and a position sensor to measure a small displacement and thus to make possible an accurate measurement of angles. This method is a very useful approach in sensitive non-contacting measurements. A light source, typically a laser, impinges on an optic reflecting the beam on a position device, which records any displacement of the beam, i.e. of the optic.

When the optic is tilted by an angle θ, we have the situation illustrated in Fig. 4.4: if all the distances are known, we can compute the angle θ.

What if we have both horizontal and vertical seismometers on the same bench, as on aLIGO? In this case, we have two instruments that are sensitive to horizontal and vertical ground motion at the same time. When the bench is tilted, they are tilted at the same time of the same angle, but they are not affected in the same way, as we have seen, but we are not able to deduce the tilt motion at low frequency because of the limitations given by the sensor noises.

If we could measure both vertical and horizontal motions and decouple the contribution of the tilt for the horizontal one, we could know exactly

4. Optical levers for tilt motion reduction
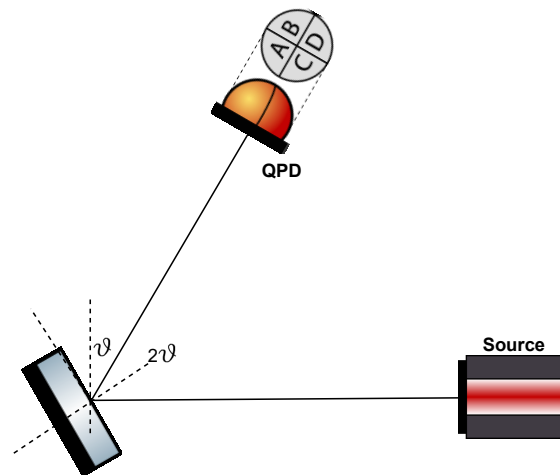
Figure 4.4.: Concept of the optical lever working principle: when the optic is tilted by a known angle, the displacement is detected by the photodiode.

the amount of corrections the actuators have to perform.

With optical lever systems we can measure the angle of the tilt, even if it is extremely small: in this way we could be able to directly measure the tilt angle θ and apply corrections to the horizontal sensor through a dedicated active system.

The device described in this chapter should involve sensing and actuation for the seismic motion on aLIGO. The position device can not be set on the same bench where the other sensors are, because it would be affected by the same ground motion. So it has to be placed on another bench, at some distance L, and an actuation system is associated to it in order to adjust the tilt of the bench under exam. The angular sensitivity increases with the distance L. Moreover, even the bench where the position device is set needs to be stable: another optical lever could be placed on it, with the associated actuation, mirroring the first one and keeping both platforms stable. A basic picture of the whole system is shown in Fig. 4.5.

The purpose when thinking of interferometers is to help reducing the
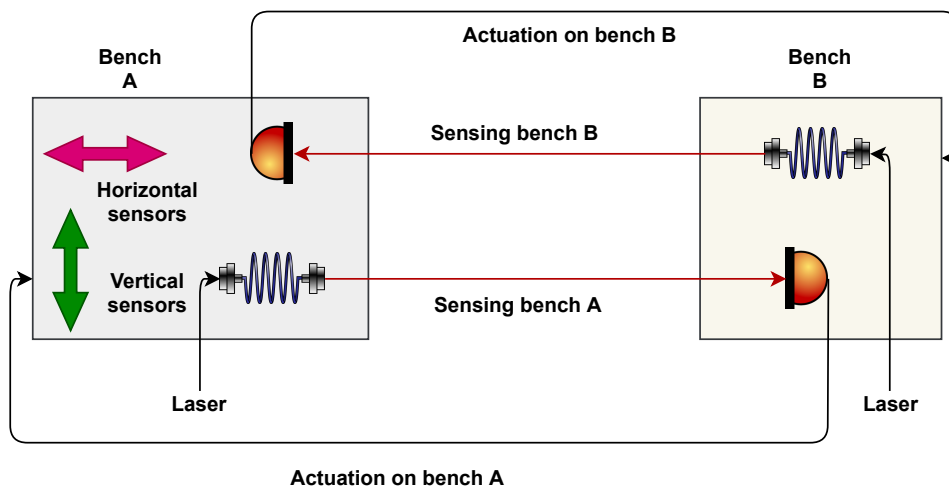
Figure 4.5.: Basic principle of the optical lever used for sensing and actuation for seismic isolation.

RX motion on the HAM chambers that propagates into the suspensions, proving a displacement of the suspension point and hence introducing noise in the cavities.

4.3. Experiment design

In order to understand the feasibility of the project in terms of performance, we have to estimate the noise budget and the sensitivity of the system.

Let's start from the block diagram of the system, in Fig. 4.6.
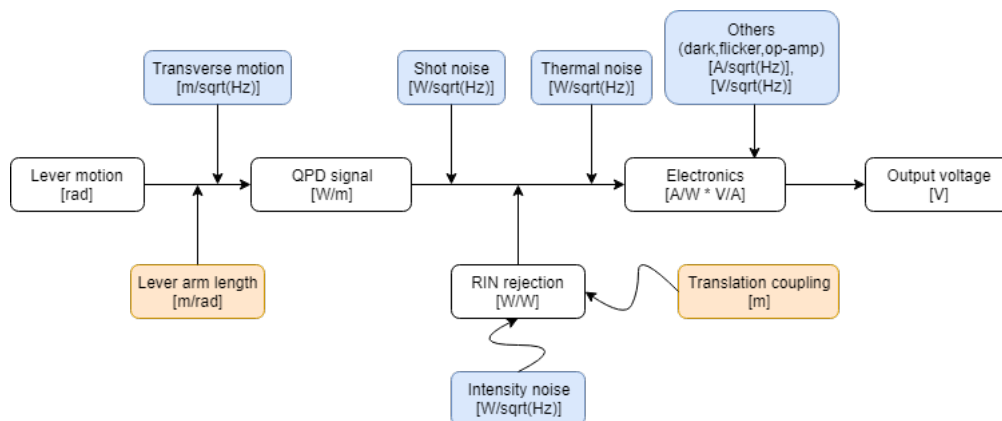
Figure 4.6.: Block diagram of the optical lever system.

In the block diagram all the noises we have to deal with are described: the most relevant in terms of contributions are the shot and the thermal noises; then there are all the noises related to the electronics, like dark current, flicker and op-amp noises, usually given in the datasheet of the devices.

Beyond them, we have to consider the relative intensity noise (RIN), due to instabilities in the laser intensity: this kind of noises reduces the signal-to-noise ratio, limiting the performance of the electronic transmission. This may be reduced by making the signal positions independent of illumination intensity.

The translation coupling noise due to the motion of the platform where sensors are set is also considered: this gives a contribution in the measurement in terms of linear displacement, while we are measuring the angular motion of the platforms.

4.3.1. Quadrant Position Devices

The Quadrant PhotoDiodes (QPD) are the position devices usually involved with optical levers. They consist of four distinct and identical quadrant-shaped photodiodes that are separated by a small gap (typically, $\sim$0.1 mm) and together form a circular detection area capable of providing a 2D measurement of the position of an incident beam.

When light is incident on the sensor, a photocurrent I is detected by each quadrant Q in Fig. 4.7.

The normalized coordinates (X, Y) for the beam's location depend on the detected photocurrents and are given by the following equations:

$$X = \frac{(I_2 + I_3) - (I_1 + I_4)}{I_1 + I_2 + I_3 + I_4} \tag{4.9}$$

$$Y = \frac{(I_1 + I_2) - (I_3 + I_4)}{I_1 + I_2 + I_3 + I_4} \tag{4.10}$$
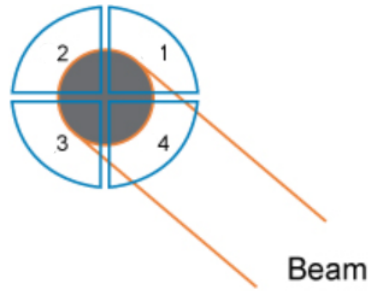
Figure 4.7.: View of the segmented photodiode. Each quadrant Q receives a photocurrent which is the signal responsible for any displacement detection: depending on which quadrant is receiving more or less photocurrent, it is possible to derive the position of the beam on the active area.

If a symmetrical beam is centred on the sensor, four equal photocurrents will be detected, resulting in null difference signals and, hence, the normalized coordinates will be (X, Y) = (0, 0). The photocurrents will change if the beam moves off center, producing different signals that are related to the beam displacement from the center of the sensor.

Spot position and displacement

At the light of what we have seen about QPDs, we have to compute where the beam is on the photodiode: the coordinates of the beam depend on the photocurrents. If we are dealing with a Gaussian beam, they are proportional to the Gaussian intensity:

$$I(x) = \frac{P_0}{\pi w_x^2} e^{-2\left(\frac{x}{w_x}\right)^2}, \tag{4.11}$$

for coordinate x, the same for y; w_x is the beam size (radius) in x direction and represents the distance from the x axis to which the amplitude reduces by $1/e$ and the intensity by $1/e^2$; P_0 is the input power.

If we want to obtain the signal in terms of power, we should integrate the Gaussian intensity. However, if the spot displacement is small, and

4. Optical levers for tilt motion reduction

assuming that the variation of the spot size is negligible with respect to the spot displacement ($\Delta w \ll \Delta x$), we can apply a linear approximation. So we have:

$$P_x = \frac{P_0}{\pi w_x^2} \int_0^R e^{-2\left(\frac{x}{w_x}\right)^2} dx, \tag{4.12}$$

where R is the radius of the detector.

The integral of the Gaussian function is the Error Function, defined as:

$$erf(x) = \frac{2}{\sqrt{\pi}} \int_0^x e^{-t^2} dt. \tag{4.13}$$

So we have:

$$P_x = \frac{P_0}{\pi w_x^2} \int_0^R e^{-2\left(\frac{x}{w_x}\right)^2} dx = \frac{P_0}{\pi w_x} \frac{\sqrt{\pi}}{2} \sqrt{2} w_x erf(x). \tag{4.14}$$

The first term of the Taylor expansion of the error function is erf(x) $\approx$ $\frac{2}{\sqrt{\pi}}x$, so we have:

$$P_x = \frac{P_0}{\pi w_x^2} \frac{\sqrt{\pi}}{2} \sqrt{2} w_x erf(x) \approx \sqrt{2} \frac{P_0}{\pi w_x} x. \tag{4.15}$$

Using the linear approximation, the displacement in x is given by:

$$\Delta x \approx \frac{\pi w_x}{\sqrt{2} P_0} \Delta P_x; \tag{4.16}$$

and the ratio between the variation of the power and the displacement in the x direction is given by:

$$\frac{\Delta P_x}{\Delta x} \approx \sqrt{2} \frac{P_0}{\pi w_x} [W/m]. \tag{4.17}$$

The same computation gives the result for the coordinate y:

$$\frac{\Delta P_y}{\Delta y} \approx \sqrt{2} \frac{P_0}{\pi w_y} [W/m]. \tag{4.18}$$

In order to estimate the resolution of the device and provide an estimate of its performance, we need to account for the noises coming from the QPD and external sources.

4.3.2. Photon shot noise

Because of the fact that the working principle of the QPD is based on tracking the motion of the centroid of power density, it is useful to compute the contribution of the shot noise.

The shot noise is the fluctuation of the photon counting on the photodetector. This fluctuation obeys the Poisson statistics, but for a large mean number of photons ($< N >\gg 1$), it approaches the Gaussian one, with standard deviation $\sigma = \sqrt{< N >}$.

If P_0 is the input power and ω is the frequency, the number of photons on the photodiode in a given time interval t is:

$$< N >= \frac{P_0 t}{\hbar \omega};$$

(4.19)

the fractional fluctuation of the number of photons is then:

$$\frac{\sigma}{< N >} = \frac{1}{\sqrt{< N >}} = \sqrt{\frac{2\pi \hbar c}{P_0 t \lambda}}.$$

(4.20)

The fractional fluctuation of the input power σ_p is given by the fractional fluctuation of the number of photons:

$$\frac{\sigma_p}{P_0} = \frac{\sigma}{< N >},$$

(4.21)

$$\sigma_p = P_0 \frac{\sigma}{< N >} = P_0 \sqrt{\frac{2\pi \hbar c}{P_0 t \lambda}},$$

(4.22)

For t=1 s:

$$\sigma_p = \sqrt{\frac{2\pi \hbar c P_0}{\lambda}}.$$

(4.23)

So the fractional fluctuation of the power scales as the square root of the input power. Since QPDs are sensitive to shape and density distribution of the incident beam, a beam which does not have a Gaussian power distribution will be centred based on the power, rather than the geometric center of the beam, so it will be more affected by shot noise.

4. Optical levers for tilt motion reduction

With the laser wavelength λ = 1064 nm and an input power P_0 = 1 mW that we chose for this experiment, we obtain:

$$\sigma_p = 1.4 \times 10^{-11} \frac{W}{\sqrt{Hz}}. \tag{4.24}$$

4.3.3. Thermal noise

The other, important noise affecting the measurements is the thermal noise due to the transimpedance resistor of the photodiode R. It is given by:

$$V_{th} = \sqrt{\frac{4k_B T}{R}} \frac{A}{\sqrt{Hz}}, \tag{4.25}$$

where k_B = 1.38 $\times$ 10^{-23} J/K is the Boltzmann constant, T is the temperature. In order to obtain the thermal noise in units of W/$\sqrt{Hz}$ we divide by the responsivity ρ (in A/W). For a 1064 nm laser wavelength the responsivity is typically 0.2 A/W.

To compute R, consider that the output voltage from the photocurrent is given by:

$$V_{ph} = P_0 \rho R, \tag{4.26}$$

and because the output voltage is limited by the range imposed by the interferometer itself, i.e. [+10, -10] V, we have that R = 5 $\times$ 10^4 Ω.

So, considering T = 300 K at room temperature, we have:

$$T = 1.47 \times 10^{-12} \frac{W}{\sqrt{Hz}}. \tag{4.27}$$

4.3.4. Resolution

Now that we have extracted the noise contributions to our system, we can determine the sensitivity α of the sensor. This means that we want to know the efficacy of our system in measuring angles (in rad/$\sqrt{Hz}$).

So, according to the block diagram in Fig. 4.6, to obtain the angular measurement we have that:

$$\alpha = shot\ noise \times \frac{1}{signal} \times \frac{1}{Length}, \tag{4.28}$$

$$\alpha = \sigma_p \times \frac{1}{\sqrt{2}\frac{P_0}{\pi w_y}} \times \frac{1}{L}, \tag{4.29}$$

$$\alpha = 1.4 \times 10^{-11} \times \frac{1}{2.22} \times \frac{1}{10}, \tag{4.30}$$

$$\alpha = 3 \times 10^{-12} \frac{rad}{\sqrt{Hz}}. \tag{4.31}$$

This value is of the order of magnitude of the sensitivity of optical levers anticipated earlier.

4.3.5. Estimated sum of contributions

In order to obtain a plot of the noise budget for the optical lever prototype, we need to take into account some more elements to add to the ones just computed:

- The motion along z of the platforms is used as noise: however, at low frequency, most sensors are not sensitive to this motion so what we need is a differential motion between HAM chambers (say HAM4 and HAM5 for this derivation); the best estimation we have is the platform z motion measured by GS13s. This motion is given by channels of LIGO Livingston data;

- The best performance of current tested optical levers is the one tested at the AEI and shown in Fig. 4.4 of reference [25];

- The ground θ motion of the chambers is given by the Beam Rotation Sensors (BRS) and used as noise source. This motion is taken from channels of LIGO Livingston data;

4. Optical levers for tilt motion reduction

- The RX motion is given by the CPS on HAM4 and HAM5 and it is used for comparison with the optical lever performance. This motion is taken from channels of LIGO Livingston data.

The optical lever performance reported in [25] takes into account the motion along the x axis, the spot displacement of the beam on the photodiode and the displacement of the photodiode itself.

The differential Z motion is given by the difference between the z motion measured by the GS13 sensors on HAM4 and HAM5:

$$\Delta Z = (GS13_z^{HAM5} - GS13_z^{HAM4}). \tag{4.32}$$

The contribution from the GS13 needs to be manipulated to give rad/$\sqrt{Hz}$: this is done converting the measured velocity to displacement. All the noise sources are divided by the lever arm, in order to obtain an estimation in radians.

A low pass filter (LP) at 1 Hz is applied to the BRS motion and a high pass filter (HP) is applied to the ΔZ motion at 0.1 Hz: we use the filters to estimate the motion, since we know that the measured signals are limited by noise where we are applying the filters.

Since all noises are independent from each other, summing all the elements in quadrature, we have the total noise performance of the optical lever, which is shown in the plot in Fig. 4.8: the plot shows that the improvements that optical levers can give are limited to a restricted range of frequencies and that they suffer the differential Z motion contribution below 0.1 Hz. Given the technical difficulties of developing and installing optical levers (see following sections), the effort would only be worthwhile if the Z motion was improved via better sensors.

$$OpLev_{noise} = \sqrt{(OpLev_{AEI})^2 + (\theta_g^{BRS})^2 + (Thermal)^2 + (Shot)^2 + (\Delta Z)^2}. \tag{4.33}$$
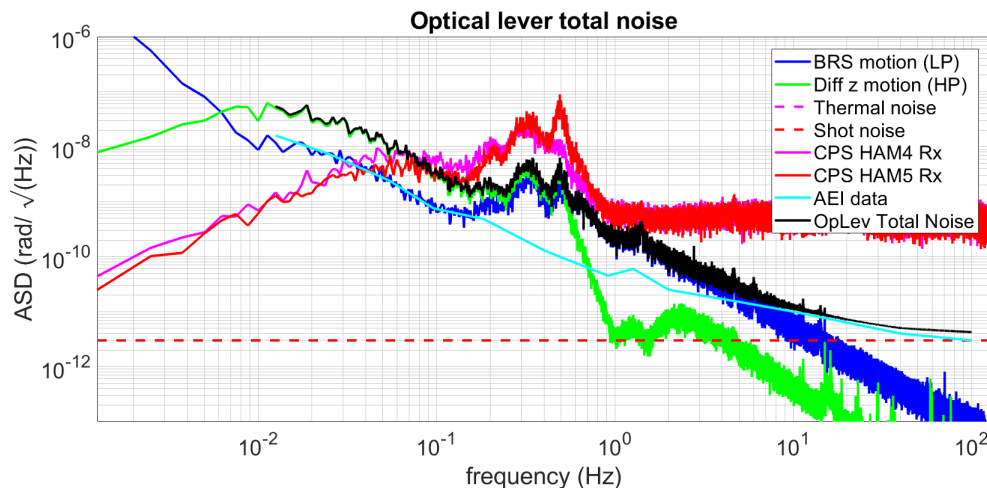
Figure 4.8.: Optical lever total noise budget. This plot shows that our model predicts significant signal-to-noise ratio improvement from ~0.15 Hz to 1 Hz (Vs CPS), but we are limited by the differential Z motion over a wide band.

4.4. Design of the prototype

The optical design has been simulated, taking into account some general constraints of the sensor: generally, the QPD diameter is around 10 mm, so the beam size should not exceed 1-3 mm; gaps in quadrant photodiodes are of the order of tens μm. Moreover, it is ideal for the setup to be compact: the prototype has been design to lie on a [75 mm × 36 mm] platform.

The chosen light source is a 1064 nm wavelength fiber-coupled Nd:YAG solid-state laser. Because of the fact that the beam size impinging on the photodiode has to be around 1 mm, a fiber collimator is used at the fiber output, and a plano-convex lens is used to focus the beam at the photodiode. In this way, with the chosen collimator, the beam size at its output is 1.38 mm. This is considered the starting point for the free propagation of the laser beam. The use of the collimator ensures that the beam size enlargement after a length L of propagation is minimized: according to the simulated free propagation, after 10 m the beam size is 2.8 mm. The focussing lens of focal length 150 mm is inserted 10 cm

before the photodiode. In this way, the beam size impinging on the lens surface is 2.79 mm $\ll$ 12.7 mm of lens diameter. The beam size at the photodiode is 0.95 mm. The basic sketch of the optical system is shown in Fig. 4.9.
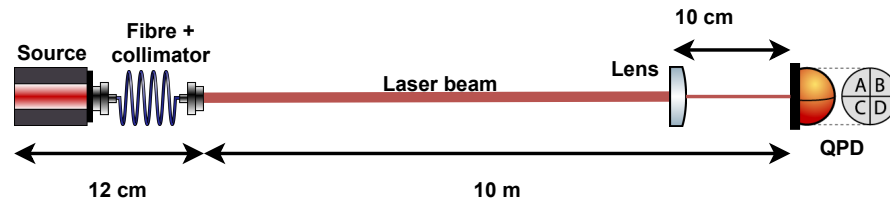
Figure 4.9.: Basic sketch of the lever optical design (not in scale).

The prototype and its own pre-amplifying electronics have been built at UoB (Fig. 4.10) and tested in air and in vacuum at the AEI. The purpose is to calibrate the prototype with the electronics from UoB in vacuum conditions and test the sensitivity of the device to angular displacements. This first step is necessary for a good sensing system characterization.
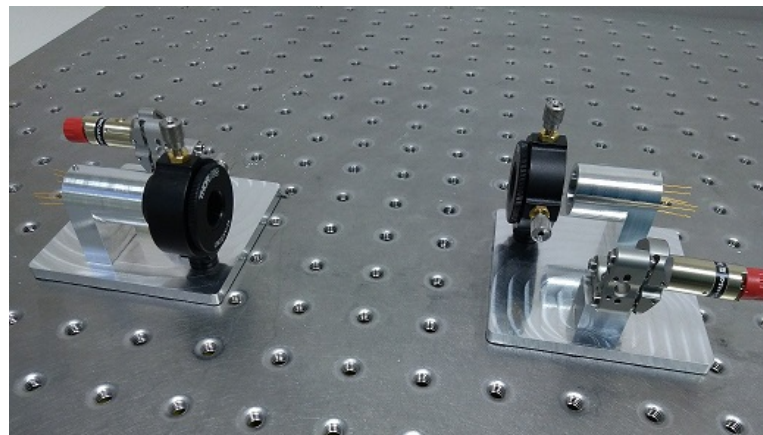
Figure 4.10.: Photo of the optical lever prototypes as built at UoB. In this picture, the devices are not connected to electronics. Each platform hosts a laser source and a sensor. Each sensor is covered by a tube to avoid spurious light on the active area, and the focusing lens is placed at the suitable distance from it.

4.5. Test at the AEI

The aim of the collaboration was to test the optical lever prototype in vacuum. We used the South bench of the 10 m prototype at AEI in Hannover.

The device and part of its electronics have been adjusted in order to match the requirements for a measurements using a Control and Data System (CDS) and facilities at AEI.

The pin configuration of the QPDs has been reset because the AEI electronics is set on a different one. It has been changed to the following:

- Q1: PIN 1 to PIN 1

- Q2: PIN 2 to PIN 2

- Q3: PIN 3 to PIN 6

- Q4: PIN 4 to PIN 7

- BIAS: PIN 5 to PIN 4

Two adaptor cables have been built to connect the UoB boxes to the QPDs with the new pin configurations.

To isolate the QPD, a small shield of plastic has been added to the QPD mount and the related metal screws have been changed with peek screws. Because of the presence of the new plastic layer, the height of all other components of the platforms has been adjusted.

Every component has been vacuum-cleaned using an ultra-sonic bath.

4.5.1. Installing the device

After cleaning, we installed the device into the South bench of the 10-m prototype. Due to the availability of the bench, only one fibre could be

connected to one collimator; consequently, only one QPD has been connected.

The lever arm has been set to be 20 cm: with the optical configuration foreseen for this lever arm the spot size on the photodiode is w $\simeq$ 1 mm. The power on that point is P = 3.5 mW.

Summarizing, the prototype is ready for the test with the specifications listed in Tab 4.1.

Beam size at QPD	w = 1 mm
Power at output	P = 3.5 mW
Displacement	$\triangle$ x = 2.22 $\times$ 10^{-3} m
Lens focal lenght	F = 150 mm
Shot noise	SN = 75 nV/$\sqrt{Hz}$
Responsivity Si @ 1064 nm	ρ = 0.2 A/W
Thermal noise	T = 21 nV/$\sqrt{Hz}$
Op-amp noise	OP = 8,8 nV/$\sqrt{Hz}$

Table 4.1.: Specifications of the optical lever prototype tested at the AEI.

Preliminary test in air To test if everything was set in the best way, we performed a first measurement in air, using one of the AEI pre-amp boxes connected to the CDS. Fig. 4.11 shows the trend of pitch P = (Q1+Q4)-(Q2+Q3) and yaw Y = (Q1+Q2)-(Q3+Q4).

4.6. Test in vacuum

We decided to set the vacuum in two steps: this idea allows to have a faster temperature gradient, decreasing the waiting time for temperature (and benches) to stabilize.

So for the first step we set the pressure at 30 mbar, the day after we set the pressure at 5 $\times$ 10^{-3} mbar.
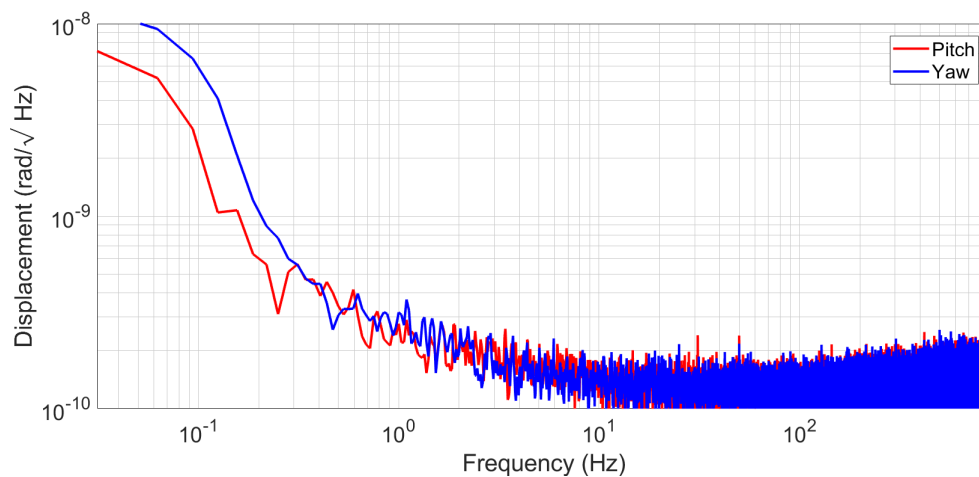
Figure 4.11.: Preliminary test in air: the traces show the trend of the pitch and as from the output of the pre-amp built at UoB.

Variables under examinations during the two steps of vacuum setting are: trend of temperature, pressure and position of the South bench along z axis.

Also, the alignment of the optical fibre has been checked during the process.

4.6.1. 30mbar test

Fig. 4.12 shows the measurements taken with the QPD. There are some peaks due to intensity fluctuations: we do not expect they disappear at lower pressure, because they are due to power fluctuation of the fibre itself.

Some peaks at lower frequencies may be due to bench motion: if the assumption is correct, at lower pressure and more stable temperature, these peaks should be less visible.

The movement of the South bench along z axis is used as a reference to monitor the bench adjustments with temperature variations. The variable under examination is displacement tested by a Linear Variable Displacement Transformer (LVDT).
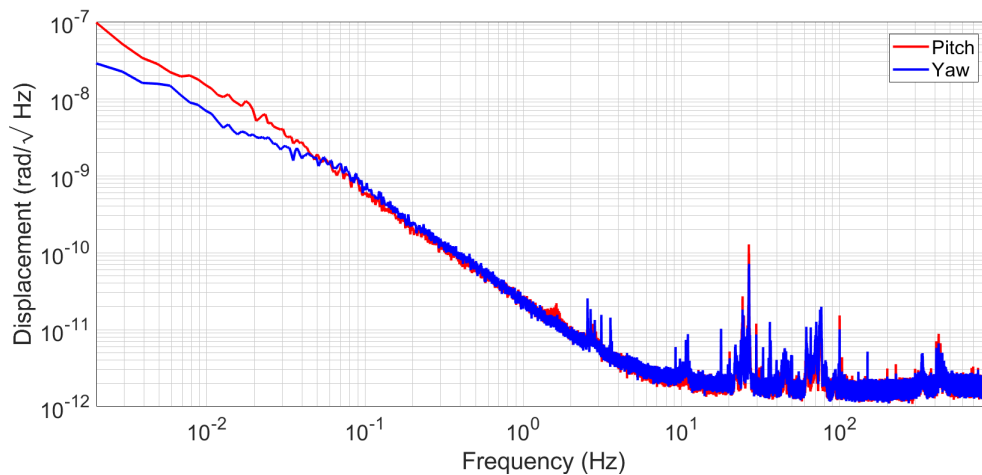
Figure 4.12.: QPD signals during 30 mbar pressure conditions. It is noticeable a difference of two orders of magnitude with respect to the in-air condition. This is due to the reduced impact of air flows and dust on the beam path.

4.6.2. Final vacuum set up

The pressure has been set at 5×10^{-3} mbar. What we expect is to find no variations in terms of the peaks we think are due to power fluctuations of the laser. Variations in LVDT trend can be due to temperature stabilization and related variations of pitch and yaw are then due to the more stable bench conditions (Fig. 4.13).

In this condition, also the signals from the L4C seismometers and accelerometers (Watt's Leakage) placed on the Central bench have been measured (Fig. 4.14). The plots with the UoB electronics show that there is some leakage below 10 Hz, probably due to saturation, in the measurement of the accelerometers.

QPD performance is shown in the plots 4.15. With AEI boxes we had expected results: no variations in the power fluctuation peaks and expected behaviour of pitch and yaw.
However, with UoB pre-amp the measurements do not seem consistent

with what we expected: we think that some non-linearities in UoB pre-amp could be the cause of the problem. This is still under investigation at UoB.
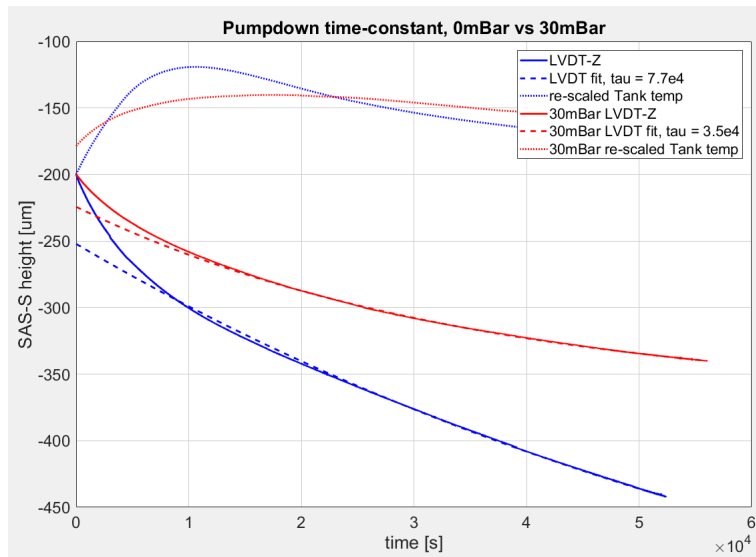
Figure 4.13.: Bench motion along z axis during the vacuum pump from 30 mbar to 5×10^{-3} mbar pressure conditions. Pressure has been set at 30 mbar at first stage to let temperature to stabilize faster. The two-step vacuum procedure was a good idea: it accelerated the lowering of temperature by two times.

4. Optical levers for tilt motion reduction
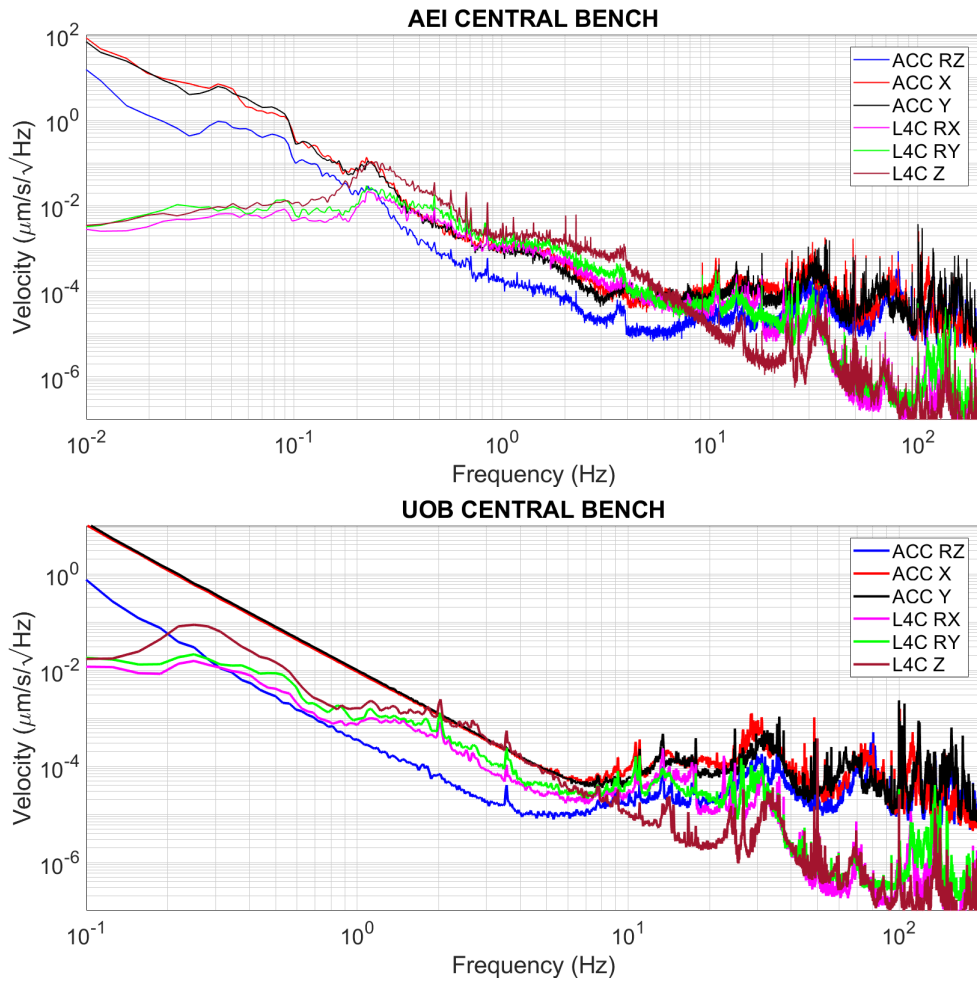
Figure 4.14.: Motion of Central bench measured by L4Cs and accelerometers, with AEI and UoB pre-amps. These plots highlights that the UoB electronics is not performing well (due to loop leakage) below 10 Hz.

Electronic noise Noise measurements of CDS with unplugged electronics have been taken, to check if there could be issues related to it. However, they do not show any unexpected behaviour: CDS dominates nearly everywhere and the CDS noise is lower than any of our optical measurements everywhere, typically by at least a factor of 10.
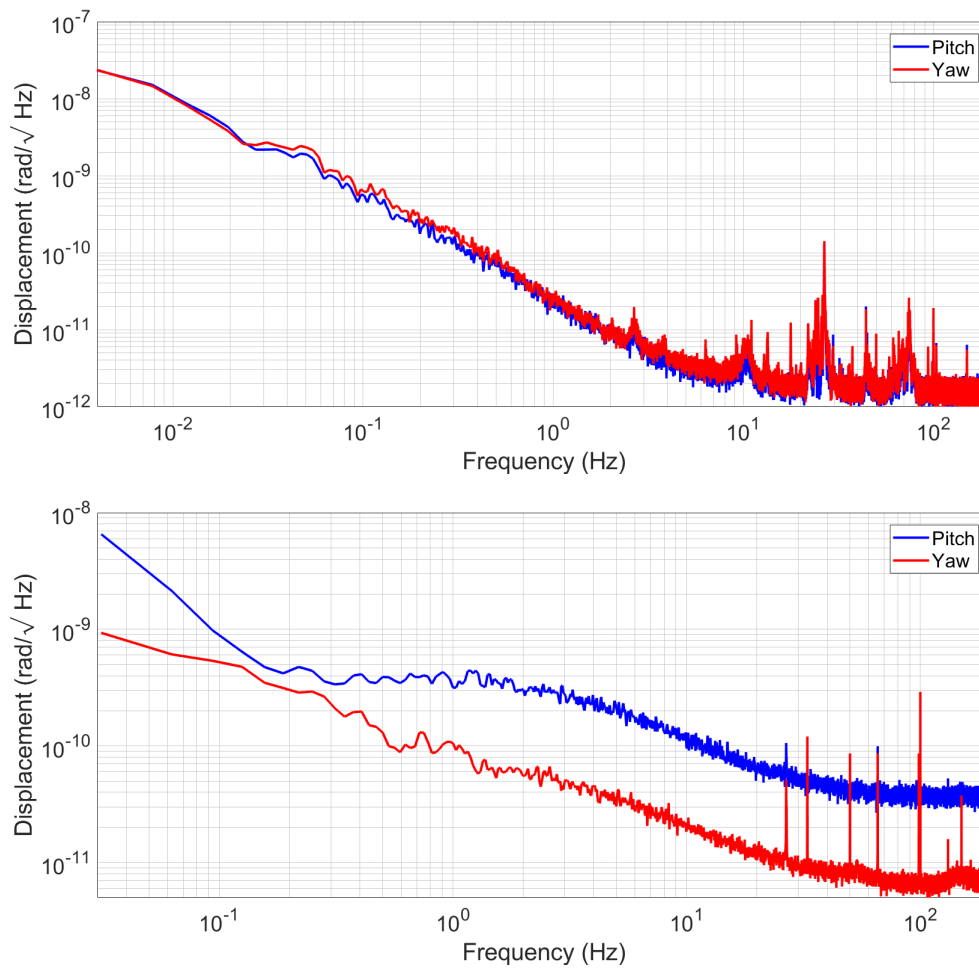
Figure 4.15.: QPD performance, with AEI and UoB pre-amps. There is an evident difference between the measurements taken with the two different electronics: pitch signal is 5x noisier than yaw with UoB electronics.

Conclusions

The analysis of feasibility of this experiment showed that the optical lever can be in principle a good device to sense tilt motion over long lever arms. However, the noise budget indicated a small frequency window of good operation, while below 0.1 Hz the levers are limited by the ground motion along the z axis. It is anyway a good device to be tested. During the test of the prototype, the measurements have shown that we had issues when calibrating the device due to problems highly related

4. Optical levers for tilt motion reduction
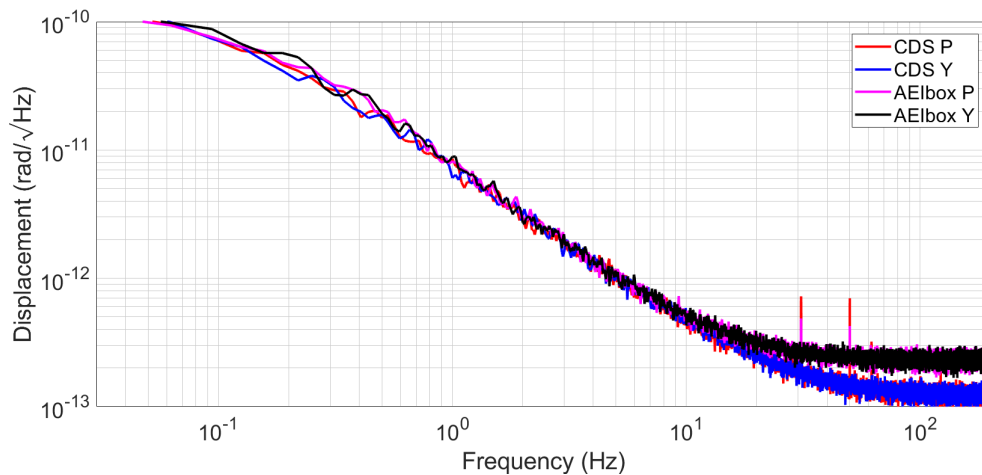
Figure 4.16.: Measurements of CDS noise and output of unplugged electronics.

to electronics from UoB, since the tests with the AEI electronics showed that the optical setup was well built and aligned. The very short time of the visit did not allow to take more in-depth tests.

Other possible reasons to investigate for better performance might lie in the structure of the prototype: further tests might be useful to understand if the device can be improved by changing the position of the lens with respect to the QPD, and let the diode sit at the focus on the lens. This solution will concentrate the power and decrease the size of the beam.

The device is currently not suitable for the purposes we tested for, but it opened the way to further tests to improve the technology: since the pitch and yaw tests have shown that the optical lever might be sensitive to the vertical motion of the bench, a reduction of this motion might be of great impact to improve the sensitivity of the levers [26]. With a good sensing system of tilt motion, the addition of an actuation system able to reduce this motion will be crucially helpful to stabilize the suspension points of the optical chains and then of the whole cavity.

5. Control of seismic platforms motion and LSC offloading

During 2019, I spent some months working at the LIGO Hanford site (Washington, USA). This experience allowed me to be critically involved in the complicated life of a gravitational-wave interferometer. In particular, I was given the opportunity to study how to improve LIGO performance at low-frequency, focussing on the reduction of seismic motion of the platforms where the optics are located.

In this chapter I will demonstrate how we can modify seismic control configuration of LIGO: in particular, this study should help reduce the differential motion between the chambers, making them move in sync, and help reduce and stabilize the rms motion of the auxiliary sensors, through an LSC offload. The final goal is to obtain different and possibly better performance for seismic motion stabilization, faster and longer locking mode and, ultimately, more gravitational waves detections. The detailed computations included in this chapter are original and partially presented to the LIGO community and stored in LIGO DCC [36] [37] .

This work has been developed in collaboration with LIGO Hanford and LIGO Livingston laboratories, Stanford University, MIT and UoB and completed at UoB during 2020.

This chapter is partially including some technical notes I shared with LIGO collaboration and the contents of this study have been presented at conferences and workshops [38].

Essential information about the sections of LIGO involved in this study

has been exposed in detail in Chapter 3.

5.1. Motivation: Duty cycle on LIGO

Lock loss events are the main sources of preventing continuous observations for long periods of time: when light loses resonance in the cavities, a lock loss happens and the control systems of the optical cavities are under effort to restore stabilization. This means that during lock loss the interferometer is no longer able to be stable and the observing time is interrupted [39].

Duty cycle is a major focus for commissioners before starting an observing run [39] [40]. It is needed not only to observe more gravitational waves, but also to identify noise sources and improve sensitivity [42].

Since the number of detected events over a time period N(t) is proportional to the volume of Universe under observation V, the observing time t and the rate R of astrophysical sources that can occur in a certain volume:

$$N(t) = R \cdot V \cdot t, \tag{5.1}$$

it can be seen that increasing the observing time towards a given direction, will increase the number of detected events.

Other ways to increase the number of detectable events is to increase the observable volume: this can be achieved by spending time on hardware to improve sensitivity on a given frequency bandwidth [40].

H1 operational state

[1256655618-1264550418, state: all]

- Observing [77.8%]
- Ready [0.9%]
- Locked [2.2%]
- Not locked [19.1%]

O3 Lockloss classification

Facilities 2.2%
CDS electronics 8%
CDS power 2.2%

Unknown 34.3%

SEI 38%

Human 15.3%

Figure 5.1.: **Up:** Example of duty cycle for Hanford Observatory, during O3b [40]. For almost 20% of the running time the detector was not locked, which means that it was not observing [1]. Of this 20%, the **bottom** chart shows the causes of the lockloss: the main ones are seismic and "unknown" The study presented here could possibly reduce both.

5.1.1. Differential motion between chambers

We have seen that among the noise sources which contribute to lock loss events there is the ground motion, including earthquakes and microseismic events.

In particular, during O3 run, it was observed that the chambers in the corner station (CS) show differential seismic motion with respect to each other [37], because they move independently from each other with respect to ground. It is reasonable to think that if the chambers could have a synchronized motion, the whole interferometer would move following the ground motion, without being affected by it. This would in principle help the cavities to be stable and to maintain the resonance.

In case of lock losses due to large earthquakes or high wind, stable resonance could be achieved in shorter times [43].

On another side, reducing the differential motion between the chambers means to reduce a source of noise at low frequency (5-30 Hz), as we will show in the next section: this would improve the sensitivity of the interferometer.

5.1.2. ISI stabilization

Differential motion affects the ISI of the HAM and BSC chambers in the CS: these are the platforms that we want to stabilize. Several sensors are responsible for sensing the seismic motion, in all degrees of freedom of each stage. We have already introduced the seismic sensors in Section 3.3 of Chapter 3: they are T240, L4C, GS13 and CPS [44].

In particular, CPS sensors are placed on every stage of every chamber: it is easy to compare the motion between HAM and BSC chambers through the signal of a device sensing the same motion on every chamber [46].

The idea which should stabilize ISIs to follow the ground motion is to lock the chambers to each other, in order to make them move on a synchronized way, following a common motion given by a driver chamber (or block of chambers).

Role of the mode cleaner We started our design on the chambers on the X arm. Along this direction, the Input Mode Cleaner (IMC) lies totally on HAM2 and HAM3 platforms: it can be used as a reference, or witness, of the motion between chambers, once they are locked together.

In the next section we will demonstrate that CPS are good witnesses to sense differential motion and that they also can be used to lock the chambers with each other.

---

[1]For a full understanding of the legend, refer to Appendix C.

5.2. Sensing differential motion via CPS

The Capacitive Position Sensors (CPS) measure the relative motion between two stages of the isolation system. On HAM chambers they are set between HEPI and ground, and between Stage 1 and HEPI. On BSC chambers they also measure the relative motion between Stage 1 and Stage 2. The plots in Fig. 5.2 show the differential motion seen by the CPS between BSC and HAM chambers: the sensors put in evidence that the HAM chambers have a more synchronized motion with respect to the motion between HAM and BSC and BSCs only. This means that the block of HAM chambers on X arm is more stable relatively to the other blocks and can be used as driver for the other chambers, with the mode cleaner acting as witness. We then projected the CPS of the X axis chambers to the suspension point in order to obtain PRCL and Input Model Cleaner Length (IMCL) traces like as they would be sensed by the CPS. For BSCs, we decided to sum the contributions of the CPSs on stage 1 and stage 2 and to project this sum to the suspension point. One of the main differences between the behaviour of CPS IMCL and CPS PRCL is that the former is involving only the HAM chambers. Since HAM2 and HAM3 have a very good common motion, IMCL can be considered more stable with respect to PRCL, which instead involves also BSCs. Indeed, CPS PRCL is following only the BSCs, at frequencies below 0.03 Hz 5.3.

Fig. 5.3 shows the plots of PRCL and ICML as sensed by CPS projection to the suspension point. These projections indicate that reducing the differential motion as seen by the CPSs will help to reduce the residual motion seen by the optical cavities. We expect this to be effective in a range of frequencies between 0.1 and 0.5 Hz.

5. Control of seismic platforms motion and LSC offloading
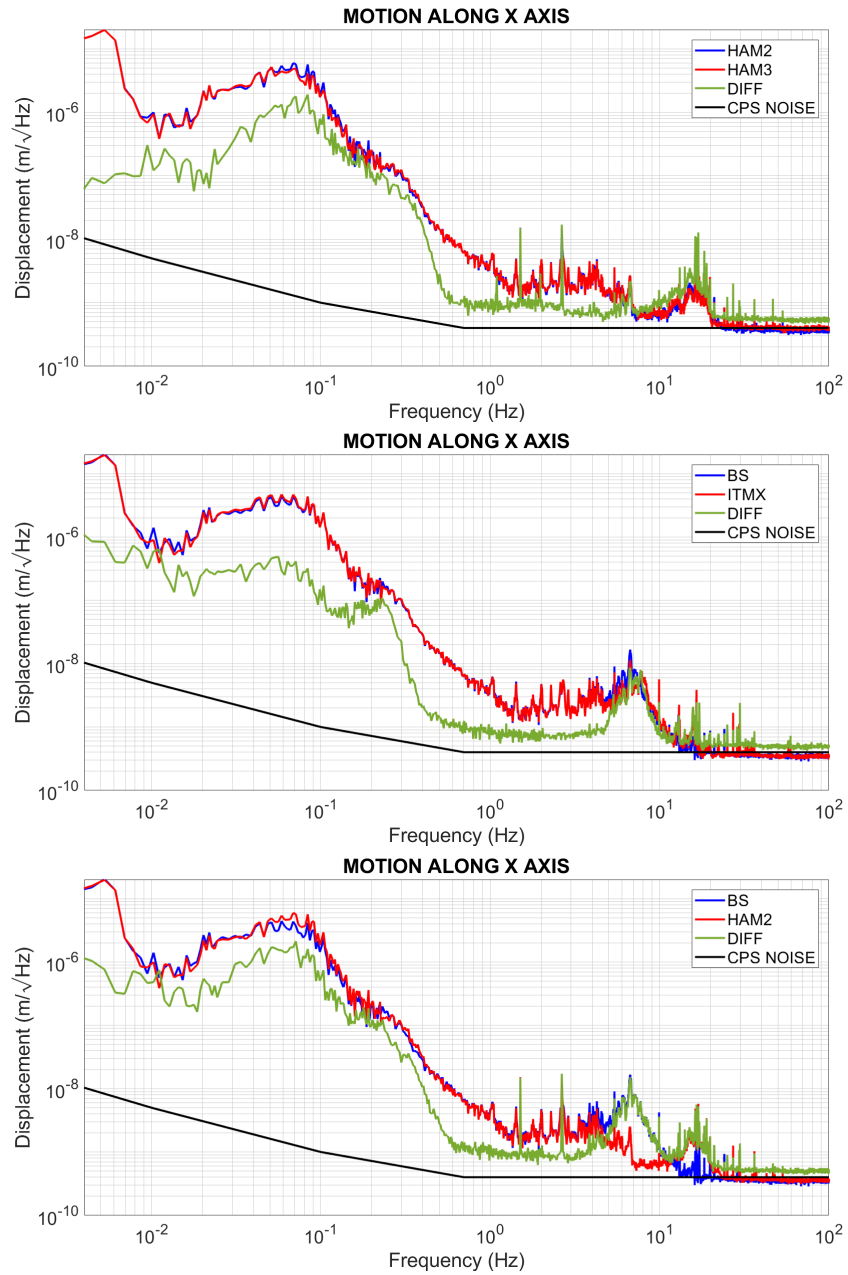
Figure 5.2.: CPS differential motion between the HAM and BSC chambers along X axis. ISIs move in common, particularly in the same building. This can be confirmed by noting that the difference between two chambers is much lower than individual chambers.

Figure 5.3.: CPS suspension point (suspoint) projections: IMCL and PRCL. These plots show that the CPS sensors are good to monitor the motion of the optics at suspension points. In particular, the PRCL sensed by the CPS matches the calibrated PRCL trace between 0.6 and 0.2 Hz. Below this value we were expecting the traces to match: the un-match is due to PRCL calibration issues under solving. The IMCL is currently monitored by the GS13, and the plot shows that even CPS can be a good sensor for it. Hence we can use these sensors to monitor the motion of the optics, additionally to the relative motions between the platforms.

5.3. Locking chambers via CPS

In the previous section we demonstrated that the CPSs are good sensors for differential motion and that they can be used to monitor the

chamber motion at lower frequencies. That said, and remembering the aim of stabilizing the motion of the chambers making them moving in sync, it is possible to use the CPSs to lock HAM2 and HAM3 together, HAM4 and HAM5 together, BSCs in the Corner Station together and BSCs hosting the ETMs together (refer to Chapter 3 for the location of these chambers). This will stabilize the ISI differential motion with respect to a driving chamber.

Since we saw that HAM2 and HAM3 show a very good common motion and that we can use the IMC as a witness of it, our first step is to lock the HAM2 and HAM3 chambers together by feeding HAM3 a calculated differential CPS signal. This is performed with an additive offset to the setpoint of the HAM3 isolation control loop [47].

The block diagram in Fig. 5.4, shows the structure of HAM2, where the signals from d_2 and i_2 represent the offsets given by CPS and inertial sensors [2].

At low frequency the CPS noise is negligible because its contribution is about 10^3 times lower than the microseismic peak.

General block diagrams notations used in the hereafter are listed in Tab. 5.1

We can compute the signal d_2 which will be the CPS offset to send to HAM3 chamber. In this case, HAM2 will drive HAM3 to follow its motion. Defining K = PC:

$$
\begin{aligned}
d_2 &= x_{p_2} - x_g \\
&= K[L_2(SN_g + Sx_g + d_2) + H_2N_{1_2} + H_2(x_g + d_2)] + Px_g - x_g \\
&= KL_2S(N_g + x_g) + KL_2d_2 + KH_2N_{i_2} + KH_2x_g + KH_2d_2 + Px_g - x_g.
\end{aligned}
\tag{5.2}
$$

---

[2]For a summary on control loops, general design and feature and how to solve a block diagram, refer to Appendix B.

P	Plant
S	Sensor correction
C	Control
L	Low pass filter
H	High pass filter
N_g	ground noise
N_i	inertial noise
x_g	ground motion
x_p	plant motion

Table 5.1.: Notations used in the block diagrams.
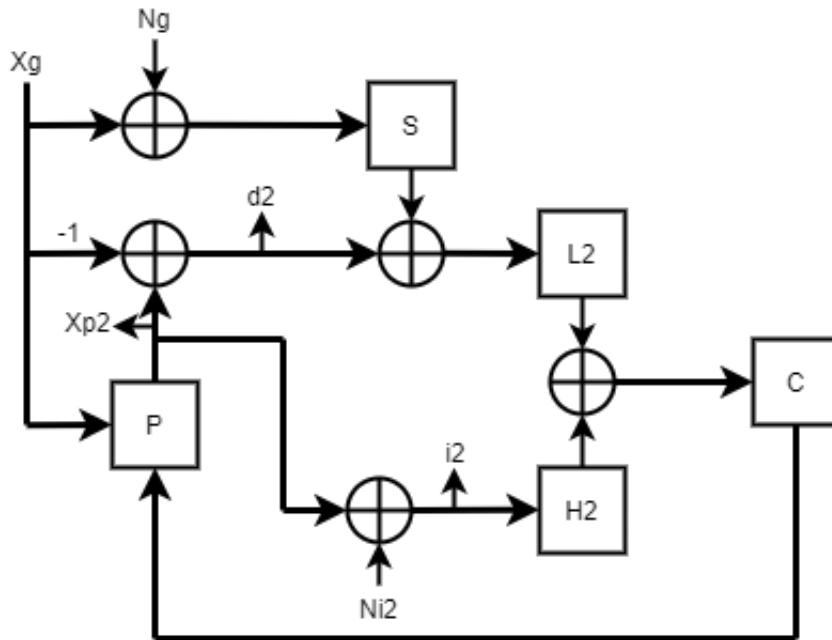
Figure 5.4.: Simplified block diagram for HAM2 chamber as it is at present on LIGO [47].

Since L_2 + H_2 = 1, we get:

$$d_2(1 - K) = KL_2S(N_g + x_g) + KH_2N_{i_2} + KH_2x_g + Px_g - x_g,$$

which will lead to:

5. Control of seismic platforms motion and LSC offloading

$$d_2 = \frac{K}{1-K}[L_2 S(N_g + x_g) + H_2 N_{i_2} + H_2 x_g] + P\frac{x_g}{1-K} - \frac{x_g}{1-K}. \qquad (5.3)$$

The platform motion of HAM2 can be computed following the block diagram in a similar way:

$$x_{p_2} = K\{L_2[S(N_g + x_g) + x_{p_2} - x_g] + H_2 N_{i_2} + H_2 x_{p_2}\} + Px_g. \qquad (5.4)$$

After some manipulations, and remembering that $L_2 + H_2 = 1$, we obtain:

$$x_{p_2} = \frac{K}{1-K}[L_2 S(N_g + x_g) - L_2 x_g + H_2 N_{i_2}] + P\frac{x_g}{1-K}. \qquad (5.5)$$

The result in Eq. 5.5 is the signal to subtract to HAM3 in order to feed HAM3 a CPS differential motion that is added to HAM3 as shown in the block diagram in Fig. 5.5. In the original configuration, without any feeding into HAM3, the block diagrams for both chambers would be identical. With the provided feeding, instead, there is no sensor correction and ground noise on HAM3 because they both come from the contribution from HAM2, which is the offset d_2 added to HAM3.

We then want to know the reaction on HAM3 plant in this configuration, in order to compute the differential motion between plants on both chambers.

Following the usual notations and the block diagram of HAM3:

$$x_{p_3} = K[L_3 d_2 + L_3 x_{p3} - L_3 x_g + H_3 N_{i_3} + H_3 x_{p_3}] + Px_g,$$

$$x_{p_3} = \frac{K}{1-K}[L_3(d_2 - x_g) + H_3 N_{i_3}] + P\frac{x_g}{1-K}. \qquad (5.6)$$

The differential motion will be:
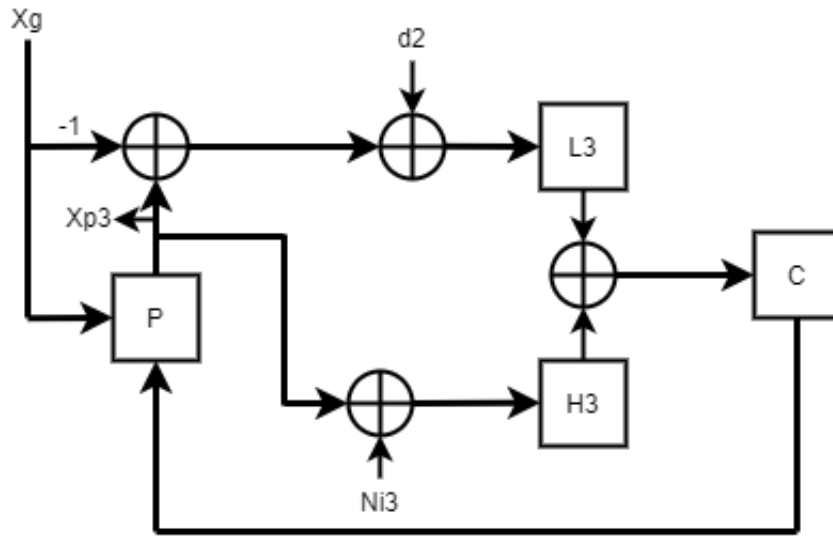
Figure 5.5.: Simplified block diagram for HAM3 in the new configuration where this chamber is now connected to HAM2: d_2 is the offset coming from HAM2 [47].

$$x_{p3} - x_{p2} = \frac{K}{1-K}[L_3(d_2 - x_g) + H_3 N_{i_3}] + P\frac{x_g}{1-K}$$
$$- \frac{K}{1-K}[L_2 S(N_g + x_g) - L_2 x_g + H_2 N_{i_2}] - P\frac{x_g}{1-K}. \tag{5.7}$$

In the approximation where K$\to \infty$, i.e. in a condition of infinite gain, the terms we computed become:

$$x_{p2} = H_2 N_{i_2} + L_2 S(N_g + x_g) - L_2 x_g, \tag{5.8}$$

$$d_2 = H_2 N_{i_2} + L_2 S(N_g + x_g) + H_2 x_g, \tag{5.9}$$

$$x_{p3} = H_3 N_{i_3} + L_3(d_2 - x_g). \tag{5.10}$$

$$x_{p3} - x_{p2} = L_3 d_2 - L_3 x_g + H_3 N_{i_3} - L_2 S(N_g + x_g) + L_2 x_g - H_2 N_{i_2}$$
$$= L_3 L_2 S(N_g + x_g) + L_3 H_2 N_{i_2} + L_3 H_2 x_g - \tag{5.11}$$
$$L_3 x_g + H_3 N_{i_3} - L_2 S(N_g + x_g) + L_2 x_g - H_2 N_{i_2}.$$

If both chambers are mainly driven by the low pass filters (H $\rightarrow$ 0), the differential motion becomes:

$$x_{p_3} - x_{p_2} = L_3 d_2 - L_3 x_g - L_2 S(N_g + x_g) + L_2 x_g$$
$$= L_3 \cdot L_2 S(N_g + x_g) - L_3 x_g - L_2 S(N_g + x_g) + L_2 x_g,$$

$$x_{p_3} - x_{p_2} = L_2 S(N_g + x_g)(L_3 - 1) + x_g(L_2 - L_3), \tag{5.12}$$

which is what we expect to be the signal of the differential motion sensed by the CPSs. In order to see this signal, we need to implement the modifications of the filters involved in the loop, as shown in the following section.

5.4. Analysis of feasibility

The next step is to study how to modify the low and high pass filters in order to obtain the best performance from each one in the new configuration of the chambers [48]. To do this, we are going to change the blending filters, i.e. those filters whose combination gives the best performance of the set low+high pass filters.

If by definition we have L+H=1[3], we can write it as:

$$L_{lh} + H_{lh} = \frac{(\alpha + b)^{l+h-1}}{(\alpha + b)^{l+h-1}}. \tag{5.13}$$

According to the values of l and h, we have different orders of magnitude of the binomials, which can be solved for the real part.

In our case, we have two main contributions given by inertial sensors and the CPS. We will apply the high-pass filter to the inertial sensors and the low-pass one to the CPS.

---

[3]This definition arises from the need to account for unconditional loop stability and noise contributions. For details about blending filters, refer to [44].

To do this, we need the specific contributions for each chamber to be specified, with all the components well defined. For example, in the case of the CPS contribution, we need to define the tilt component, the CPS noise and the ground motion, which will take part into the platform motion as seen by the CPS sensor. This is because these components are independent from each other and will need to be summed in quadrature.

Besides, as we saw in the previous computations, we will need to apply filters: the Sensor Correction filter will be the one used on LIGO and shown in Fig. 5.6; the high- and low- pass filters will be evaluated through blending several possible filters across a certain number of l and h order of magnitudes, as introduced before. The best blended filter will be given by a combination of two l and h values at a specific blending frequency.

At the end of the analysis for each chamber (HAM and BSC) in isolation, we will connect the chambers via CPS and look at the results.

All this analysis has been performed through Matlab software.
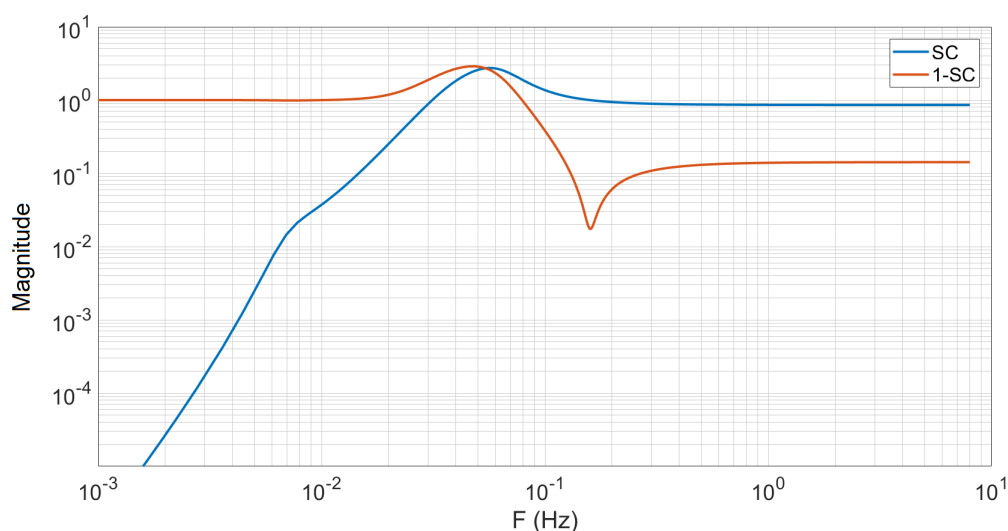
Figure 5.6.: The sensor correction filter as it is at present installed on LIGO. This filter is one of the contributors to take into account for when computing the blending filters.

5.4.1. Contributions from CPS and inertial sensors

To calculate the CPS signal contribution, we need the ground motion and we used the ITMY STS (Streckheisen Tri-axial Seismometer) signal on X direction. This is going to be the same motion for every chamber, since there is only one sensor in the Corner Station to measure it, because it has been found that the ground motion is the same everywhere in the Corner Station. This signal includes a contribution from the tilt motion, dominating in the STS spectrum in the microseismic frequency (< 0.15 Hz); we call it $\theta_g = \theta \cdot g/\omega^2$ and we separate it from the ground motion x_g:

$$x_g = STS - \theta_g. \tag{5.14}$$

The CPS signal has been then computed summing in quadrature the contributions given by tilt, ground motion and CPS noise (N_{cps}), and applying the sensor correction filter:

$$CPS_{inj} = \sqrt{(\theta_g \cdot SC)^2 + (x_g \cdot (1 - SC))^2 + (N_{cps})^2}. \tag{5.15}$$

Figure 5.7 shows the CPS signal and all its contributions. Since θ_g effects one STS, this injected signal is the same at all CPS sensors.

To calculate the platform motion of the BSC, we used data from the ITMX ISI along X direction. This is the signal from the T240 sensor. We applied the same technique and we separate the tilt contribution ($BSC\theta_p$) from the signal, and to obtain the inertial sensor contribution for the BSC chambers we sum in quadrature the contributions from tilt and T240 noise:

$$T240_{inj} = \sqrt{BSC\theta_p{}^2 + N_{T240}{}^2}. \tag{5.16}$$

Figure 5.8 shows the T240 signal and its contributors.
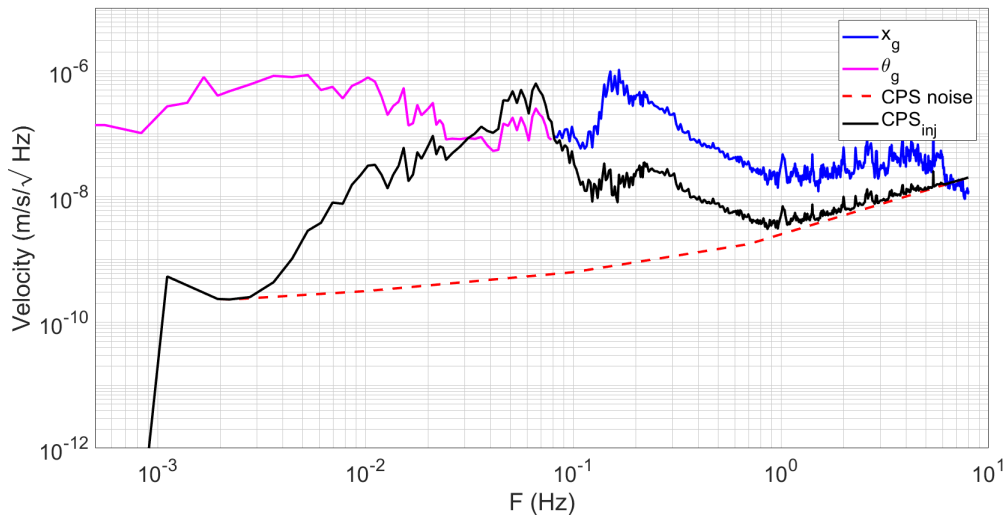
Figure 5.7.: Plot of all the single CPS contributions calculated. This compu-
tation is valid for all chambers, since CPSs are installed on all
chambers and are subjected to the same working principle.
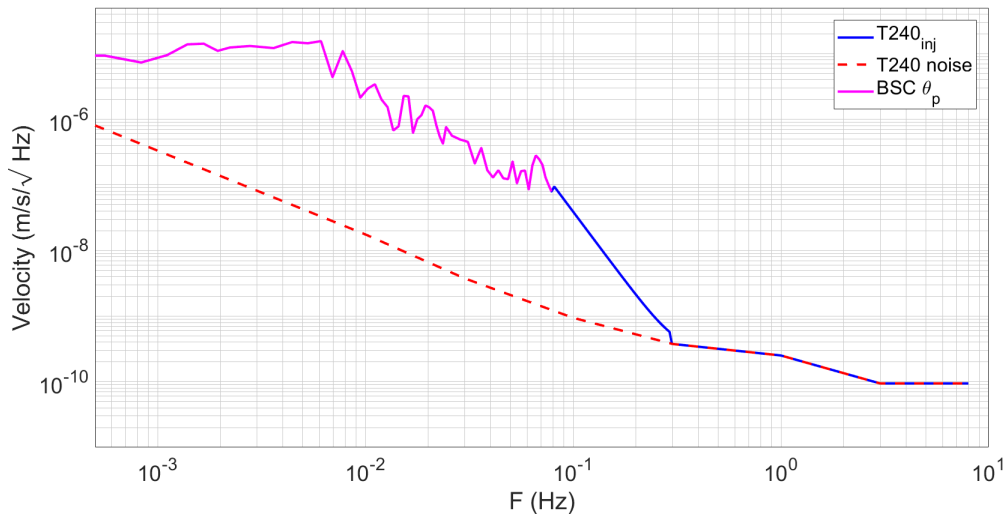
Figure 5.8.: Plot of all the single BSC contributions computed from the iner-
tial sensor involved in this chamber. We assume that the T240
is dominated by tilt effects below 80 mHz, and by sensor-noise at
higher frequencies: the θ_p contribution is the $T240_{inj}$ signal below
80 mHz. We interpolated these two bands together to determine
an effective input disturbance as witnessed by the T240.

5. Control of seismic platforms motion and LSC offloading

The inertial contribution for HAM chambers is computed in a similar way: the sensor in this case is the GS13 and we used data from the ISI of HAM2 in x direction. Calling variables in the usual way:

$$GS13_{inj} = \sqrt{HAM\theta_p{}^2 + N_{GS13}{}^2}. \tag{5.17}$$

Figure 5.9 shows the GS13 signal and its contributors.
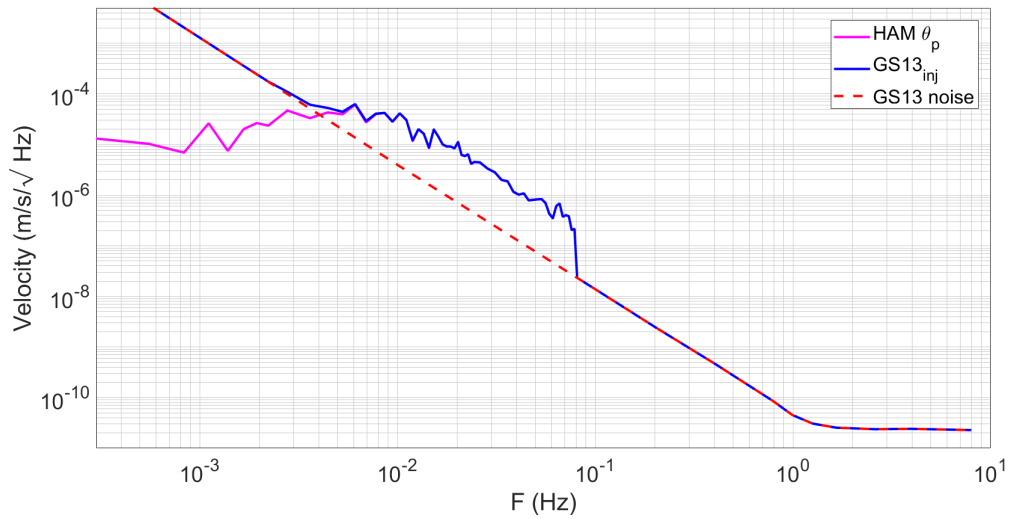
Figure 5.9.: Plot of all the single HAM contributions calculated for the inertial sensor involved in this chamber. Similarly to the previous case, the θ_p contribution is the $GS13_{inj}$ signal below 80 mHz.

5.4.2. Blending filters

In order to compute the platform motion for the single chambers in isolation and, later, locked together via CPS, we need the low- and high-pass filters. Many possible blended filters have been found for different combinations of order of magnitudes and blending frequency: the plots in Fig. 5.10 show the velocity rms for every combination.

The best combination has been found computing the orders and the blending frequency which give the minimum of the cost. The optimized blending filter has been then built using the best values of l and h orders

and blending frequency. The cost is given by:

$$cost = \sqrt{\int ((cps_{inj} \cdot LP)^2 + (T240_{inj} \cdot HP)^2)df} \qquad (5.18)$$

with a similar equation for the HAM chamber.

Fig. 5.11 shows the cost and its rms obtained with the best blending filters for BSC and HAM chambers.

5.4.3. Locking the chambers

With these elements, we can proceed with the analysis of the behaviour of the chambers when locked via CPS. We refer to HAM2 and HAM3 chambers, since in the previous sections we made the computations for them. We recall here that the equations we need are 5.8, 5.9, 5.10 and 5.12, where x_{p_2} is HAM2 platform motion, d_2 is the signal from HAM2 to send to HAM3 and x_{p_3} is HAM3 motion when attached to HAM2 via CPS.

What we need to know is which terms of these equations are coherent, in order to separate them from the incoherent ones, which will need to be summed in quadrature. We assume that the ground translation at low-frequencies is the same everywhere in the CS, and we already estimate the tilt separately, so the terms involving x_g can be considered coherent. Noises are instead independent from each other. The previous equations then become:

$$x_{p_2} = \sqrt{(H_2 N_{i_2})^2 + (\theta_g \cdot SC \cdot L_2)^2} + (x_g \cdot SC \cdot L_2) - (x_g \cdot L_2), \qquad (5.19)$$

$$d_2 = \sqrt{(N_{i_2} H_2)^2 + (\theta_g \cdot SC \cdot L_2)^2} + (x_g \cdot SC \cdot L_2) + (x_g \cdot H_2), \qquad (5.20)$$

$$x_{p_3} = \sqrt{(N_{i_2} H_2)^2 + [L_3 \sqrt{(N_{i_2} H_2)^2 + (\theta_g \cdot SC \cdot L_2)^2}]^2}$$
$$+ (x_g \cdot SC \cdot L_2 + x_g \cdot H_2) \cdot L_3 - (x_g \cdot L_3). \qquad (5.21)$$
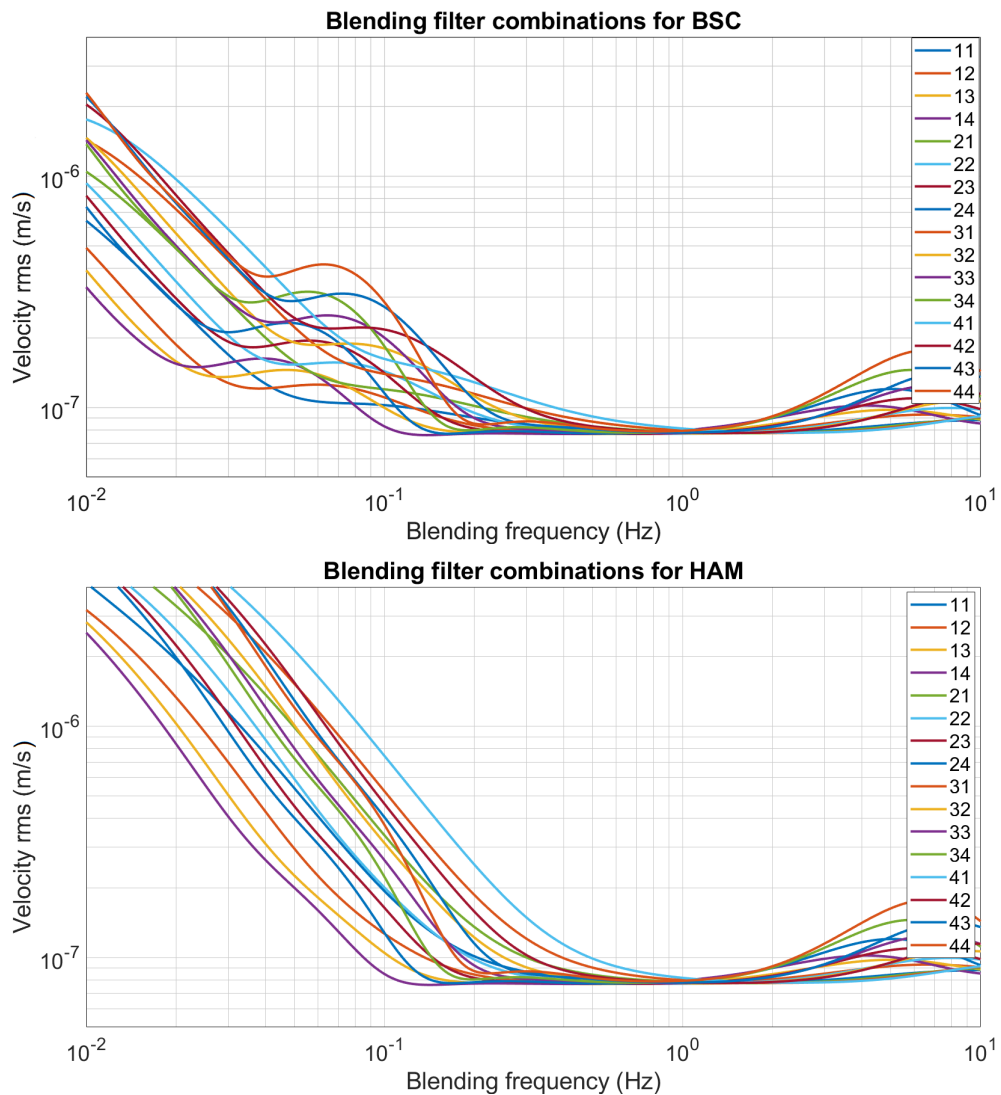
Figure 5.10.: Plots of all possible costs built with different combinations of blending filters. The orders of magnitude are indicated by the low and high pass indices l and h of the binomial filter in 5.13 and the are going between l =[1,4] and h = [1,4]. The plateau on both plots is given by the fact that the SC filter is dominating over those frequencies: this means that the chosen cost function has too little power to discriminate between blends. This makes a new way to evaluate blending filters in presence of the SC filter necessary, in particular re-weighting the blends as functions of frequency may help the optimisation process.
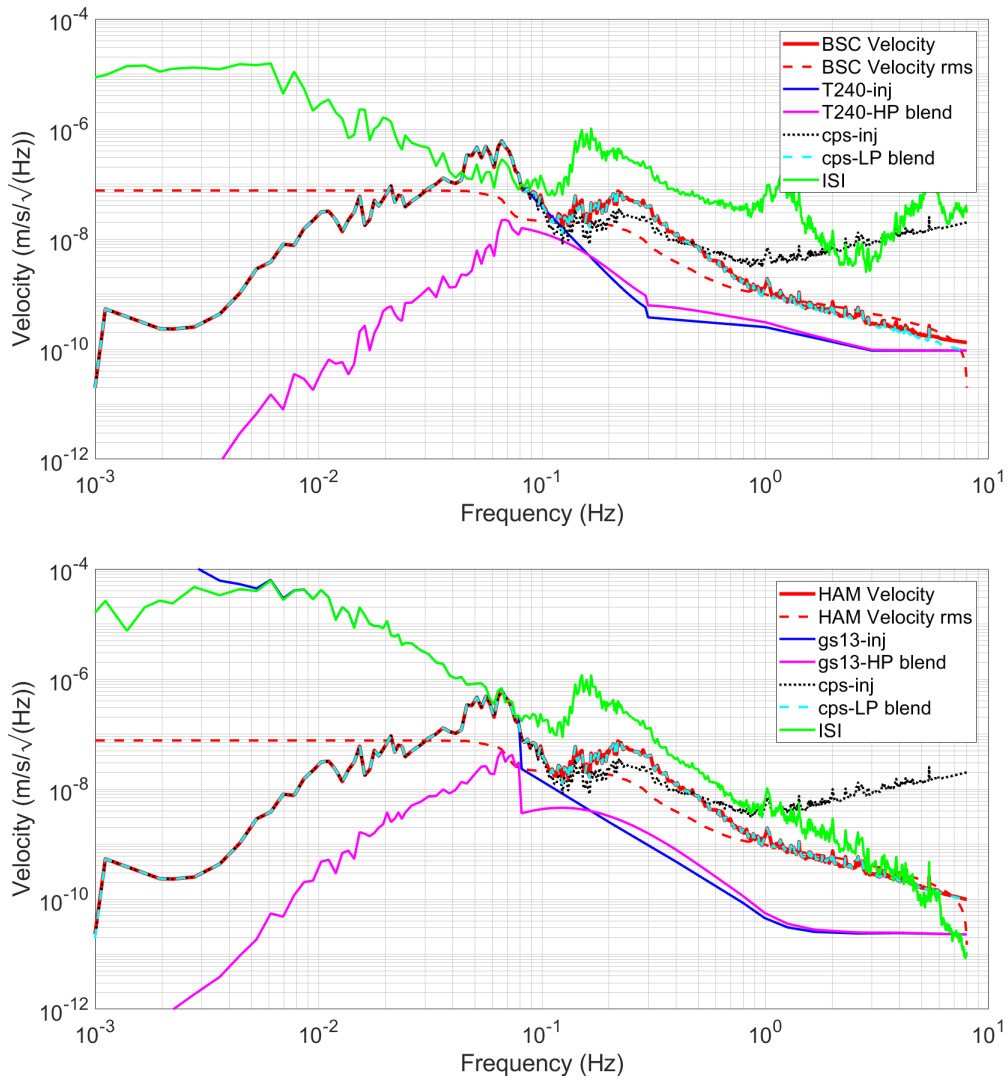
Figure 5.11.: HAM and BSC cost and their contributions from. For BSC, the best blending filter is given by l = 1, h = 4 at a blending frequency of fb = 0.13 Hz. For Ham, the best indeces are l = 1, h = 4 and fb = 1.14 Hz. Te green trace is the row, uncontrolled motion of the ISI, for reference.

Since $L_3 = L_2$ and $H_2 = H_3$:

$$x_{p3} - x_{p2} = |\sqrt{(L_2 \cdot SC \cdot \theta_g \cdot L_2)^2 - (L_2 \cdot SC \cdot \theta_g)^2} + (x_g \cdot SC \cdot L_2{}^2) - (x_g \cdot SC \cdot L_2)|. \tag{5.22}$$

The plot in Fig. 5.12 shows the differential motion of HAM2 and HAM3

in isolation and the motions when the chambers are locked to each other. The improvement of the differential motion is evident below 0.1 Hz, but it is not efficient above this frequency: further studies of the blending filters involved and a re-weight of the cost in a different part of the spectrum could help to find a compromise.
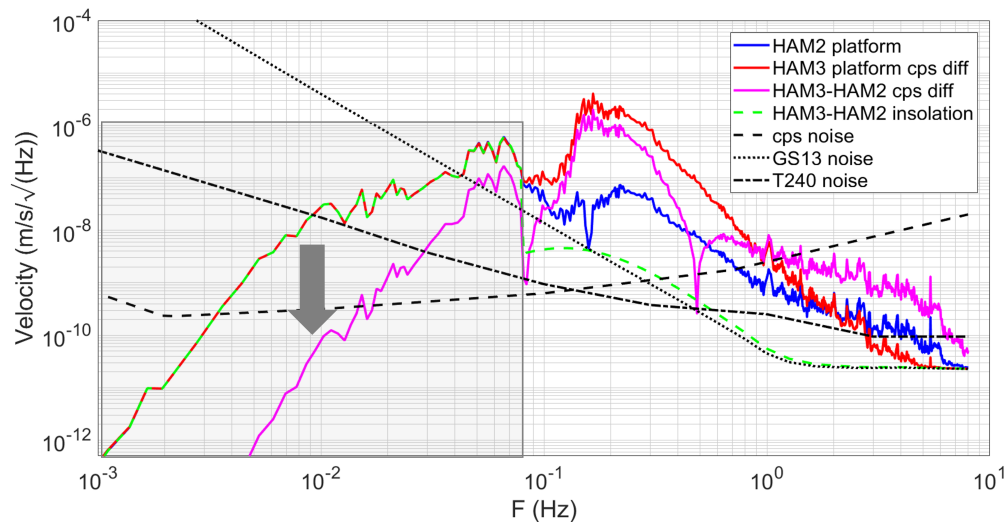
Figure 5.12.: HAM chambers in CPS locking condition: the plot shows the motion of each chamber, where HAM3 depends on HAM2, through CPS locking, and the differential motion between them. There is an improvement of the differential motion in the new configuration (purple trace) with respect to the situation in isolation (green dashed trace) by a factor of 3 in order of magnitude below 0.1 Hz.

5.5. Inertial sensors locking

In the frame of ISI stabilization from ground motion, the inertial sensors could also be used for the same purpose to lock chambers, in addition to CPS locking [48]. This means that HAM3 will be fed by the inertial sensors signal coming from HAM2.

Signals from inertial sensors are represented by i_2 and i_3 notations in Fig. 5.4 and 5.5. However, adding the signal i_2 to HAM3 implies that the block diagram will be modified as in Fig. 5.13.
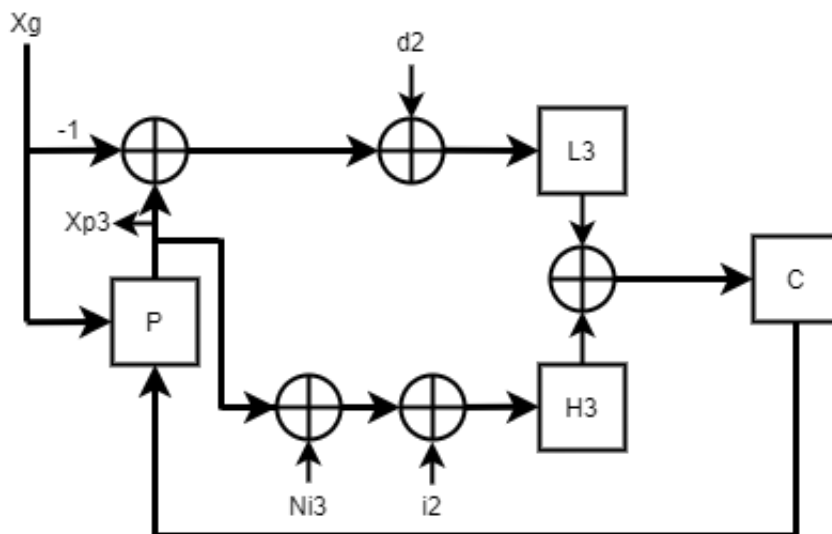
Figure 5.13.: New setup of HAM3 chamber fed by CPS and inertial sensor signals from HAM2.

Following a similar path for the math for this configuration of i_2 signal from HAM2:

$$i_2 = x_{p_2} + N_{i_2} = \frac{K}{1-K}[L_2 S(N_g + x_g) - L_2(N_{i_2} + x_g)] + \frac{Px_g}{1-K} + \frac{N_{i_2}}{1-K}. \quad (5.23)$$

This is the signal from HAM2 inertial sensors to inject into HAM3 as shown in Fig. 5.13. Then, the platform motion of HAM3 becomes:

$$x_{p_3} = K[L_2 d_2 + L_3 x_{p_3} - L_3 x_g + H_3 i_2 + H_3 N_{i_3} + H_3 x_{p_3}] + Px_g,$$

$$x_{p_3} = \frac{K}{1-K}[L_3(d_2 - x_g) + H_3(i_2 + N_{i_3})] + \frac{Px_g}{1-K}. \quad (5.24)$$

In the approximation where K → ∞:

$$i_2 = L_2 S(N_g + x_g) - L_2(n_{i_2} + x_g), \quad (5.25)$$

$$x_{p_3} = L_3(d_2 - x_g) + H_3(i_2 + N_{i_3}). \quad (5.26)$$

Remembering Eqs. 5.8 and 5.9 for x_{p_2} and d_2, we can compute the differential motion:

$$x_{p_3} - x_{p_2} = L_3 d_2 - L_3 x_g + H_3 i_2 + H_3 N_{i_3} - H_2 N_{i_2} - L_2 S(N_g + x_g) + L_2 x_g$$

$$= L_3 L_2 S(N_g + x_g) + L_3 H_2 N_{i_2} + L_3 H_2 x_g - L_3 x_g + H_3 L_2 S(N_g + x_g) -$$

$$H_3 L_2 (N_{i_2} + x_g) + H_3 N_{i_3} - L_2 S(N_g + x_g) + L_2 x_g - H_2 N_{i_2},$$

$$x_{p_3} - x_{p_2} = x_g(L_3 H_2 - H_3 L_2 + L_2 - L_3) + N_{i_2}(L_3 H_2 - H_3 L_2 - H_2) + N_{i_3} H_3. \quad \text{(5.27)}$$

The computation of the differential motion between HAM2 and HAM3 in the conditions where the two ISIs are connected both via CPS and inertial sensors shows that there is no contribution from the sensor correction and from the ground noise.

Besides, it is worth notice that if $L_2 = L_3$, also $H_2 = H_3$ by definition and then the differential motion is:

$$x_{p_3} - x_{p_2} = N_{i_3} H_3 - N_{i_2} H_2$$
$$= H(N_{i_3} - N_{i_2}), \quad \text{(5.28)}$$

which is exactly the solution that we would obtain if the differential motion was computed without any feeding: this means that in this configuration the differential motion would be the same as in isolation condition.

5.6. Test on LIGO Hanford and LSC signals optimization

During the 2019 commissioning break, in collaboration with LIGO Livingston Observatory, we tried to apply the new CPS configuration in

order to obtain improvements in ISI motion and LSC signals at LIGO Hanford.

This test has been performed before the detailed analysis exposed previously and hence a more detailed and precise study for the choice of the blending filters involved is essential to get the expected enhancements. However the preliminary tests at LHO showed an improvement of a factor of 3 at 60 mHz (Fig. 5.14), as detected by the IMC sensors, and an encouraging result detected by the DARM signal below 0.1 Hz when all the chambers inside and outside the CS were locked (Fig. 5.15). This is an interesting result that shows that with the implementation of the correct filters as shown in the analysis it is possible to reduce the differential motion of the platforms. Some effects of this configuration have been testified even by IMCL, during a measurement in on/off offloading, reported in the LHO logbook post 52690. Other tests looking at the effect on the LSC cavities are reported in post 52729 of the LHO logbook.

With this in mind, a positive consequence of this effect might be the improvement of the LSC signals from LIGO cavities. Among them, DARM is particularly important, because it represents the gravitational wave signal. It might be convenient to make the optics of the LSC cavities, lying on the platforms and subjected to the ISI motion, be controlled by the ISI itself. This ideas has been developed and tested at LHO and is exposed in the following section.

5.6.1. LSC offloading

We saw that the cavities and the optical signals in LIGO are affected by the ISI motion, simply because they lie on them. Given the work done with the CPSs to suppress the ISI motion, we should see an improvement on LSC signals. This is not immediate, though, nor trivial, because the optics are just set on the optical bench, without any com-

5. Control of seismic platforms motion and LSC offloading
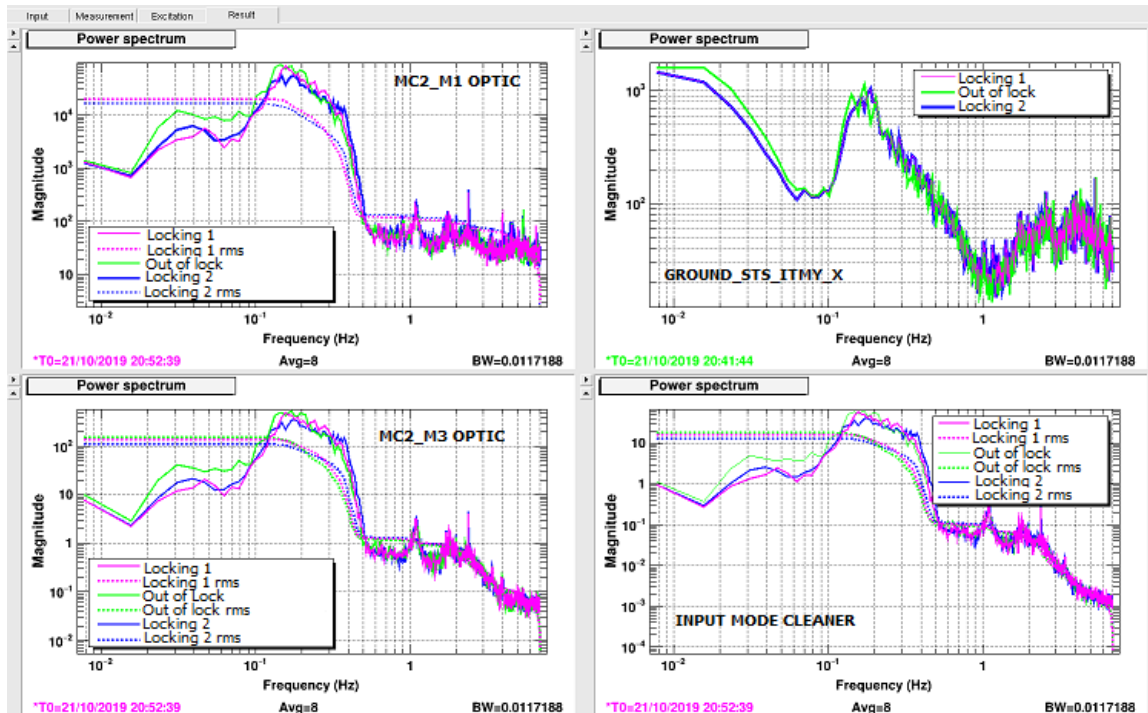
Figure 5.14.: Screenshot from LHO CDS showing a quick measurement with the chambers in the CS were locked: the witness is the IMC and we monitored also the ground motion to make sure that no important variations were happening at the moment of the measurement. The green traces represents the motion before the locking, while we took two measurement after the locking (blue and pink) to validate the test. **Left:** motion of the suspension point of the M2 and M3 optics (lying on HAM3 and HAM2 respectively). **Right:** ground motion and IMC cavity motion before (green) and after the locking mode (blue and pink).

munication with the ISI, and there is no active control between the ISI and these optics. Despite there is a sort of benefit as testified by Fig. 5.15, the motion of the optics on the chambers due to other factors than seismic noise is not seen by the platforms: if we could connect this motion to the platform via software, this would make the optics and the platform more dependent on each other. This means that we can control the stabilization of the cavity lengths also with the ISIs.

What we expect is a faster reach of locking and a longer state of lock of
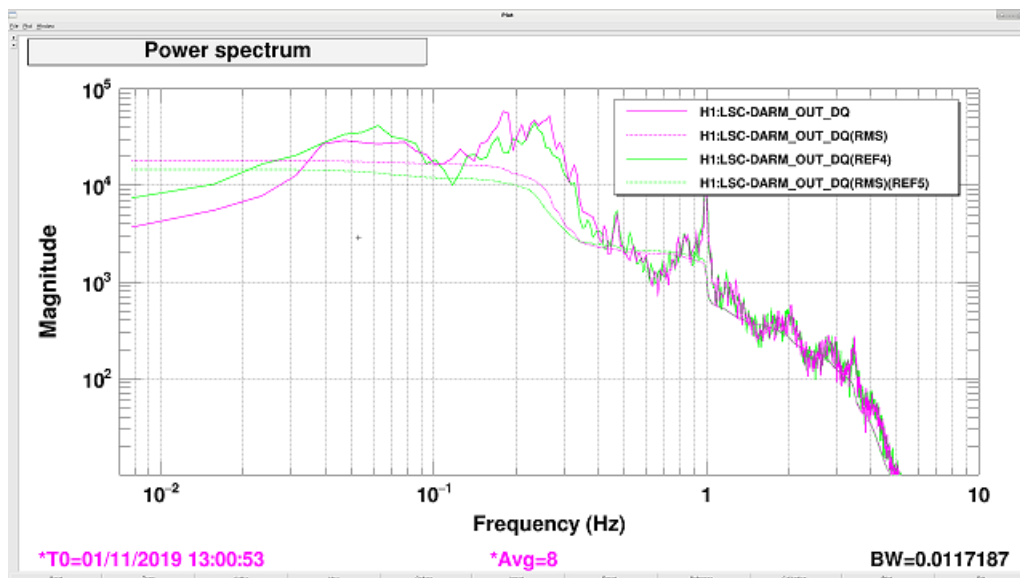
Figure 5.15.: Screenshot taken from LHO CDS when a quick measurement of DARM reaction to the lock of all the chambers has been taken. The result is encouraging because it shows an improvement of the signal below 0.1 Hz.

the interferometer during observing runs. Another advantage would lie in a reduction of the forces already used to stabilize the cavities and in less tilt motion.

This work has been performed on LIGO Hanford in October and November 2019, during the commissioning break between O3a and O3b observing runs. The reason of this choice is that we needed the interferometer to *not* be observing, since we were going to modify some software structure of the instrument.

To lock the LSC signals to ISIs, we need to do something similar to what we did with the HAM chambers: we need to connect via software two different setups which do not talk to each other. We decided to start from the Power Recycling Cavity Length (PRCL) because we locked HAM2 and HAM3 chambers, so it was natural to start to lock the cavities on the x axis.

Through CPSs locking, we reduced the differential motion of HAM2 and HAM3 chambers and made them move in sync. So they can be consid-

ered as a whole block. The IMC is entirely lying on HAM2 and HAM3, and it is straightforward to use it as a witness: to make this real, we need to feed the HAM2-HAM3 block to IMCL. This will lock the cavity signal to the HAM2-HAM3 block. The same feeding will be performed with PRCL, SRCL, DARM and MICH cavities, whose optics are suspended on the other chambers, in and out the corner station. Fig. 5.16 illustrates the chambers and the locations of the cavities of interest in this study.
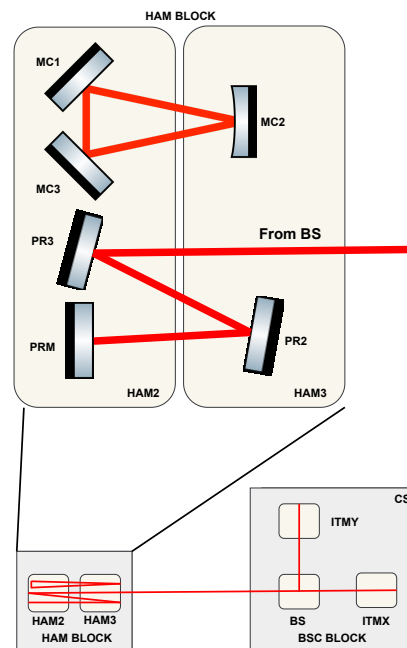
Figure 5.16.: Sketch of the blocks and the locations of the PRC and IMC cavities (not in scale). the suspensions of the mode cleaner and the power recycling cavity lie all on HAM2 and HAM3 chambers. the signal for PRCL come form the Corner Station, which can be grouped as a BSC block.

The same work is foreseen to be done for the other cavities: the very short period of time available during the commissioning break allowed us to modify only the control loop for PRCL. Moreover, during the commissioning break, time is also used to work on the chambers, profiting of the out-of-lock mode. This means that, for every attempt of software modification, a locking trial was needed, to see if the new configuration of the instrument was giving better performance and, also, if it was af-

fecting negatively other sides of the instrument. To try to lock LIGO, we needed people not to work besides the chambers. This was a huge and collaborative work, which involved many people on site, and their time. Despite these challenges, the results obtained are encouraging and validated the analysis of feasibility exposed.

The Power Recycling Cavity Length (PRCL)   We need to connect the ISI to the cavity and to do it we need to know how the PR cavity is going to communicate with the ISI (refer to Chapter 3 for details on the PR cavity). The block diagram in Fig. 5.17 illustrates the simplified concept of the PR cavity connected to the ISIs of the block of HAM2 and HAM3 chambers [4].

The work done in this case is similar to the one done for the HAM chambers, except for the fact that a new filter needs now to be built in order to control how the ISI affect the motion of the PRC optics.

This block diagram has been solved with Mathematica in order to find the correct crossover filters to add. The system was simulated via Matlab and includes information from calibration filter modules, PRM control filters, and HAM Small Triple Suspension (HSTS) models via the calibration filters. This is needed to simulate the addition of the ISI as a PRCL actuator. The aim is to offload low-frequencies to the ISI and hence we need to decide the best configuration of gains and offsets of the crossover filter.

After every simulation which could possibly work for the system, we locked the interferometer and took a measurement of the PRM suspension point. The plot in Fig. 5.18 shows a comparison between the simulation and the actual measured PRCL signal: the outcome is positive because the two traces differ by only a factor of 2, which says that the crossover filter should be adjusted by a factor of 2 to match the real sig-

---

[4]Some insights about the shape of the transfer function of the suspensions are in Appendix C.
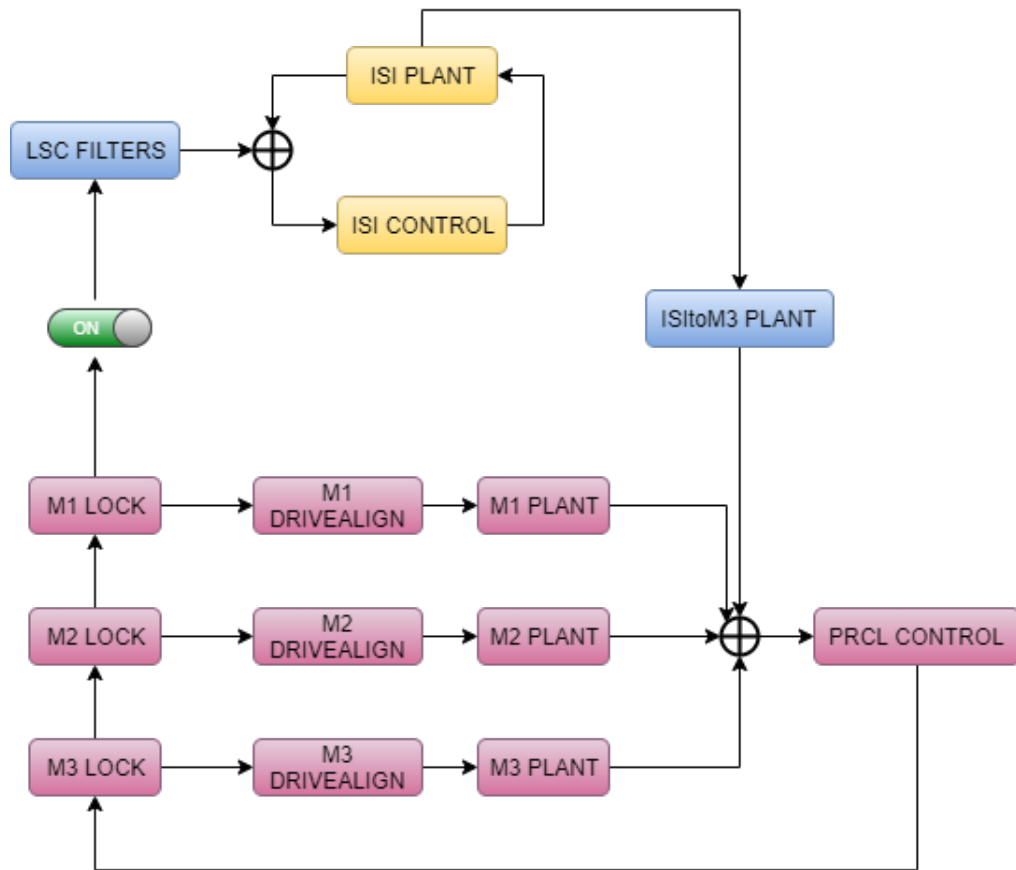
Figure 5.17.: Block diagram of PRCL locked to the ISI. This drawing highlights the details of the PRCL cavity sections involved in active control. In the standard diagram, only the PRCL sections would be involved, while now the cavity is connected via software to the ISI. The LSCfilter block is the crossover filter between the cavity and the ISI (and the connection between them is enabled by a switcher) while the ISItoM3 block represents the plant block of the suspension point of M3 after the connection. The blocks in pink represents the 3 stages of optics involved in the HSTS suspension and the controller already existing on LIGO.

nal. This result has been obtained implementing the filter in Fig. 5.19. The test shows that the offloading works as expected and that the PRCL signal can be driven (and hence controlled) by the ISI.
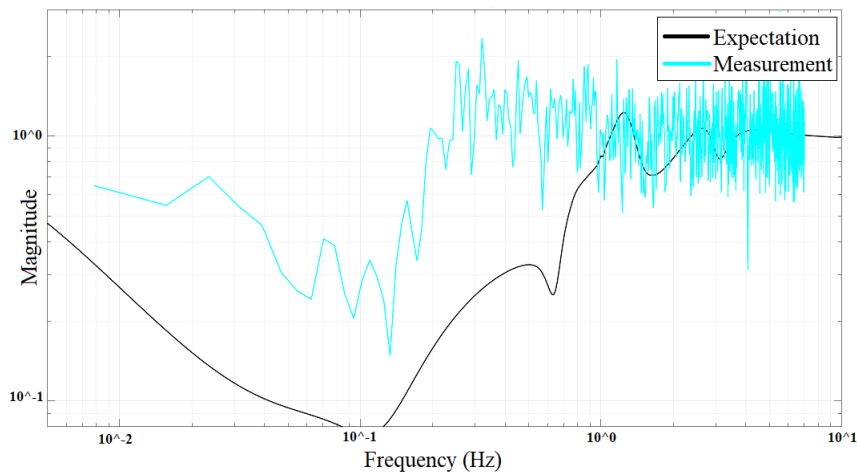
Figure 5.18.: Best measurement of the PRCL signal with respect to the expected signal from the simulations: the two traces differ by a factor of 2.
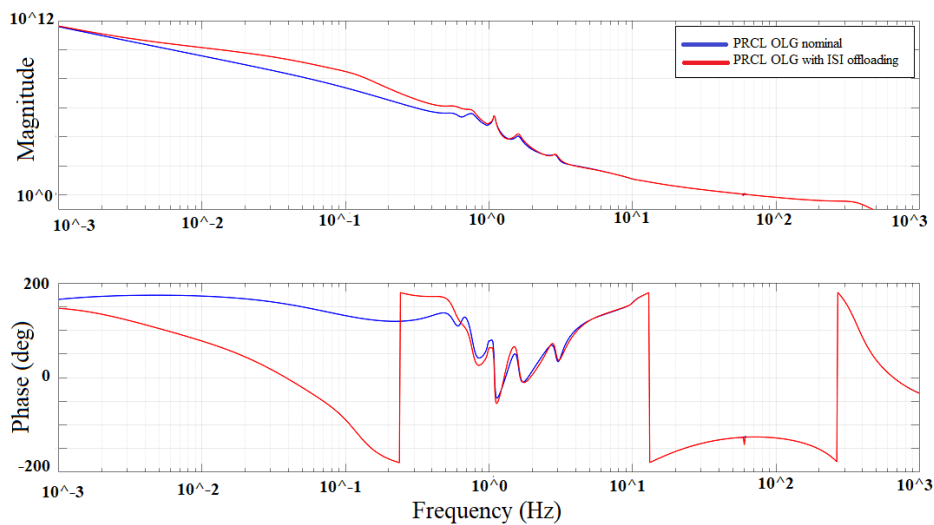
Figure 5.19.: Open loop gain (OLG) crossover filter implemented at LHO for a measurement of PRCL signal in offloading conditions.

5.7. A follow-up test at LHO

The new configuration proposed and tested has changed a crucial section of the structure of LIGO. This change might have consequences on other sides of the instrument, for example affecting other noise sources. A test about the effect of this configuration has been performed at LHO

in 2020 by the LHO, LLO and Seismic teams. This test studied the impact of CPS differential controls on scattered light glitches on O3b run. The teams investigated the reason of an increase in the rate of glitches. The synchronized motion of the chambers with the ground could in principle make the instrument more sensitive to glitches (and other noise sources) which were hidden by the seismic and sensor noises. The study is showing that the configuration is not responsible for this increase, but there is an effect on the sensitivity of LIGO to glitches, when the configuration is activated. The complete study is exposed in details in the LHO logbook post [51].

This is an example of the impact of the CPS differential control on LIGO: it has been used to test the effect of wind in microseismic regions [52] and further tests might help to understand the impact of less seismic motion on other noise sources.

Conclusions

This study is promising to provide a significant contribution to the improvement of LIGO LSC signals and the detector stability when it is running in observing mode. The tests at LHO demonstrated that the experiment succeeded in lowering the seismic motion of the platforms by a factor of 3 at low frequencies and that also the DARM signal benefited from it. The simulations have shown that it is possible to reduce the differential motion of the chambers by a factor of 3 in order of magnitude below 0.1 Hz. The test on the Power Recycling Cavity Length highlighted that the signal can be controlled by the ISI according with the software simulations.

As we saw, the implications go straight to the basics of the instrument: a more stable detector produces a less noisy signal which can last longer into the cavities, assuring a longer observing time and giving the possibility to detect more gravitational waves and in lower ranges of fre-

quency [12] [49]. LIGO Livingston site has also actuated a similar process, following the progression at LHO during the work on site in 2019 [50]. Due to the limited time of the commissioning break, it was not possible to take further measurements of ISI motion and LSC signals, especially with an accurate study of the blending filters. However, since the software skeleton of the new configuration has been built and installed on both LIGO CDSs, further studies and tests were due in 2020 to complete the last steps and test it fully on the interferometer. Meanwhile, the impact of the new configuration is under investigation on both sites: the reduced seismic motion could affect other noise sources that were previously hidden by the seismic and sensor noises, like glitches and wind. The results make then the idea worthy of future developments and improvements, and we are confident that these tests could be carried out in the near future.

6. Laser frequency stabilization for 6D isolation system device

In this chapter I will introduce the 6-Dimension (6D) device, a new technology for inertial isolation. This project was presented to the scientific community at the 10th ET Symposium in 2019 [55]. My contribution to the development of this technique focused on the sensing side: a laser will be injected into the device and will need to be stabilized in frequency for a low-noise readout of the sensing system at lower frequencies. To do it, we propose a new technique based on compact interferometry. The experiment was built and tested in-depth: the laser stabilisation results were limited by excess noise in the sensors and many tests were made to identify and reduce noise. During these tests, it was determined that one of the devices was intrinsically noisier than the other. This work was done entirely at UoB: the design of the project was conducted in 2020, while the experiment was built and tested from September 2020, when the University allowed the return to the laboratory, to July 2021.

6.1. 6D inertial isolation system overview

The 6D inertial isolation system is a device based on a new technology under development at University of Birmingham and at Vrije Univestiteit in Amsterdam, which could enable detection of gravitational waves below 10 Hz [56]. We have already seen the importance for this

frequency window to be opened (chap 2): this sensor could be installed on 2nd generation Earth-based interferometers, with major upgrades, on or under ground, allowing the different instruments to easily use the same device.

As the name reminds, the 6D system investigates the motion of a reference mass in all 6 degrees of freedom, using 6 interferometers. In Fig. 6.1 it is shown a sketch of the design of the facility.
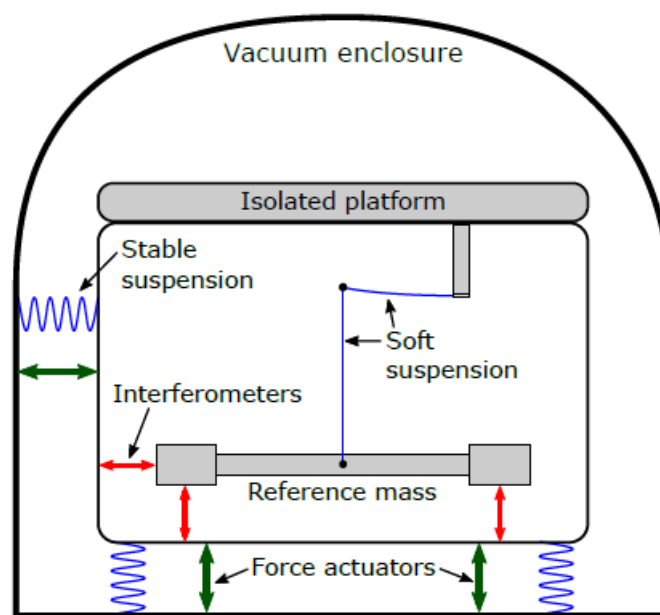
Figure 6.1.: Sketch of the 6D device (Figure taken from [56]). The working principle is based on an isolated, suspended reference mass which is monitored by compact interferometers, detecting the relative motion between the mass and the platform; actuators apply corrections to the platform and the whole apparatus is in vacuum.

All six degrees of freedom are simultaneously low-noise, reducing the cross-coupling affecting low force-noise measurements.

The reference mass, suspended from a single, thin, fused-silica fibre, provides supports in the vertical (Z) degree of freedom. An interferometric readout and control are used in all 6 degrees of freedom.

The major advantages is that this system can improve sensitivity, ther-

mal noise, and tilt-to-translation coupling, providing isolation in all the degrees of freedom with the use of only one device. Currently aLIGO is seismically isolated by three seismometers and twelve geophones [57]: the use of the 6D device would replace three seismometers and six geophones on Stage 1 of the chambers.

What we expect from the 6D system is isolation at low frequencies and reduction of fundamental noises: the thermal noise of the suspension is suppressed by the quasi-monolithic, fused-silica fibre; temperature gradients are kept under control thanks to the vacuum enclosure.

The expected performance is shown in Fig. 6.2: the 6D isolator provides an improvement of the performance of more than two orders of magnitude with respect to what is possible with state of the art seismometers [56].

The key point is to reduce the motion in order to limit the control noise and allow the bandwidth of control loops to be lowered. This is a goal set for a detector sensitive to low frequencies, and for which the 6D device can contribute [5].

Figure 6.2.: A comparison of the expected performance of the 6D isolator and that of current seismometers (Figure taken from [56]).

6.1.1. HoQI technology

The 6 interferometers dedicated to the sensing role of the facility are the HoQI devices (Homodyne Quadrature Interferometer) developed at UoB [58].

HoQI is a compact, fibre-coupled interferometer with high sensitivity and large working range. In Fig. 6.3 you can see the optical layout of the device:
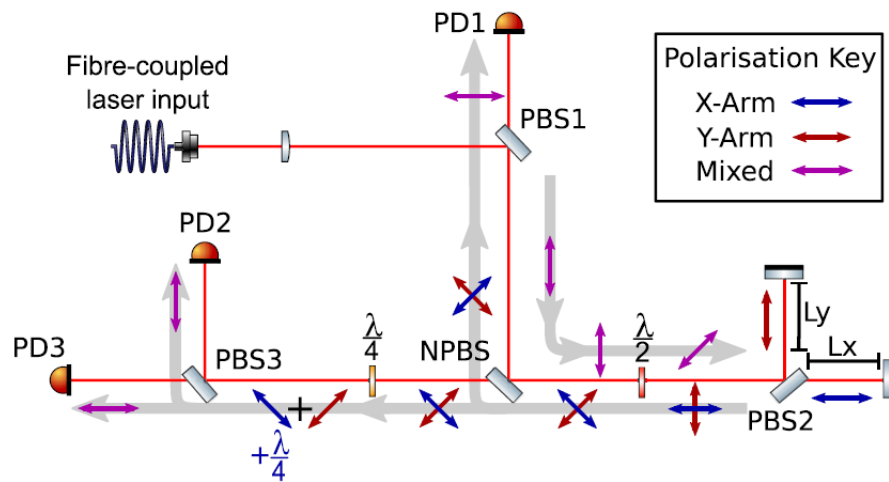
Figure 6.3.: HoQI optical layout (Figure taken from [58]). The working principle is based on a Mach-Zender interferometer which uses two different beam splitters to recombine the beam independently. Moreover, the required differential phase shift is generated by a polarization scheme conveniently designed.

This device has been designed to sense motion at low frequency, with a sensitivity of 2×10^{-14} m/ $\sqrt{(Hz)}$ at 70 Hz and 7×10^{-11} m/ $\sqrt{(Hz)}$ at 10 mHz [58]. In the frame of compact devices, HoQIs are designed to be very small in size, so they can easily be attached to sensors: good results were obtained when combining HoQI devices to inertial sensors to create an "interferometric inertial sensor" [59]. They are then ideal for 6D purposes, not only for their high sensitivity, but also for their small size.

The six HoQIs used for the 6D device need to be fed by a laser source

that is sent into the vacuum chamber: my project focused on this source, specifically how to stabilize it in frequency.

6.2. Laser stabilization: requirements and key technology

The laser chosen as source for 6D is a 1064 nm RIO ORION Laser Module (see Fig. 6.4). This has been chosen for its low frequency noise, inexpensiveness and small size, relatively to other options. The key point in the stabilization of the frequency noise of this source is that the technology will be based on HoQIs: the same devices used by the 6D, but with a longer arm-length mismatch, are sensitive enough to be installed also to stabilize the laser source. This solution is very convenient in terms of costs and presents practical advantages: the HoQIs are known devices, compact in size and, as we will see, they allow the setup to be moved easily (in vacuum or in air), according to the main 6D requirements.

Figure 6.4.: Picture of the RIO Orion laser mounted on a breadboard.

What we want from this source is a low-noise readout for the HoQIs inside the 6D tank, and thus the laser source needs to be as low noise in frequency fluctuations as possible at frequencies below 0.5 Hz, because this is the range of frequencies where the 6D isolator is aimed to detect and control seismic noise: we are going to use two Rio Orion laser mod-

ules to obtain a frequency stabilization suitable for 6D requirements. Constraints to these requirements are mainly given by the HoQIs. For 6D readout, HoQIs are built in such a way that the arm length mismatch is as small as practically possible, e.g. $L_{6D} < 3$ mm. Limitations to this number are given by BOSEM size ($\pm$ 2 mm) and the ability to adjust it, once the devices are in vacuum. Another parameter to take into account is the noise of HoQIs, which is $H = 6 \times 10^{-14}$ m/$\sqrt{Hz}$ at about 1 Hz [58]. Frequency fluctuations depend on both these parameters and we want it to meet the following requirement:

$$\delta f_{6D} \ll f \times \frac{H}{L_{6D}} \simeq 5000 \frac{Hz}{\sqrt{Hz}}, \qquad (6.1)$$

where f is the laser frequency.

The technique we are going to adopt to stabilize the laser in frequency, as anticipated, is to use HoQIs, because we can associate frequency fluctuations to fluctuations of arm length:

$$\delta f = \frac{\delta L}{L} \cdot f, \qquad (6.2)$$

and this arm length can belong to a HoQI placed on the optical bench. The use of compact interferometers to stabilize the frequency of solid-state lasers without the use of cavity locking is new and allows the whole set up to be small in size. This technique, in combination with cheap laser sources, makes the set up competitive with other more expensive products.

We can then apply the same relation of. eq. 6.2 to the arm length of the HoQI used for the laser stabilization, remembering that the requirement of $\delta f \ll 5000$ Hz/$\sqrt{Hz}$ must remain valid. So, constraints to the arm length in this case are due also to the size of the bench and the whole set up.

We said we want a compact setup, but the arm length of this HoQI (say

L$_{stab}$) can have a wider range of sizes to fit the requirement. For example, for L$_{stab}$ = 1 m we have:

$$\delta f_{stab} = f \times \frac{H}{L_{stab}} \simeq 16\frac{Hz}{\sqrt{Hz}}, \tag{6.3}$$

which is still much lower than the threshold of 5000 Hz/$\sqrt{Hz}$.

Since we want the setup to be as much compact as possible, we need to find the lowest possible L$_{stab}$ which gives an interesting δf_{stab}, compared to the current performance of RIO Orion and the best products available.

In the plot in Fig. 6.5 there is the analysis and comparison with two of the best products available.
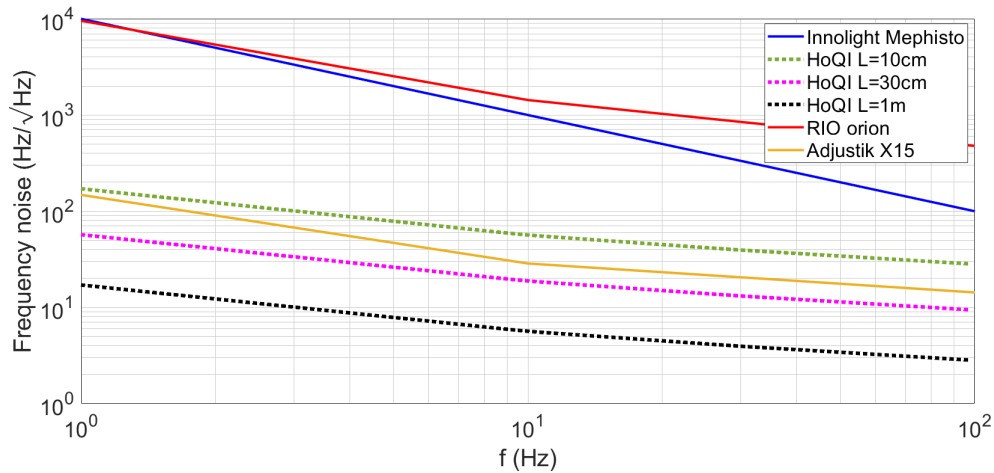
Figure 6.5.: Analysis and comparison of RIO Orion laser with other products and with the configuration involving HoQIs. For an arm mismatch of 10 cm, δf_{stab} is still below the threshold, being 168 Hz/$\sqrt{Hz}$, still fitting the 6D requirements.

It is evident that we cannot build a HoQI with L=10 m. If we want our device to be competitive even with the best product (ADJUSTIK X15, shown in orange line), we will need a L=30 cm. However, our purpose is to make the set up *compact* and *competitive* with most of the avail-

able products, so the best compromise is choosing L=10 cm. With this configuration, the device will still be competitive with ADJUSTIK X15 in terms of price.

Fig. 6.6 shows a plot of the measured frequency noise of the Rio Orion laser modules and the level of stabilization required by the 6D with the chosen L_{stab}.
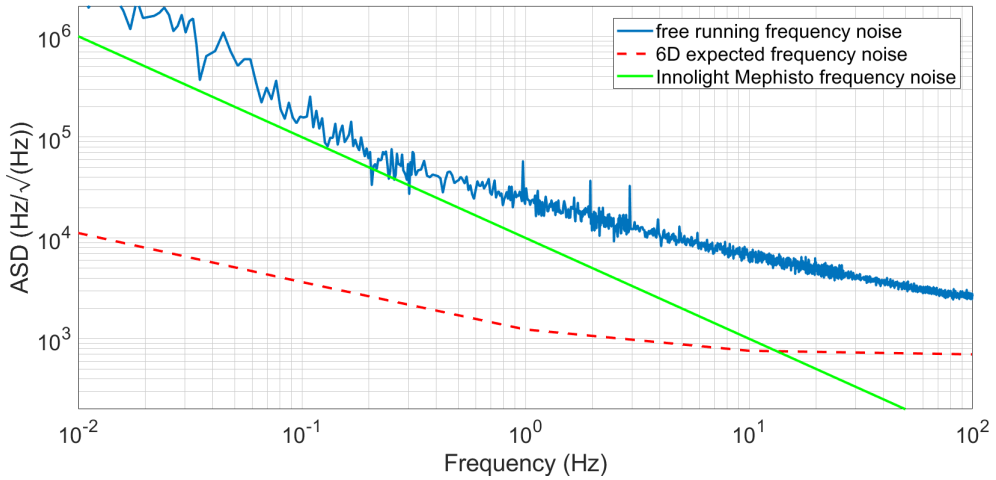
Figure 6.6.: Measured free running frequency noise of the Rio Orion laser modules compared with the frequency noise of the Mephisto Light laser module. The dotted line is the threshold of the 6D requirements for stabilization of its laser source, which is the goal we aim to achieve with the proposed setup. This threshold has been built using L_{stab}=10 cm and the HoQI noise and ADC floors as in [58].

6.3. Experiment design

The optical set up for the stabilization of the laser source is built on a 800 mm × 650 mm breadboard: this choice allows to adjust the position of the laser source easier when the light is sent to the 6D vacuum chamber. The setup includes two RIO Orion lasers with output power 12 mW each, and a double-check of the light signal through an optical heterodyne detection: the beat frequency is monitored to assure that the two

light frequencies are as much similar as possible. The frequency noise from the heterodyne detection is measured by a frequency counter: we chose this device because it is the least ambiguous, lowest noise, lowest systematic-error, best calibrated measure of the relative fluctuations of the two lasers available for our purposes.

The frequency of the lasers is tunable via temperature and input modulation: in the first case, the Thermo-Electric-Controller (TEC) is driven by a software provided by the manufacturer, while in the second case the module can be integrated to any software code to produce an output voltage between +4 V and - 4 V, that is sent to the lasers: the frequency tuning efficiency with this method is around 80 MHz/V, when a sinusoidal modulation is applied at 10 kHz. From specifications, the range of tuning spans between 50 and 100 MHz/V.

To minimise airflows, the optical setup has been enclosed into a box made of foam.

Opto-mechanical design   The optical layout is shown in Fig. 6.7: the two lasers have a twin optical layout. There is a Faraday Isolator (FI) at each output and then a 1 to 4 fibre beam splitter (BS) which separates the beam into 4 outputs of equal power: 3 outputs go into the vacuum chamber (for a total of 6 laser inputs, one for each 6D HoQI into the vacuum chamber). The remaining output is sent through a fibre coupler to a Schafter-Kirchhoff collimator and gives an output of about 1.2 mW for each laser; this proceeds freely on the breadboard towards a 1 inch, 10/90 (R/T) beam splitter: 10% of the light is sent to a fast DC coupled 125-MHz photoreceiver (PD) acted to sense the beat-note of the two lasers; two 1 inch mirrors deviate one of the two laser beams towards the transmitting surface of another 1 inch beam splitter, which combines the light from both lasers towards the photoreceiver; the other 90% of it is sent to the HoQIs, one for each laser. The optical path lengths (OPL) have been set to be equal, to assure the same beam size

from both lasers at the photoreceiver.

The photoreceiver has strict constraints about the beam size and the input power: a focussing lens in front of the active area assures that the beam size is suitable to fit the 0.3 mm active area. Neutral density damping filters are added along the OPL, because the maximum input power of the device is 55 μW.

The whole optical setup lies on the breadboard and it is relatively easy to align because all the optomechanical components have been manufactured to make the beams out of the collimator to travel at the same height as HoQI components and the photoreceiver, so that there is no need of pitch tuning.
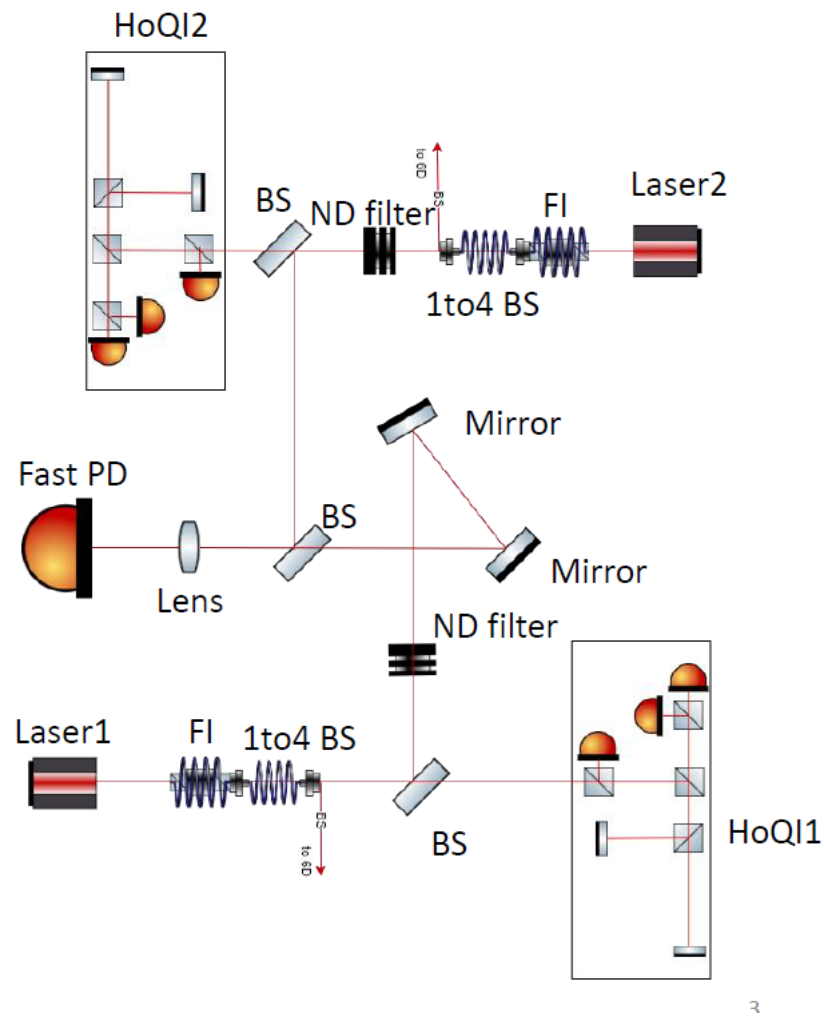
Figure 6.7.: Optical layout of the laser stabilization experiment.

HoQI design HoQIs for 6D laser stabilization have been built to fit the requirements, as shown previously: the adjustable arm-length mismatch is of 10 cm; the photodiodes have a bigger active area with respect to the one of the HoQIs inside the 6D vacuum chamber, because the laser spot size is larger than the one travelling into the 6D device. Moreover, this type of HoQI is independent from any inertial sensor, so both the arms end with mirrors on steering mounts, and instead of corner cubes used to for the A+ devices. Table 6.1 shows other small details that have been adapted for this experiment.

	A+ HoQIs	**Laserstab HoQIs**
Platform thickness	6 mm	1 cm
Size	65×75mm	65×200mm
Corner Cubes	2	0
PD active area	3.6×3.6mm	5.8 ×5.8mm
Steering mirrors	1	2

Table 6.1.: Main differences between the original HoQI and the one used for 6D laser stabilization.

In Fig. 6.8 there is a photo of the HoQI built for this experiment.

Figure 6.8.: Photo of one of the HoQIs built for the laser stabilization experiment.

The photodiodes are Hamamatsu S2386-8K and the optical layout is

similar to the one shown in the figure 6.3: there are commercial 0.5 inch cubic beam splitters (three polarizing and 1 non polarising) mounted on custom cubic bases, two 0.5 inch mirrors on steering mounts, one 0.5 inch $\lambda/2$ waveplate and one 0.5 inch $\lambda/4$ waveplate, both mounted on a custom base allowing them to rotate for fine tuning. The whole optical set up is placed on a 75 mm $\times$ 200 mm $\times$ 10 mm baseplate.

The two HoQIs have been tuned to obtain the best fringe visibility, which is 0.8 for HoQI1 and 0.6 for HoQI2. The technique used to measure the fringe visibility is based on measured power on a sin vs cos plot, once the beams have been aligned to overlap in far field and produce interference. The plot show a *lissajous* figure, which can be tuned by improving the alignment with the steering mirrors and rotating the waveplates for power adjustments. When the adjustments are optimal (same power amplitude and in quadrature phase offset), the *lissajous* is a circumference[1]. Fig. 6.9 shows the sinusoids of the HoQI photodiodes after fringe visibility optimization.

6.4. AC-coupled control loop

To acquire our data, we need to connect the HoQIs and the beat-note receiver to a data acquisition system. At UoB we have 3 CDS racks and one of them is dedicated to 6D. As shown in Fig. 6.10, HoQIs will need a pre-amplifier, an Anti-Aliasing (AA) device and an Analog to Digital Converter (ADC) before connecting to CDS (Fig. 6.10).

The beat-note receiver is 15 V powered and connected to a frequency counter, and then to the CDS. A detailed scheme of the electronics is shown in Fig. 6.11.

The sensing and control system of the experiment is based on the HoQIs: the software code manipulating the HOQIs signal and driving the

---

[1]For details about the characteristic equations of HoQIs and the working principle, refer to [58].
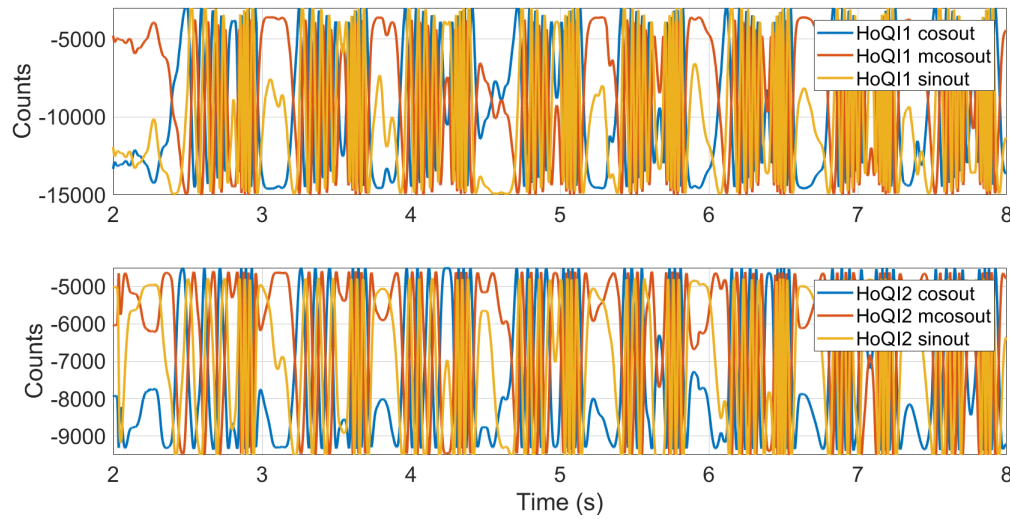
Figure 6.9.: Example of how we set the fringes of the HoQIs to obtain the desired alignment. Every photodiode detects the fringes independently from the others: to obtain the same response, we adjusted the offsets and the gains of each diode on the pre-amplifier and via software.

input modulation is written with Matlab Simulink and controlled by the CDS. The controller filter has been built taking into account all the features of the loop and implemented into the CDS: the filters are shown in Fig. 6.12: their performance has been tested looking at the stability of the beat-note peak when each filter is switched on, and when they are on together as the full controller filter.

The lasers can then be controlled via input modulation of the current feeding the lasers, through the feedback control loop built via the CDS, where HoQIs act as the sensors.

6.5. Noise hunting

The performance of the setup depend strongly on the HoQIs because they are the sensing and feedback devices of the setup: the noise budget in Fig. 6.13 shows that the measured HoQI readut follows the free
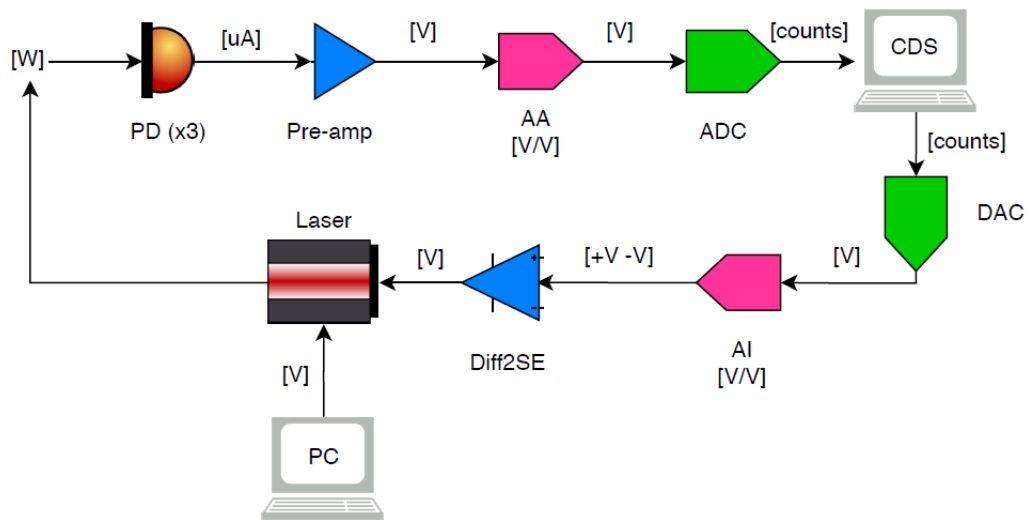
Figure 6.10.: Basic scheme of the row signals for laser frequency control: the power detected by the photodiodes is converted into μA and sent to a pre-amp, one for each HoQI; the pre-amps convert the signal into double-ended voltage to be sent to an ADC. The output of the CDS is a $\pm$ 10 V double-ended signal out of the DAC: since the lasers require a $\pm$ 4 V single-ended input, the double-ended signal is converted into single with a custom differential- to single-ended amplifier of gain 2.5.

running frequency noise of the lasers detected by the frequency counter at low frequencies, and then it sits on the ADC noise (estimated as in [58]) at frequencies above 100 Hz. What we are interested in is getting the lowest possible frequency noise from the lasers, reducing the noises affecting the HoQIs. The improvement of HoQIs sensitivity is crucial to obtain the best performance in sensing frequency fluctuations, in order to provide the correct and stable control and feedback to the setup.

6.5.1. Tested noise sources

There are several noise sources to take into account and that we tested and minimized: air currents and vibrations from electronics and cables have been reduced placing the optical setup into a foam box and moving
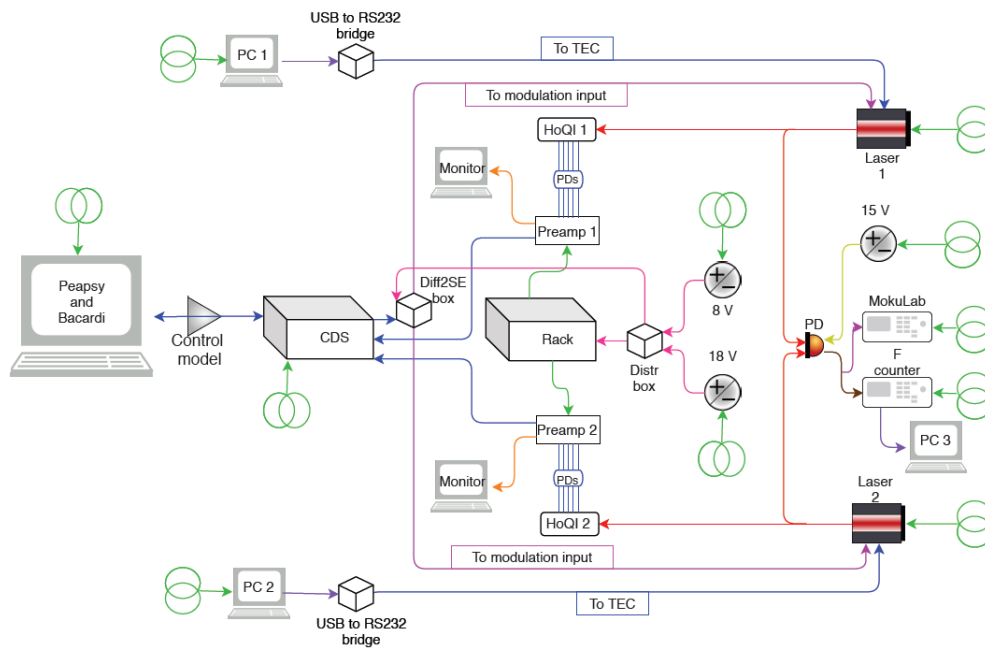
Figure 6.11.: Detailed scheme of the electronics designed for this experiment. The different colors of the arrows represents different types of cables. Bacardi and Peapsy are the front-end and the workstation controlling it, as we named them at UoB. Differential to single ended converters (Diff2SE) are needed because the CDS supports differential outputs while the pre-amps are single ended. The Mokulab is the device used as an oscilloscope and/or as a spectrum analyser, connected to the beat-note fast photoreceiver. Green arrows indicate power supplies. The frequency counter can be connected to a computer to acquire data or a USB drive can be inserted to save data directly from the device. The temperature modulation requires the use of a software provided by the manufacturer and installed on computers. Each laser needs its own software connection.

the electronic devices suitably. The lasers have been left outside the box to avoid overheating inside, due to their heat dissipation. Cables have been isolated from the table and the breadboard by rubber feet.
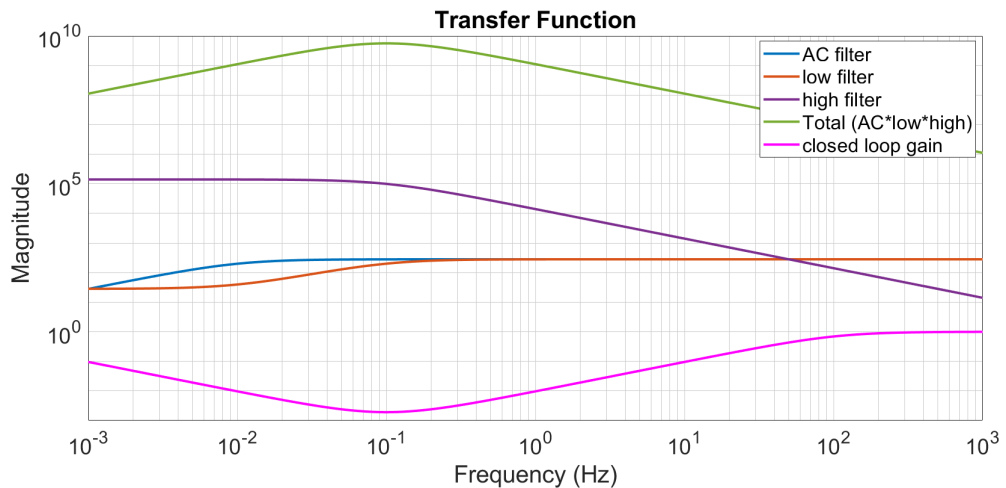
Figure 6.12.: Plot of the controller filter installed into the CDS (green) and of the closed-loop expected gain when this filter is applied (magenta). This design should push the gain from below 0.1 Hz, assuring stability when applied at lower frequencies.
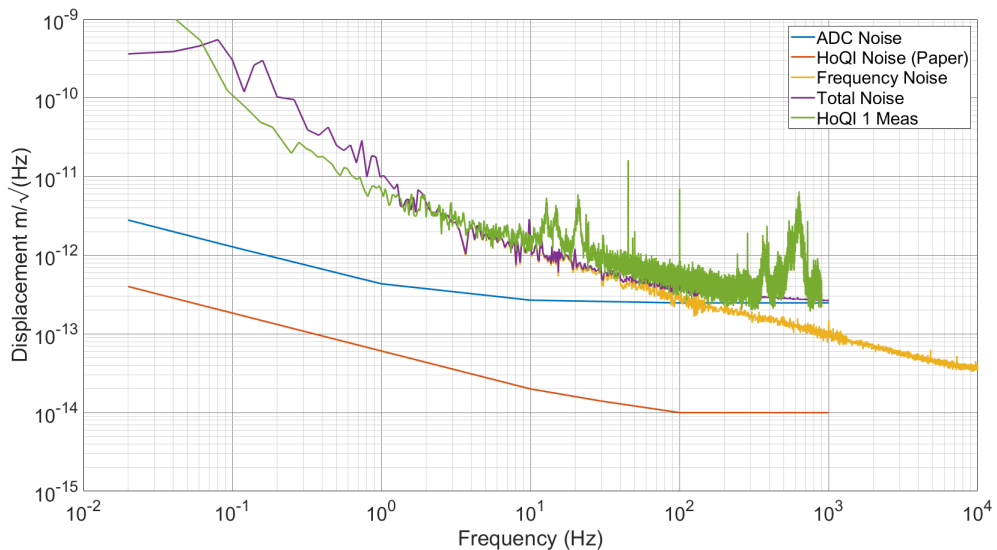
Figure 6.13.: Noise budget of the laser stabilization setup, in free air with the controller turned off. The paper which provided the HoQI noise and the ADC noise is given by [58].

Offset/gain parameter matching When aligning HoQIs, a significant contribution to the results was given by the fact that the fringes needed to be adjusted to match in gain and offsets: this was done via CDS and

it provided one of the most important issues (and noise sources) during the tests. Imperfect fringe-visibility and parameter matching dominate the coupling from intensity to measured-phase, and we saw substantial improvements when these values were optimised. We had insufficient diagnostics to fix the issue, mainly because, to create fringes, the HoQIs needed to be mechanically shaken and tuned, and this could be done only manually and in dark room (to avoid room light to affect the offsets), providing imprecise results. We had no proper way to adjust the laser frequency without changing the intensity, and we had no way to adjust the intensity without changing the frequency. This made the offsets and gains change and pollute the measurements. The plots in Fig. 6.14 show the difference between the row fringes generate while shaking HoQI1 and the ones generated after optimizing the parameters. We observed variations in the settings, which needed to be double-checked and readjusted before every measurement. This was an important issue that slowed the tests down and that it is worthy of further tests and data analysis.
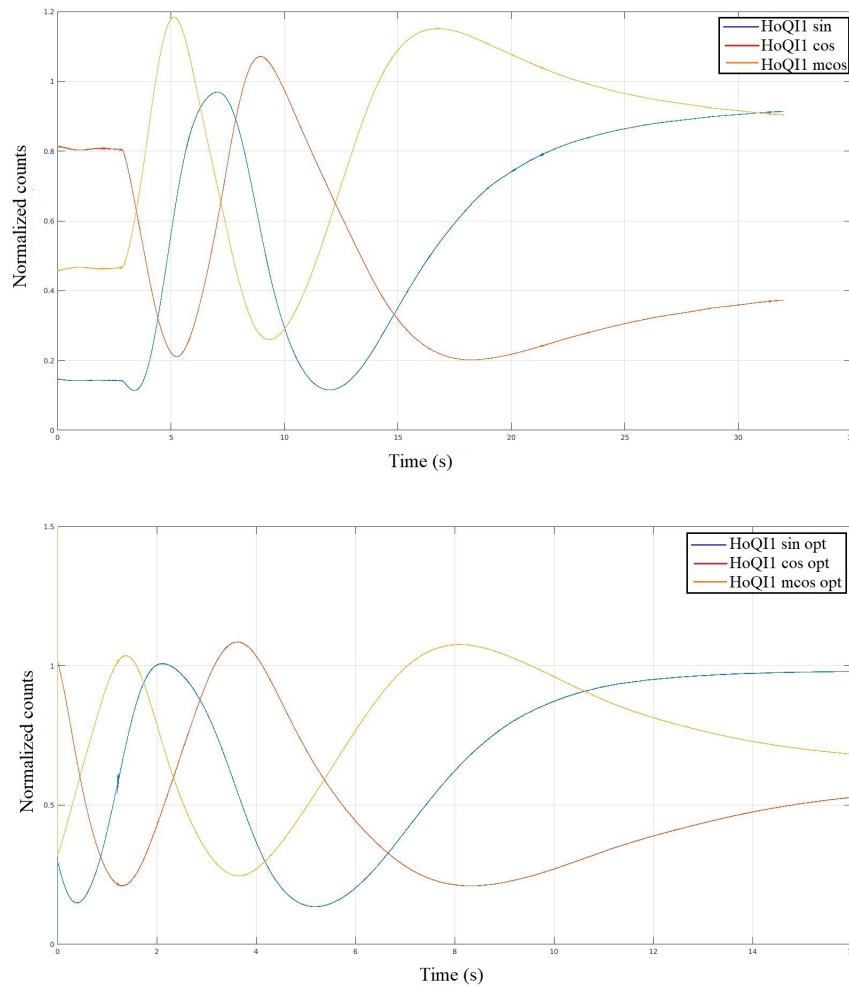
Figure 6.14.: Row and optimized fringe parameters for HoQI1. This fringes has been generated by changing the temperature of laser1: this induced a frequency variation, detected by HoQI. The plots show the row fringes from each photodiode (upper) and the ones after the optimization of the gains and offsets for each photodiode, with respect to a reference one (lower).

Acoustic noise The test in Fig. 6.15 shows that the setup is sensitive to acoustic noise: we injected a sound at 75 Hz and both HoQIs clearly detected it. Moreover, we found out that HoQI1 is detecting some noise around 22 Hz that HoQI2 is not able to sense: the two peaks in the figure are present in every condition of the laboratory and time of the day. The source of this noise is still under investigation: it could be a

permanent sound in the lab non audible by humans. The fact that only HoQI1 can detect it could be due to its position with respect to the noise source: it might be closer to it than HoQI2. Imperfections in the optics and general setup of the HoQIs are also taken into account.
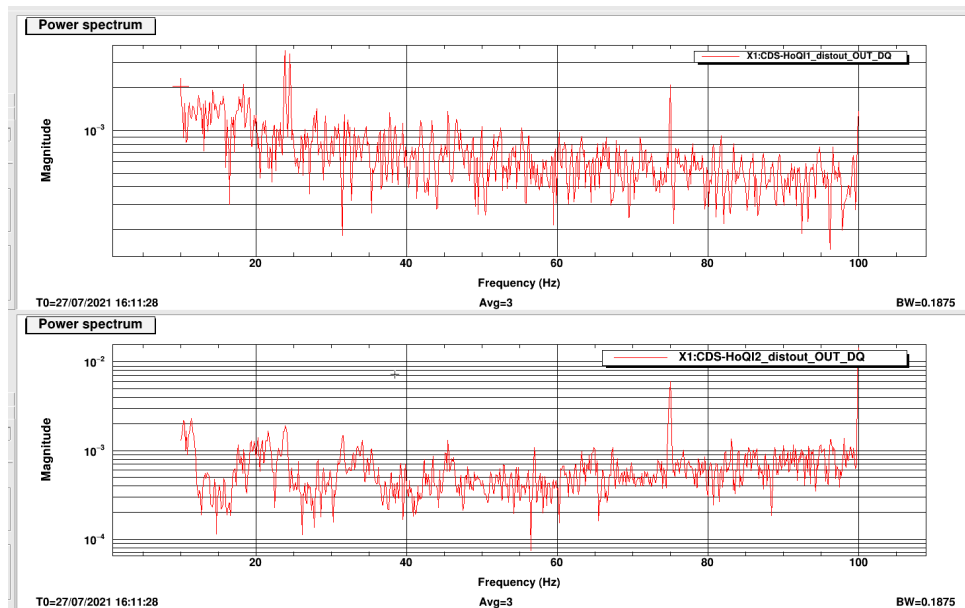
Figure 6.15.: Test of the setup to sound stimulation. The peaks at 75 Hz shows that both HoQIs are sensitive to acoustic stimulation; HoQI1 is also detecting another noise around 22 Hz, which is instead non-visible by HoQI2.

The role of the temperature Temperature changes affected dramatically the measurements. The two lasers can be driven also via temperature modulation: this method has been used to move the beat-note peak along the frequencies and set it around 60 MHz, being this the set-point we decided for it. However, both laser modules are sensitive to changes of the room temperature, which make the peak move out from the setpoint on large time scales (hours): this affects long time measurements. The stabilization of the room temperature requires the use of the air conditioning, which in turn creates air currents visible by the

setup below 10 Hz (Fig. 6.16 shows the difference between two tests taken with and without AC).

Temperature changes are also responsible for deformations of metals; this induces noises into the HoQI platforms because of the different materials they are built of: temperature change induces differential expansion. In a rigid structure this creates stress and some of the bolted connections slide, introducing noise. This issue has been reduced by inserting rubber rings between the connections: this allows the baseplate to expand differentially without creating stress.

HoQIs performance When monitoring the output of the HoQIs, we noticed that HoQI2 is much noisier than HoQI1: Fig. 6.17 shows an out of loop measurement of the output of both HoQIs. This discrepancy has been investigated: possible reasons for that could arise from the laser source of HoQI2, alignment and clipping on the optics, fringe visibility, spurious light, mechanical defects in HoQI2 setup. The laser source has been changed to be the same as HoQI1 and further tests showed that HoQI2 is performing the same way. This relieved the laser of any responsibility, since now the same source is feeding the two HoQIs in the same way. The alignment and the clipping on the optics have been carefully checked and possible sources of stray lights have been meticulously covered. The fringe visibility has been double-checked: the test is still showing more noise from HoQI2 output. What remains to inspect is the possibility of mechanical defects in the optics or in the setup of HoQI2, the latter being a concrete possibility due to errors in manufacturing.

Another reason of concern about HoQI2 behaviour is that it is not consistent with tests in loop (see Fig. 6.19 later): this might be due to intensity noise coupling, which effect might be more evident than in HoQI1 due to internal defects, giving a noisier output when the setup is in loop.
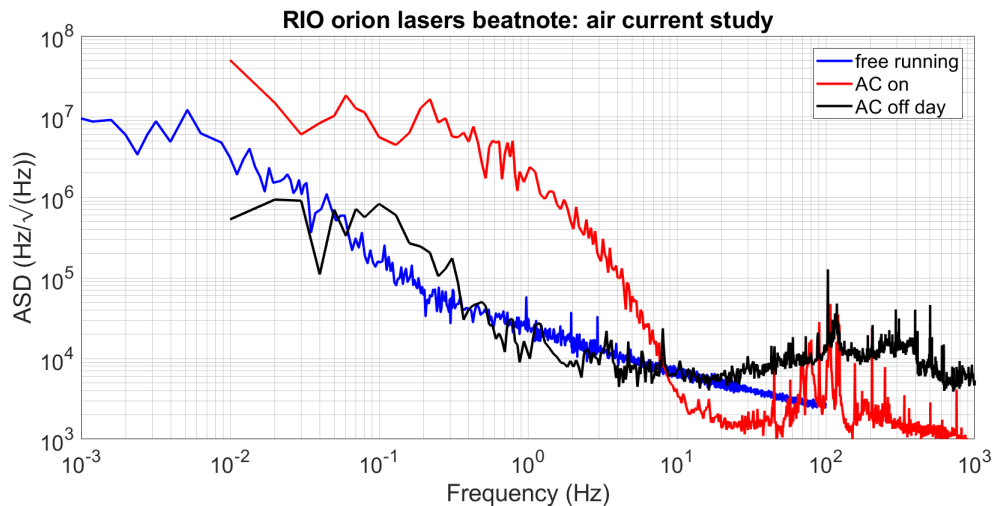
Figure 6.16.: Test of the impact of air conditioning (AC) on the frequency stability. From this plot the free running frequency measured by the beat-note is compared to the frequency measured when the setup is in loop in different AC conditions: the red trace shows a measurement taken when the AC was on, during the night: the AC creates air currents, and it is also responsible for changes in the temperature of the room and of the lasers, and it can induce dust in the OPL. All these contributions are affecting the setup below 10 Hz; the black trace shows the same test with no AC: below 10 Hz the trace is much quieter. The higher noise above 10 Hz is due to the fact that this test has been taken in daylight time, and HoQIs suffered the vibrations of the building. After this test we reduced the free space OPL between the optics were possible, filled the empty spaces of the box and reduced the free space between the last optic and the beat-note photoreceiver, to reduce air flows. All the following tests have been taken with AC off.

Power variations The datasheets of the laser modules put in evidence that the power modulation is different for the two lasers: in particular, for laser2 it is higher than laser1 (compare the datasheets reports in [60] and [61]). This might in part explain why HoQI2 is in general noisier than HoQI1. We monitored the power of both in-loop lasers: ac-
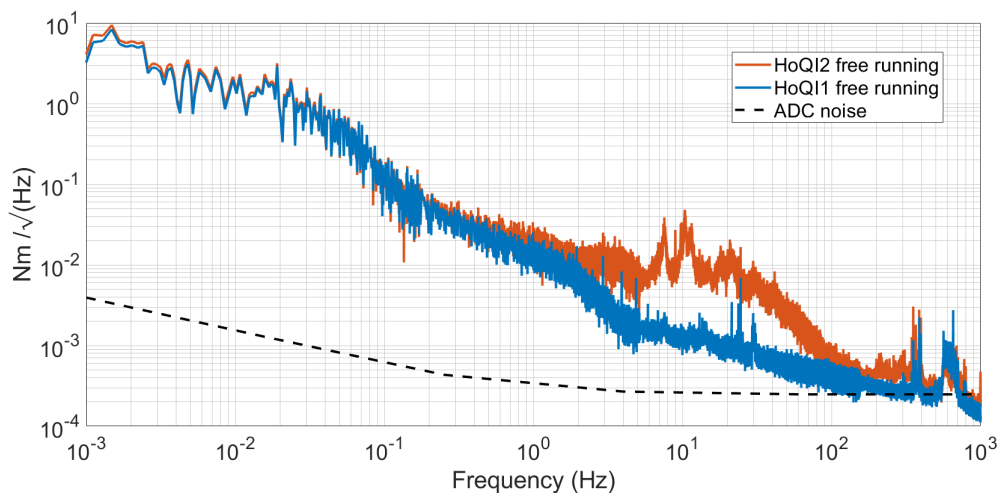
Figure 6.17.: Difference between HoQI1 and HoQI2 outputs in an open-loop test.

cording to the datasheet, the power modulation of laser 2 is about 1.56 times higher than for laser 1. In Fig. 6.18, the power variation measured at HoQIs input during frequency modulation for the two lasers is consistent with the datasheet. The higher power variations of laser 2 might induce higher intensity fluctuations, which could affect HoQI2.

6.5.2. Loop performance

The behaviour of the two HoQIs has been tested in loop and out of loop, to check if they are detecting and responding correctly to the injection of the controller filters through the input modulation of the laser modules. The expectation is that the HoQIs output in out-of-loop mode should show the injection of the gain: Fig. 6.19 shows that the expectations are satisfied.

This test confirms that HoQI2 is in general noisier than HoQI1, especially above 1 Hz: this affects laser stabilization measurement and loop stability, thus it has been deeply investigated. The higher intensity fluctuations of laser2 can partially explain the reason of HoQI2 noise.

Figure 6.18.: Power measured at the input of the two HoQIs, after the polarizing beam splitter (PBS) over 1 hour of data. Laser 2 shows a higher power variation over the same time with respect to laser 1, for a change about 1.56 higher. This is consistent with the datasheet statements, and might also be a reason for the higher noise into HoQI2. However, for practical reasons the power photodiode has been placed after the PBS, a contribution of this optic in this effect is not excluded: there might be internal imperfections which could be accounted for possible polarization variations there on in the fibres.

6.6. Laser stabilization: tests and results

The tests have been performed measuring the stability of the beat-note peak around the 60 Hz setpoint: the frequency counter used for this measurements is a Keysight 53230A 350 MHz - 20 ps. The output of the fast photoreceiver is DC-coupled and can be directly connected to the counter. The measurements has been recorded on a USB drive: the data provided by the counter are in frequency (Hz).

Several tests have been taken in different conditions for noise hunting along the frequency range of interest, the best measurements are shown
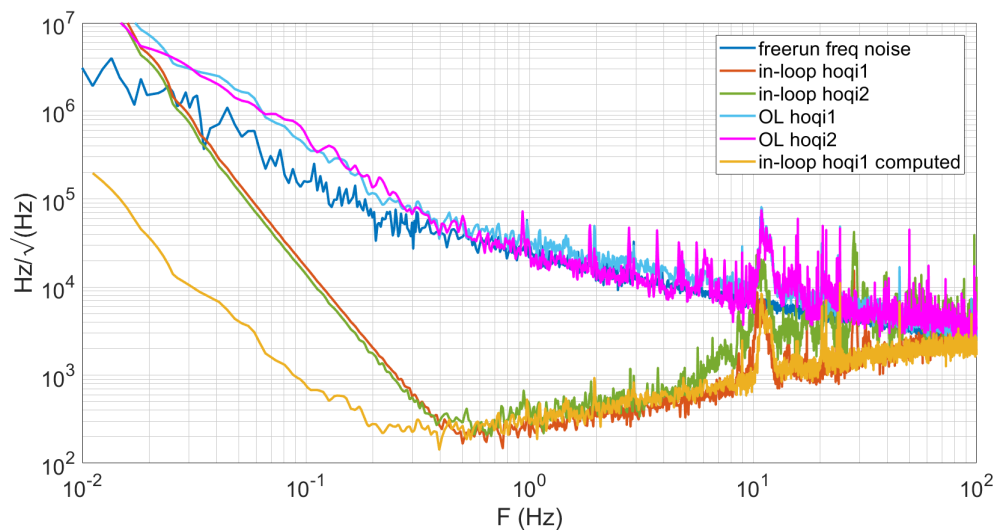
Figure 6.19.: In-loop test of HoQIs performance. The out-of-loop traces (cyan and purple) are following the free running frequency noise trace (blue) as expected, while when the loop is closed the HoQI outputs (green and red) show that the controllers are pushing the expected gain (orange). There is an evident un-match with the orange trace below 0.4 Hz and this is likely due to spectral leakage.

in Fig. 6.20. The tests with the heterodyne detection revealed that the system is very sensitive to the external noise sources described above and that the two HoQIs are not robust and stable enough to assure the stability of the loop, despite the robustness of the controller filter. The solution for reducing these noises might be placing the HoQIs in vacuum.

6.7. An alternative test

An alternative test has been made to make sure that the input modulation is effectively reducing the frequency noise of the lasers. Since we found that HoQI2 is noisier than HoQI1 and that laser2 has larger power fluctuations, we decided to use laser1 to feed both HoQIs. The
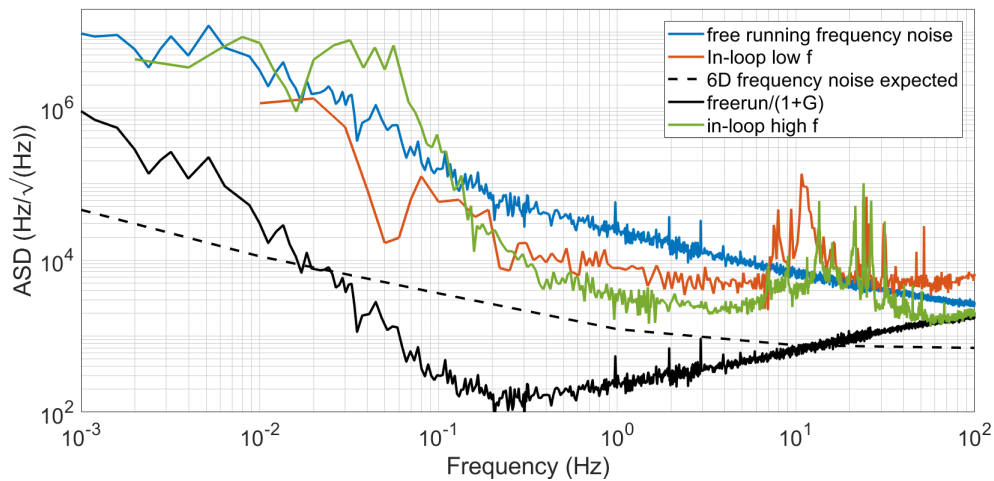
Figure 6.20.: Results of frequency stabilization with respect to the free running frequency noise: the in-loop red trace shows the frequency stabilized lasers as detected by the frequency counter, monitoring the beat-note between the two lasers in the lower frequency range. This trace is the best measurement we obtained below 1 Hz, where we reached 1.67×10^4 Hz/$\sqrt{Hz}$ at 0.05 Hz; The green trace is a test taken with the counter set to a higher frequency range: this test shows a result of 3.6×10^3 Hz/$\sqrt{Hz}$ at 1 Hz. This is also the test which showed the quietest results above 10 Hz, demonstrating that the HoQIs can reach a good level of stability in air. The black trace is the expected gain activated by the controllers, which is set to maximise the stabilization below 1 Hz: when it is lower than the green and red curves, we are not limited by loop gain. When it is below the dashed-black curve, there is sufficient loop gain to meet our noise target.

new concept is to let only HoQI1 be the in-loop sensor, while HoQI2 will act as the out-of-loop sensor.

Results are shown in Fig. 6.22 and are encouraging: the frequency noise of the out-of-loop sensor is lowered by about one order of magnitude when the controller on laser1 is active. This means that the control loop works well and that there are still more external noise sources that are reducing the performance of the HoQIs, impacting also on the mea-
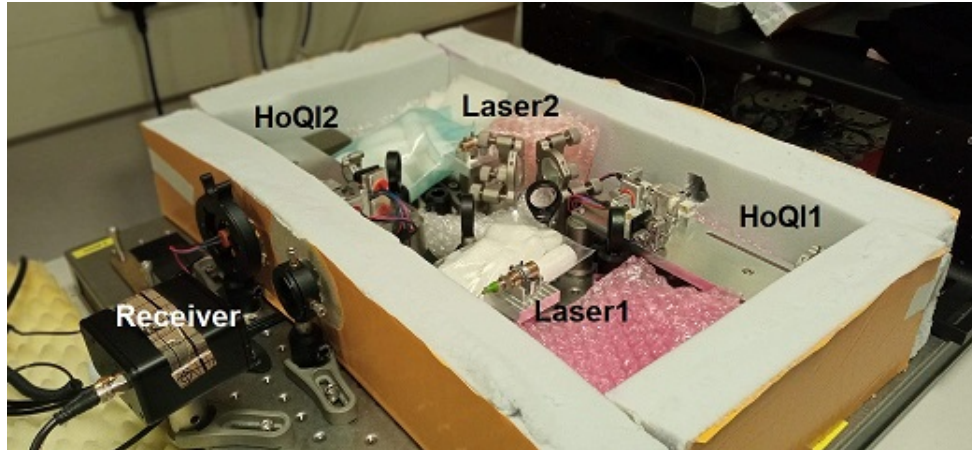
Figure 6.21.: Photo of the experiment setup for frequency stabilization of the 6D laser source. Only the optical setup has been placed inside the foam box, which suitable apertures to let the beams go to the power photodiodes and the photoreceiver outside the box. The gaps inside the box have been filled in order to reduce the air currents along the OPL in free air and a lid covers the whole box.

surement through the heterodyne detection.

This test confirmed also that HoQI2 is still noisier than HoQI1, especially in closed loop, despite the use of the laser with less power fluctuations: this clarifies that HoQI2 noise arises from other external sources that HoQI1 is non-sensitive to or imperfections of the setup. A test in vacuum could solve the doubts about the external sources and HoQI2 assembly.
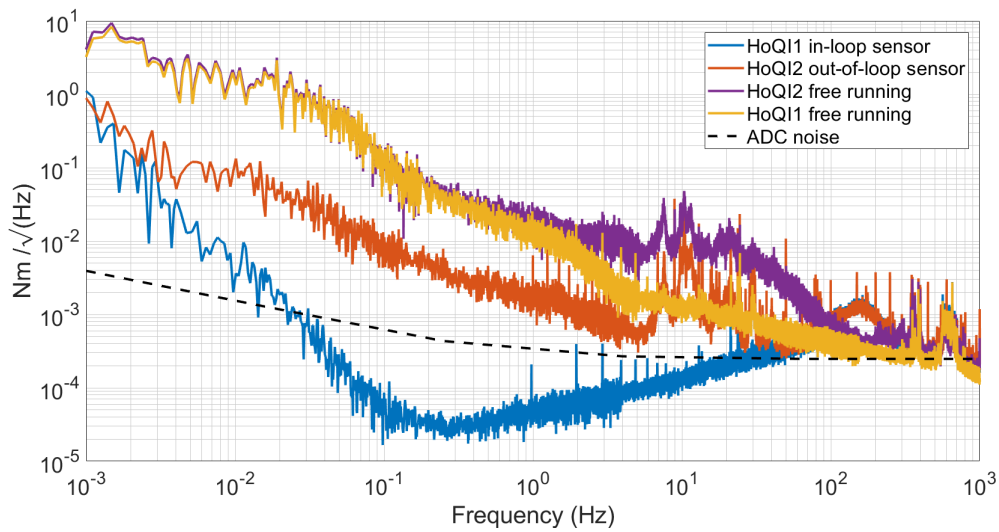
Figure 6.22.: Alternative test for frequency stabilization: the out-of-loop sensor (HoQI2) is less noisy by an order of magnitude when the in-loop sensor is actuated by the controller filter. This is a proof that the frequency noise of the laser is reduced by the control loop.

Conclusions

The results of this experiment showed that it is possible to stabilize the frequency of the laser source of the 6D device using the technology presented: a compact, easy to handle setup which makes use of small interferometers of the same type that are used inside the 6D sensor. With this technology, we managed to reach a frequency stabilization of 3.6×10^3 Hz$/\sqrt{Hz}$ at 1 Hz, without the need of installing the prototype in vacuum.

This is already a promising result, but not yet sufficient for the requirements of 6D, especially below 1 Hz. The results showed that we are not limited by loop gain, that acoustic noise and vibrations are important noise sources, that intensity noise and frequency-to-intensity coupling limit performance, and that both HoQIs show different coupling to these effects. The alternative test showed an indirect measurement of laser stabilization, because the out-of-loop HoQI improved its output signal of about one order of magnitude when the laser was modulated by the

controller filter. This test highlighted that the frequency stabilization through the heterodyne detection depends on the stability and robustness of the HoQIs. A concrete plan for next tests is to place the setup in vacuum: this will suppress all the external noises and will possibly highlight the intrinsic issues of HoQIs.

This test has already been considered as a possibility during the experiment design: the HoQI setups can be placed inside the 6D vacuum tank independently from the rest of the components of the stabilization breadboard and electronics.

Summary and future developments

This thesis is intended to provide a contribution to the improvement of gravitational-wave interferometers in the lower frequency bandwidth (below 30 Hz). My PhD project then focussed on developing new devices and improving already existing control structures for this aim, through three different experimental works: the study of optical levers for sensing and reducing tilt motion, the modification of the control system of LIGO in order to improve the control of seismic motion on the platforms and the frequency stabilization of the laser surce for the 6D isolation system device.

The optical lever can be in principle a good device to sense tilt motion over long lever arms. However, the noise budget indicated a small frequency window of good operation, while below 0.1 Hz the levers are limited by the ground motion along the z axis, but it opened the way to further tests to improve the technology: with a good sensing system of tilt motion, the addition of an actuation system able to reduce this noise will be crucially helpful to stabilize the suspension points of the optical chains and then of the whole cavity.

The study on the CPS and LSC offloading is promising to provide a significant contribution to the improvement of LIGO LSC signals and the detector stability when it is running in observing mode. The tests at LHO demonstrated that the experiment succeeded in lowering the seismic motion of the platforms by a factor of 3 at low frequencies and that

also the DARM signal benefited from it. The simulations have shown that it is possible to reduce the differential motion of the chambers by a factor of 3 in order of magnitude below 0.1 Hz. The test on the Power Recycling Cavity Length highlighted that the signal can be controlled by the ISI according with the software simulations.

The results of the laser stabilization experiment showed that it is possible to stabilize the frequency of the laser source of the 6D device using the technology presented: a compact, easy to handle setup which makes use of small interferometers of the same type that are used inside the 6D sensor. With this technology, we managed to reach a frequency stabilization of 3.6×10^3 Hz/$\sqrt{Hz}$ at 1 Hz, without the need of installing the prototype in vacuum. This is already a promising result, but not yet sufficient for the requirements of 6D, especially below 1 Hz. This experiment requires further tests in vacuum in order to isolate the HoQIs and improve the performance.

Future developments

All the three experiments proposed in this thesis can provide an important contribution for the low frequency noise reduction and are worthy of further tests and developments, as demonstrated by the experimental results and the simulations.

The optical levers and their performance under stimulation of vertical motion is a matter of studies at the AEI, and it would be ideal to fix the electronics and perform further tests with a lever arm of 10 m. This would be of great help to understand if optical lever can be useful to be installed on the platforms of the interferometers. A further analysis of the control system for reducing the tilt motion is required and it could be an ideal topic for another PhD project.

The project developed at LIGO is currently in use, as highlighted in Chapter 5. It is straightforward to complete the job done there with

more appropriate blending filters and fine tuning of the software design for locking the chambers: this work was due to 2020 or 2021, when I was supposed to go back to Hanford and conclude the work. However, it was not possible due to the pandemic. It would then be useful to go back when possible, or that another student into the fellowship program could bring the project to a final stage.

The frequency stabilization of the lasers for the 6D isolation system requires another test in vacuum and, probably, independent tests on the single HoQIs to verify if there are internal defects. This is supposed to be studied at University of Birmingham. Since the setup is already built, the controller is designed and is working with good performance and it needs to be completed in order to be installed into the full 6D device, these further tests should be straightforward: an internship student or a Master's student could take care of this.

A. Assembling suspension chains for A+ at LHO

In 2019 I spent some months working on LIGO Hanford site. Along with the study exposed in Chapter 5, I offered my lab experience in building the HSTS (HAM Small Triple Suspension) to be installed for the LIGO A+ upgrade. The assembly team was composed by me, Dr. Rahul Kumar and Dr. Jeff Bartlett. The suspensions have been installed in 2021 under the supervision of Rahul in HAM7 and HAM8, and will be known as Filter Cavities (FC). The FC will enhance squeezing capabilities and help improve the quantum noise. Here there is a gallery of original photos of the lab-work done together. It was an intense and very interesting team work, which enhanced my skills in working into a clean room, with delicate structures that needed to be assembled very precisely.

Figure A.1.: Mounting the blades onto the top of the suspension skeleton. On the right photo: the blades mounted and fixed and the required angle.

Figure A.2.: Left: one of the wire used to suspend the test mass. The wires suspending the bottom mass are stainless steel wires, 0.0047 inches-thick. The upper stages are suspended by 0.008 inches-thick wires. Right: Technique to prepare the wire with the right tension: a given weight is applied and left for 5 minutes.

Figure A.3.: Mounting the wires for the test mass suspension on their support. Right: Jeff and I while installing the wire support into the suspension cage.

Figure A.4.: Top: Rahul and I installing the bottom test mass and suspending it with the wires. The bottom mass is a mirror of 2.8 Kg. Bottom: Rahul while measuring the alignment of the test mass into the suspension cage.

B. Control loops

B.1. Control theory

The theory of controls is a branch of science and technology which studies how to drive a given dynamical system. This is generally characterized by inputs and outputs and the former can be manipulated to obtain a desired output, which is chosen by a reference setpoint. The design and the technology involved depends on the system, but in general they imply a sensing section, a software section which can modify some features of the input and a feedback section to check that the manipulation of the input signal gives the output as set by the reference.

B.1.1. Principles: control loops

The collection of all the sections forms a control loop and manages the behaviour of a given variable under exam. Control loops can be:

- Open-loop: the control action is independent from the output.

- Closed-loop: the control action depends on the desired output conditions. This kind of loop uses feedback loops, that assure that the process is correctly going on, i.e. the value of the variable under exam is that of the setpoint.

In order to design a control loop, we need to build all the subsystems up: the main one is the **plant**, which is the physical parameter to be controlled; the plant is measured by one or more **sensors**, which detect

a deviation (if any) in the signal from the reference setpoint. An error signal is then produced and processed by a **controller** into a correction signal that is sent to an **actuator**. The actuator applies the correction to the plant.

B.1.2. How to: block diagrams

Block diagrams are useful graphical instruments to describe, study and build a control loop. Each element of the control system is represented by a block and each block is joined by lines with arrows showing the sequence of controls. Following the logical steps stated before, we can then draw the block diagram of a basic system to be controlled as in Fig. B.1.

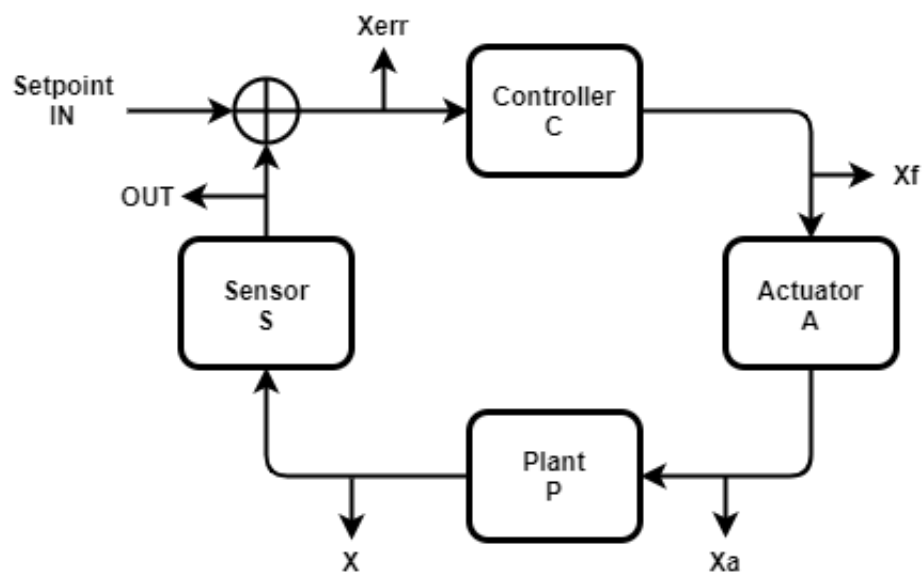Figure B.1.: Basic block diagram of a control loop. The setpoint is injected as an input.

Every variable of interest at the output of each block can be evaluated by *solving* the diagram. Referring to Fig. B.1, solving a block diagram means solving the system of equations involving the variable under exam and each block. The product of the components of the block diagram give the total gain of the loop.

B.2. Control analysis

Once the control loop has been schematically drafted, it needs to be finalized: the software section implies instructions. These are given by a computation of the transfer functions of the whole system, which gives the response in the frequency domain of the output to a given input. The computed (and measured) transfer function will then be modified with suitable filters to make the output adjust to the reference setpoint.

B.2.1. Transfer functions

Every dynamical system is characterized by equations of motion in the time domain. In order to study the system in the frequency domain, it is possible to apply a Laplace transform. So, for any function f(t) in the time domain, the Laplace transform is defined as:

$$F(s) = \int e^{-st} f(t) dt \tag{B.1}$$

where s = a + iω.

A transfer function is defined as the ratio between the output and the input, in the frequency domain. For any input X(s) and output Y(s), the transfer function is:

$$T(s) = \frac{Y(s)}{X(s)} \tag{B.2}$$

and so the output is characterized by the product between the transfer function and the input signal in the Laplace domain, which is the Laplace transform of the convolution of the two functions in the time domain[1].

Since, in general, a function can be written as a product of polynomials, the transfer function is also in the form:

---

[1]An interesting demonstration of this statement can be found in [65]

B. Control loops

$$T(s) = C\Pi_{i,j}\frac{(s - z_i)^j}{(s - p_i)^j} \tag{B.3}$$

where z and p are the ith zeros and poles of the polynomial, of order j and C is the amplitude. This form is useful to study the stability of the system:

- $Re(p) < 0$: the system is asymptotically stable;

- $Re(p) = 0$ with j = 1: the system is marginally stable;

- $Re(p) = 0$ with j > 1 or $Re(p) > 1$: the system is unstable.

The gain of the system is defined as the ratio between the amplitudes of the input and output, i.e. it's the absolute value of the transfer function:

$$G = \frac{|Y(s)|}{|X(s)|} = |T(s)| \tag{B.4}$$

and the phase is φ = arg(T(s)).

In the frame of control loops, the transfer function is given by the gain contributions of all the subsystems of the loop. So, recalling the previous block diagram, if we want to know the transfer function of the system, we need to solve the system of equations:

$$\begin{cases} X_{err} = IN + OUT \\ x_f = C \cdot X_{err} \\ X_a = A \cdot X_f \\ X = P \cdot X_a \\ OUT = S \cdot X \end{cases}$$

$$OUT = S \cdot P \cdot A \cdot C \cdot (IN + OUT) = G \cdot (IN + OUT), \tag{B.5}$$

where G = S P A C. The transfer function is then:

$$\frac{OUT}{IN} = \frac{G}{1 - G}, \tag{B.6}$$

which is also called the *open loop gain*. Since normally the variable we want to control is X_{err}, we want to solve the closed loop:

$$X_{err} = IN + G \cdot X_{err} = \frac{IN}{1 - G}.$$

(B.7)

The term 1/(1-G) is called *closed loop gain.*

B.2.2. Phase and magnitude interpretation: the Bode plot

The Bode plot is a graph representing the response in frequency of the magnitude and phase of the system under exam. It is largely used to define the marginal conditions for the stability of the loop. The magnitude is expressed in dB = $20\log_{10}(x)$ and it is computed as the absolute value of the transfer function:

$$| T(s) | = \sqrt{T \cdot T^*}.$$

(B.8)

The phase is expressed in degrees (deg) and it is computed as:

$$\varphi = -\arctan\left(\frac{ImT(s))}{Re(T(s))}\right).$$

(B.9)

In the frame of loops, the closed-loop gain was:

$$G_{CL} = \frac{1}{1 - G},$$

where G is a pole for this relation. This means that if G = 1, G_{CL} diverges and the loop is unstable. On the phase plot, this corresponds to φ = 180°. In general, when the trace on the phase plot approaches this value at certain frequencies, it means that the loop that we are building is unstable in that region.

B.2.3. Spectral density

Spectral densities are views of a signal in a frequency spectrum. It is a useful tool to detect effects on the signal during processing, like

peaks due to harmonics, or resonances. The physical parameter used in this study is the power spectral density, which measures the power of a signal as a function of frequency and has units of $W/Hz^{-1/2}$. When there is no direct power associated to the measurement (like in case of Volts) the units are in terms of the square of the signal per Hz. In some cases, an Amplitude Spectral Density (ASD), defined as the square root of the power spectral density, is used when the shape of the signal is quite constant; in this case the units are in the form of $1/Hz^{-1/2}$ and the variations in the ASD will then be proportional to the variations of the signal itself.

B.2.4. Coherence

The coherence is a statistic relation between two signals or data sets x and y. It is defined as the ratio between the cross spectral density of the two functions and the product of the spectral densities of each function:

$$C_{xy}(f) = \frac{\mid ASD_{xy}(f) \mid^2}{ASD_{xx}(f)ASD_{yy}(f)}. \tag{B.10}$$

Coherence is a useful parameter to estimate the correlation between the two signals. In control loops, it can be used to verify how much the output can be predictable by the input. The values of the coherence lies between 0 and 1 and two signals are considered optimally correlated if their coherence approaches 1.
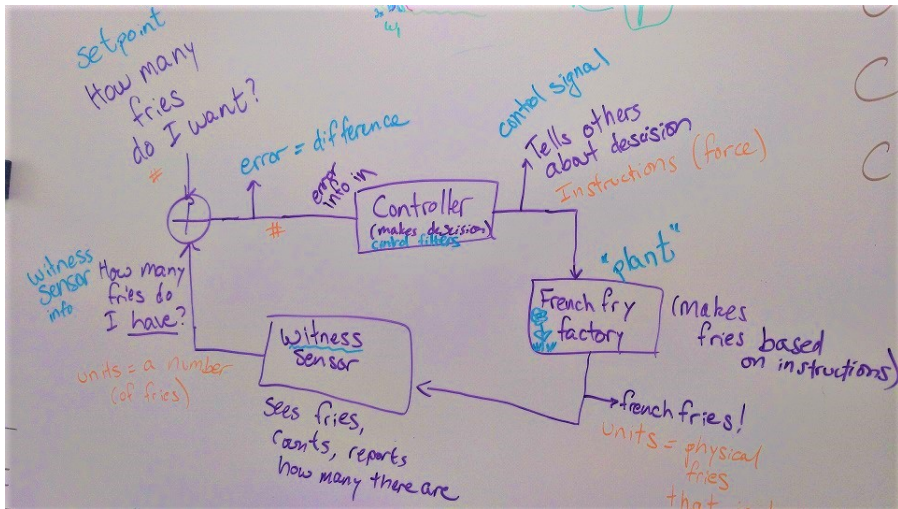
B.3. The French fry factory

Figure B.2.: The French fry factory: basic principles of a control loop as explained by Dr. Jenne Driggers during a private conversation at LIGO Hanford. Original photo.

C. Useful insights

C.1. The first Detection

On 14th September 2015 the two LIGO antennas observed for the first time a signal from a gravitational wave produced by the merger of two black holes. This was the very first time that a merger of such massive and elusive objects could be observed.

The gravitational-wave signal has been named GW150914 and has been emitted by 2 black hole of masses of 36 $M_\odot$ and 29 $M_\odot$, which merged at a distance of 410 Mpc (z = 0.09)and produced a final BH of 62 $M_\odot$. The remaining 3 $M_\odot$ have been radiated in gravitational waves. Fig. C.1 shows the signal detected from LIGO Hanford and LIGO Livingston.

This detection has been the result of a wide scientific collaboration which efforts made possible a discovery that deserved the Nobel Prize in Physics in 2017 to the pioneers of gravitational wave hunting *'for decisive contributions to the LIGO detector and the observation of gravitational waves'*.

C.2. LIGO duty cycle

The efficiency of the instrument was shown in Fig. 5.1, and the upper chart is reported here.

The legend of this pie chart is defined in the detchar summary pages *https://summary.ligo.org/O3/*. From a private conversation with Dr. Jeff Kissel, it is generally intended as in Tab C.1.
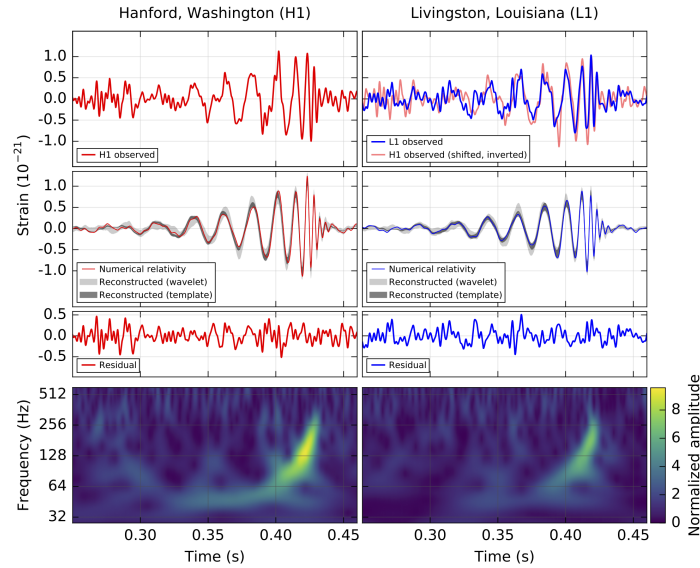
Figure C.1.: First detection of a gravitational wave signal [4]. The event is shown for both observatories at the time of observation 09:50:45 UTC on 14th September 2015. The top row is the gravitational wave amplitude for Hanford (H1) and Livingston (L1). In the L1 panel, there is a visual comparison of the two signals: the wave passe through L1 first, H1 signal (in orange) is shifted by the 6.9 ms of difference, and inverted due to their mutual orientation. The second row shows the consistency of the measured signal with expectations independently computed. Third row shows the residuals after subtraction of the measured time series and the numerical waveform. Bottom row is the same signal in frequency vs time, where it is evident the increase of frequency with time.

Other definitions and details about duty cycle and performance of the instrument can be found in [68] and [69].

Figure C.2.: The gravitational-wave scientific community (image kindly provided by [67]).
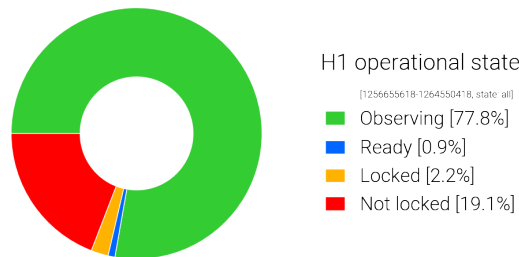
Legend	Jeff's definition
Observing	We are at nominal low noise, no one is messing with the interferometer
Ready	We are at nominal low noise, but the low-latency processes aren't functioning normally
Locked	LIGO is locked, and the automated lock-acquisition system thinks it's in nominal low noise, but the operator hasn't confirmed that we're ready yet
Not locked	every other time.

Table C.1.: Duty cycle legend of LIGO as explained by Dr. Jeff Kissel (from a private conversation).

C.3. The PRCL suspension filters

The transfer function of the suspensions of the PR cavities, illustrated in the block diagram 5.17 in Chapter 5, are shown in the plot C.3. The complicated shape of this functions makes difficult to manually solve the PRCL block diagram and simulate the motion of the optics. To solve the diagram, the Mathematica software has been used and several tests have been tried to look for the best filters and their effects (as reported on LHO logbook posts 52623, 53160, 53442, 53442).
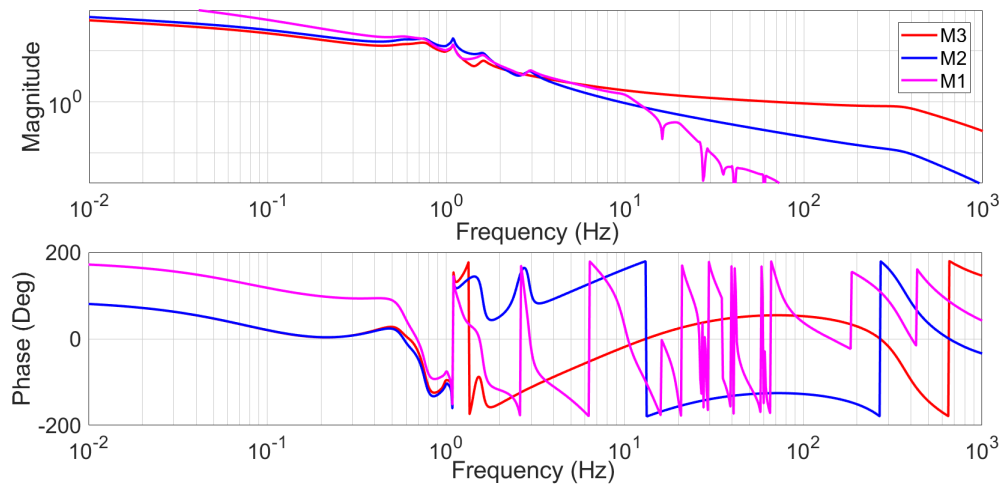
Figure C.3.: Transfer function of the suspensions for PRCL.

Bibliography

[1] S. Weinberg *Gravitation and Cosmology: principles and applications of the General Theory of Relativity*, John Wiley & Sons, Inc., 1972

[2] M. Maggiore *Gravitational waves - Vol. 1: Theory and Experiments*, Oxford University Press, 2013

[3] J. V. Narlikar *An introduction to Relativity*, Cambridge University Press, 2011

[4] B. P. Abbott, *Observation of Gravitational Waves from a Binary Black Hole Merger*, Phys. Rev. Lett. 116, 061102, 2016

[5] H. Yu et al, *Prospects for Detecting Gravitational Waves at 5 Hz with Ground-Based Detectors*, Phys. Rev. Lett. 120, 141102, 2018

[6] S. Bird et al., *Did LIGO detect dark matter?*, Phys. Rev. Lett. 116, 201301, 2016

[7] M. Branchesi, *Multi-messenger astronomy: gravitational waves, neutrinos, photons, and cosmic rays*, 2016 J. Phys.: Conf. Ser. 718 022004

[8] LIGO Scientific Collaboration and Virgo Collaboration, Fermi GBM, INTEGRAL, IceCube Collaboration, AstroSat Cadmium Zinc Telluride Imager Team, IPN Collaboration, The Insight-Hxmt Collaboration, ANTARES Collaboration, The Swift Collaboration, AGILE Team, The 1M2H Team, The Dark Energy Camera GW-EM Collaboration and

the DES Collaboration, The DLT40 Collaboration, GRAWITA: GRAvitational Wave Inaf TeAm, The Fermi Large Area Telescope Collaboration, ATCA: Australia Telescope Compact Array, ASKAP: Australian SKA Pathfinder, Las Cumbres Observatory Group, OzGrav, DWF (Deeper, Wider, Faster Program), AST3, and CAASTRO Collaborations, The VINROUGE Collaboration, MASTER Collaboration, J-GEM, GROWTH, JAGWAR, CaltechNRAO, TTU-NRAO, and NuSTAR Collaborations, Pan-STARRS, The MAXI Team, TZAC Consortium, KU Collaboration, Nordic Optical Telescope, ePESSTO, GROND, Texas Tech University, SALT Group, TOROS: Transient Robotic Observatory of the South Collaboration, The BOOTES Collaboration, MWA: Murchison Widefield Array, The CALET Collaboration, IKI-GW Follow-up Collaboration, H.E.S.S. Collaboration, LOFAR Collaboration, LWA: Long Wavelength Array, HAWC Collaboration, The Pierre Auger Collaboration, ALMA Collaboration, Euro VLBI Team, Pi of the Sky Collaboration, The Chandra Team at McGill University, DFN: Desert Fireball Network, ATLAS, High Time Resolution Universe Survey, RIMAS and RATIR, and SKA South Africa/MeerKAT *Multi-messenger Observations of a Binary Neutron Star Merger* ApJL, 848:L12, 2017

[9] P. Fritschel, B. Lantz, *Report on the workshop on Low Frequency Noise in LIGO, April 6 -7, 2021*, Low Frequency Workshop, April 2021 DCC L2100055

[10] ERC Workshop, Frebruary 2021

[11] Low Frequency Workshop, University of Birmingham, August 2018

[12] B. Lantz, *System-wide upgrades to improve the Seismic Isolation and control of detectors beyond A+*, talk, 2020

[13] A. D. Goulding et al, *Discovery of a Close-separation Binary Quasar at the Heart of a z~0.2 Merging Galaxy and Its Implications for Low-*

frequency Gravitational Waves, The Astrophysical Journal Letters, 879:L21 (7pp), 2019

[14] J. S. B. Whyithe et al, *Low-frequency gravitational waves from massive black holes binaries: predictions for LISA and PULSAR timing arrays*, The Astrophysical Journal, 590:691–706, 2003

[15] Advanced LIGO Systems Group, *Advanced LIGO Systems Design*, DCC document T010075-v3, 2017

[16] B. P. Abbott et al, *GW150914: The Advanced LIGO Detectors in the Era of First Discoveries*, Phys. Rev. Lett. 116, 131102, 2016

[17] D. Martynov et al., *The Sensitivity of the Advanced LIGO Detectors at the Beginning of Gravitational Wave Astronomy*

[18] F. Matichard et al, *Seismic isolation of Advanced LIGO: Review of strategy, instrumentation and performance*, Class. Quantum Grav. 32 185003, 2015

[19] J. Kissel, *On Seismic Isolation in 2nd Generation Detectors*, GWADW talk, 2012, dcc.ligo.org/LIGO-G1200556

[20] K. Izumi, D. Sigg, *Advanced LIGO: length sensing and control in a dual recycled interferometric gravitational wave antenna*, 2017 Class. Quantum Grav. 34 015001

[21] C. Di Fronzo *Optical sensors for improving low-frequency performance in GW detectors*, Mid-Course Assessment, University of Birmingham, 2018

[22] C. Di Fronzo et al., *Optical Lever for interferometric inertial isolation*, poster, LVC meeting, Maastricht 2018, https://dcc.ligo.org/LIGO-G1801693

[23] B. Lantz et al., *Estimates of HAM-ISI motion for A+*, T1800066-v2, March 2018, https://dcc.ligo.org/LIGO-T1800066

Bibliography

[24] S. Cooper et al., *Ham ISI model*, Technical note, University of Birmingham, March 2018, https://dcc.ligo.org/LIGO-T1800092

[25] S. M. Köhlenbeck, *Towards the SQL Interferometer Length Stabilization at the AEI 10 m-Prototype*, PhD thesis, Gottfried Wilhelm Leibniz Universität Hannover, 2018

[26] L. KranzHoff for the AEI group, *A novel vertical inertial sensor for with phasemeter readout*, poster, LVK September 2021

[27] D. Tuyenbayev, *Extending the scientific reach of Advanced LIGO by compensating for temporal variations in the calibration of the detector.*, PhD thesis, University of Texas, 2017

[28] Venkateswara et al., *Subtracting tilt from a horizontal-seismometer using a ground-rotation-sensor*, Bulletin of the Seismological Society of America (2017) 107 (2): 709-717

[29] R.V. Jones et al., *Some developments and applications of optical levers*, 1961 J. Sci. Instrum. 38 37

[30] K. Agatsuma, *Optical lever for KAGRA*, GW monthly seminar at Tokyo, 2014

[31] B. Lantz et al. *Review: Requirements for a Ground Rotation Sensor to Improve Advanced LIGO*, Bulletin of the Seismological Society of America, Vol. 99, No. 2B, 2009

[32] C. Collette et al. *Review: Inertial Sensors for Low-Frequency Seismic Vibration Measurement*, Bulletin of the Seismological Society of America, Vol. 102, No. 4, 2012

[33] D. E. Clark, *Control of Differential Motion Between Adjacent Avanced LIGO Seismic Isolation Platforms*, PhD thesis, Stanford University, 2013

[34] S. M. Aston at al., *Update on quadruple suspension design for Advanced LIGO*, Class. Quantum Grav., 29 (2012) 235004 (25pp)

[35] B. Shapiro, *Brief Introduction to Advanced LIGO Suspensions*, LAAC Talk, August 2014, https://dcc.ligo.org/LIGO-G1400964

[36] C. Di Fronzo et al., *Proposal for an experiment at LHO: Locking PRCL to IMCL*, proposal, 2019, DCC T1900656-v2

[37] C. Di Fronzo et al., *Reducing differential motion using CPS sensors*, technical note, 2019, DCC T1900777-v1

[38] C. Di Fronzo, *Reducing differential motion of Advanced LIGO seismic platforms to improve interferometer control signals*, talk, LVK September 2020

[39] S. Biscans et al., *Control strategy to limit duty cycle impact of earthquakes on the LIGO gravitational-wave detectors*, arXiv:1707.03466, 2017

[40] J. Kissel, *On Relaxing Our Demand for Single IFO Duty Cycle*, talk, 2019, DCC G1901125-v1

[41] A. Pele' *Lockloss status at beginning of O3 (LLO)*, Talk, dcc.ligo.org/LIGO-G1901122

[42] S. Biscans, *Global seismic control*, talk, GWADW 2019

[43] A. Biswas et al., *New methods to assess the impact of seismic events on LIGO detector duty cycle*, 2019, arXiv:1910.12143

[44] J. Kissel, *Calibrating and improving the sensitivity of the LIGO detectors*, PhD thesis, 2010

[45] LIGO Scientific Collaboration *Advanced Ligo*, LIGO-P1400177-v5

[46] J. Kissel, *Advanced LIGO Active Seismic Isolation*, talk, 2011

Bibliography

[47] C. Di Fronzo et al., *Reducing differential motion of Advanced LIGO seismic platforms to improve interferometer control signals: block diagrams and maths*, technical note, 2020, DCC T2000108-v1

[48] C. Di Fronzo et al., *Reducing differential motion of Advanced LIGO seismic platforms to improve interferometer control signals:analysis of feasibility*, technical note, 2020, DCC T2000365-v2

[49] J. Driggers, *Noise Cancellation for Gravitational Wave Detectors*, PhD thesis, 2016

[50] A. Pele' et al., *ECR: Differential CPS and cavity offload*, proposal, 2019, DCC E1900330-v1

[51] LHO and SEI team *The impact of CPS differential controls on scattered light glitches in O3b*, alog.ligo-wa.caltech.edu/aLOG/index.php?callRep=56293

[52] LHO team *Turned off CPS DIFF* alog.ligo-wa.caltech.edu/aLOG/index.php?callRep=53926

[53] B. Lantz et al., *Estimates of HAM-ISI motion for A+*, technical note, 2018, DCC T1800066-v2

[54] S. Cooper et al., *Ham ISI Model*, technical note, 2018

[55] C. Di Fronzo et al, *A 6D inertial isolation system*, ET Symposium, 2019, poster, https://dcc.ligo.org/LIGO-G1900741

[56] C.M. Mow-Lowry, D. Martinov, *A 6D interferometric inertial isolation system*, 2019 Class. Quantum Grav. 36, 24

[57] L Barsotti et al, *Alignment sensing and control in advanced LIGO* 2010 Class. Quantum Grav. 27 084026

[58] S. Cooper et. al, *A compact, large-range interferometer for precision measurement and inertial sensing*, 2018 Class. Quantum Grav. 35 095007

[59] S. Cooper, *Breaking the Seismic Wall: How to Improve Gravitational Wave Detectors at Low Frequency*, PhD thesis, University of Birmingham, 2019

[60] $https://rio-lasers.com/1064-nm-laser-module/$

[61] Test of the lasers at UoB $https://lnx0.sr.bham.ac.uk:8081/ifo/371$

[62] $https://www.photonicsolutions.co.uk/upfiles/ADJUSTIK FiberLaserLG13Dec17.pdf$

[63] $https://edge.coherent.com/assets/pdf/COHR\_MephistoNPRO$

[64] Andreas Freise, *The Next Generation of Interferometry: Multi-Frequency Optical Modelling, Control Concepts and Implementation*, Appendix B *Control loops*, PhD thesis, 2003

[65] https://en.wikipedia.org/wiki/Control-system

[66] ligo.caltech.edu *Observation Of Gravitational Waves From a Binary Black Hole Merger*

[67] M. Cavaglia, *Logo slide with institution names*, DCC G1300394

[68] Buikema A. et al., *Sensitivity and Performance of the Advanced LIGO Detectors in the Third Observing Run*, https://dcc.ligo.org/LIGO-P2000122

[69] Davis D. et al., *LIGO Detector Characterization in the Second and Third Observing Runs*, https://dcc.ligo.org/LIGO-P2000495